# THE BIOFILM MATRIX IN SULFATE-REDUCING BACTERIAL BIOFILMS: POTENTIAL ROLES FOR ELECTRON MEDIATORS AND LARGE PROTEINS

by

Gregory Peter Krantz

A dissertation submitted in partial fulfillment
of the requirements for the degree

of

Doctor of Philosophy

in

Microbiology and Immunology

MONTANA STATE UNIVERSITY
Bozeman, Montana

November 2019

# ACKNOWLEDGEMENTS

Many thanks to my mentor, Dr. Matthew Fields for allowing me the opportunity to grow into the scientist that I am in your laboratory. It has been a privilege to work with an advisor who respects the overall wellbeing of their students in addition to their professional progress. I am grateful to my committee members Dr. Robin Gerlach, Dr. Gill Geesey, Dr. Jim Wilking, and Dr. Zbigniew Lewandowky for taking the time to meet and review my work and provide your feedback. The Center for Biofilm Engineering has been an incredible place to work. From exposure to industrial associates, to highly organized and well maintained equipment resources, these attributes grease the wheels of a career in science.

While getting a Ph.D can be intense at times, one thing that stood out to me was the gift of having time to wonder about things, and to have that be my job. The freedom to let my mind be curious about bacteria and to have the time to answer the questions that arose, has been an incredible and memorable experience.

Most importantly, I would like to thank my family, specifically my parents Jan and Ken, and my siblings Keegan and Lendy, because without their loving and articulate support, this would not have come to fruition.

I am deeply grateful to the Molecular Biosciences Fellowship Program and to ENIGMA for funding. The research community, funding resources, and vast array of collaboration opportunities have been breath-takingly impressive.

I would also like to thank all of my Bozeman friends outside of science that have supported me and enriched my life during my time in graduate school.

TABLE OF CONTENTS

TABLE OF CONTENTS CONTINUED

TABLE OF CONTENTS CONTINUED

TABLE OF CONTENTS CONTINUED

# LIST OF TABLES

# LIST OF FIGURES

Figure Page

LIST OF FIGURES CONTINUED

# ABSTRACT

Sulfate-reducing bacteria grow and form biofilms in soil and benthic environments across much of the Earth's surface. Formation of these prevalent biofilms requires the secretion of an extracellular polymeric substance (EPS) to allow the cells to stick together, as well as adhere to a surface. The specific interactions that occur between EPS components of an SRB biofilm are poorly understood. The data presented in this dissertation suggest the presence of two extracellular mechanisms utilized in these communities.

The first mechanism was observed in a study altering the lactate (electron donor) and sulfate (electron acceptor) ratios to create limiting nutrient conditions in *Desulfovibrio alaskensis* G20 (G20) biofilms. G20 was grown under two conditions: electron donor limited (EDL) and electron acceptor limited (EAL) conditions. When grown on a 1018 carbon steel substrate, the G20 consumes all of the available lactate, and once limited, it turns to the high energy electrons in the $Fe^0$ for growth. Corrosion rates in the steel increased two fold compared to the EAL condition. Global metabolomic analysis revealed increased lumichrome levels under the EDL condition, which suggested higher flux through the riboflavin/FAD biosynthetic pathway. Previous research showed that synthetically adding riboflavin and FAD increases the corrosion rate of a SRB biofilm on 1018 carbon steel, and paired with these results, suggest G20 produces a flavin-based extracellular electron transfer molecule endogenously, and uses it to harvest high energy electrons from $Fe^0$ when limited for electron donor.

The second mechanism was observed in *Desulfovibrio vulgaris* Hildenborough (DvH) biofilms grown on glass. Two proteins, DVU1012 and DVU1545 were found to be the most abundant extracellular peptides in a DvH biofilm. Single deletion strains for these proteins grew biofilm similar to the wild type strain, but a double deletion strain had decreased ability to form biofilm, demonstrating that at least one of the peptides must be present in order to form a biofilm. Exposure to increased shear force caused an large increase in wild-type biofilm biomass, yet eliminated the double mutant biofilm. These proteins are required for a DvH biofilm to respond to shear force.

# CHAPTER ONE

# INTRODUCTION

## Sulfate-Reducing Microorganisms

Sulfate-reducing microorganisms (SRM) are widely dispersed in anaerobic soil and benthic environments and reduce sulfate to hydrogen sulfide, playing an important role in the global sulfur cycle. SRM also oxidize fermentation byproducts and form a link between the global sulfur and carbon cycles in many anaerobic environments (Pester et al. 2012), and many SRM can also form syntrophic relationships with archaeal methanogens (*e.g.*, Brileya et al., 2014). Direct evidence of the C- and S-cycle link can be observed in stromatolites where sulfate-reduction activities (oxidizing lactate and reducing sulfate) form dome-shaped rock structures by precipitating $CaCO_3^-$ and storing carbon (Dupraz et al. 2005). SRM include Gram-negative mesophilic bacteria (*i.e.*, δ-*Proteobacteria*), Gram-positive spore-forming bacteria (*e.g.*, *Desulfotomaculum sp.*), thermophilic bacteria (*e.g.*, *Thermodesulfovibrio*), and thermophilic archea (*Archaeoglobus*) (Castro 2000) that can occupy a range of environmental conditions (*e.g.*, salinity, nutrients). SRM have been found in arctic sediments (Rabus et al. 2004), mesophilic soil habitats (Heidelberg et al. 2004), hot springs environments (Hugenholtz 1998), and hypersaline lakes (Foti et al. 2007). One can conclude that SRM are ubiquitous throughout nature and are most likely driven by the wide distribution of sulfates and related compounds under anoxic conditions.

## Model Organisms

With respect to the δ-*Proteobacteria* SRM, this body of work will focus on the model microorganisms *Desulfovibrio alaskensis* G20 (G20) and *Desulfovibrio vulgaris* Hildenborough (DvH). G20 was isolated from a producing oil well in Ventura Country, California and is known to corrode ferreous metals and reduce heavy metals (Hauser et al. 2011). The G20 complete genome was sequenced and updated in 2011 and informed altered taxonomy that was changed from *Desulfovibrio desulfuricans* G20 to *Desulfovibrio alaskensis* G20 (Hauser et al. 2011). DvH has similar roles in metal corrosion and bioremediation and was isolated from clay soil in Hildenborough, Kent (UK) (Heidelberg et al. 2004). The DvH complete genome was sequenced in 2004 (Heidelberg et al. 2004) and there is a tractable genetic system for creating knockout mutant strains (Keller et al. 2008). Both organisms utilize hydrogen cycling as an intermediate in sulfate-reducing metabolism in a model proposed by Odom and Peck (Odom and Peck 1981); however, there has been debate about the wide-spread nature of hydrogen cycling in SRM or the possibly transient nature of hydrogen cycling function for a given organism (Keller and Wall 2011). Regardless of the specific metabolism that results in sulfate-reduction, the *Desulfovibrio* are major sulfate-reducers in numerous environments and have been both of great interest and subject to scrutiny for the last several decades due to utility in bioremediation or detrimental contributions to metal bio-corrosion and/or oil souring (Franco et al., 2018; Krantz et al., 2019). In fact, despite decades of research into the biochemistry of sulfate-reduction by the *Desulfovibrio*, a complete understanding of electron flow under different conditions is still not complete

(Keller and Wall 2011), and even more so for the biofilm growth mode (Clark et al., 2012). Hence, there is still considerable interest in understanding and ultimately controlling the sulfidogenic activity of SRM, particularly at interfaces (*i.e.*, biofilms). Because of metabolic versatility and distribution in different environments, the *Desulfovibrio* are model systems for studying anaerobic SRM metabolisms, metal reduction, aerotolerance, and microbially-induced corrosion (Holman et al., 2009; Rabus et al., 2015), and numerous studies have characterized *Desulfovibrio* biofilms (Clark et al., 2007; Clark et al., 2012; Kurczy et al., 2015; Stylo et al., 2015; Krantz et al., 2019; Scarascia et al., 2019).

## Biofilm Matrix

The biofilm matrix or EPS (exo-polymer substance) is a complex functional scaffold that enables cells to adhere to surfaces and to each other. It is an all-inclusive term for the extracellular macromolecules that include, but are not limited to polysaccharides (carbohydrates), extracellular DNA, membrane vesicles, cell debris from lysed cells, enzymes, and structural proteins (Flemming and Wingender, 2010; Flemming, 2016). While some of these components have been identified and a function established for a particular species (namely *Pseudomonas*, *Escherichia*, *Staphylococcus*, *Streptococcus*, *Bacillus*), there are still many matrix components that have not been identified or described for the breadth of bacterial diversity. Moreover, the biofilm matrix is increasingly being realized to contain a variety of intra- and inter-matrix interactions that contribute and may control biofilm behavior (Schooling and Beveridge, 2006; Payne and Boles, 2016). More recently, Hooper and Burstein posited that the

minimization of extracellular space in prokaryotic (*i.e.*, *Bacteria* and *Archaea*) biofilms promoted cellular associations that impacted metabolism and may have contributed to the evolution of *Eukarya* (Hooper and Burstein, 2014).

The biofilm EPS plays a crucial role in providing the evolutionary advantages of microbial life adhered to a surface (Costerton et al. 1978) by providing adhesion and cohesion properties as well as protection from predation, dessication, and detrimental products (*e.g*., biocides). In addition to the many molecular components that comprise the biofilm matrix, the biofilm can serve as a local repository for cellular materials that can be utilized (or recycled) in the future (Fleming and Wingender 2010). As such, the biofilm matrix can be thought of as a microbial storage compound, storing cell debris as well as capturing molecules sorbed from passing fluid flow. This can include metal ions, nutrients for growth, large particles like sand, and even minerals formed during growth such as corrosion products in metal biofilms (McNeil and Little, 1990). The biofilm matrix binds all these materials and keeps them close to the cells for convenient access.

Many microorganisms produce polymers that promote interactions with both biotic and abiotic surfaces (Costerton et al. 1978), and historically carbohydrate/polysaccharide interactions in the biofilm matrix have been a research focus (Costerton et al., 1978; Fleming and Wingender 2010; Fleming 2016 and references therein). *Desulfovibrio vulgaris* Hildenborough (DvH) is a model microorganism for sulfate-reducing bacteria and produces a biofilm that is predominantly dependent upon protein when grown on a glass substrate (Clark et al., 2007; Clark et al. 2012).

Therefore, much less is known about biofilm matrix proteins and the roles played in biofilm formation, maintenance, and disassembly.

Recently, bacteria such as *E. coli* and *P. fluorescens* Pf0-1 have been shown to synthesize extracellular proteins such as curli (CsgA) and LapA that play a role in binding cells together in the biofilm (Hobley et al. 2015, Smith et al. 2018). Curli is a major component of the *E. coli* biofilm forming "amyloid like" β-sheet structures in EPS, and LapA is anchored in the outer membrane and mediates adhesion to a variety of substrates (El-Kirat-Chatel et al. 2014).

## Type 1 Secretion Systems (T1SS)

In order for proteins to be secreted outside the cell, they must be transported across the membrane(s) and cell wall. T1SS perform that function and are commonly identified in Gram-negative bacteria and typically perform the translocation of proteins through both the cell membrane and the outer membrane in a single step. The *Escherichia coli* T1SS mechanism is the most well studied system and it requires an ABC transporter, a membrane fusion protein (MFP), and an outer membrane protein (OMP) (Spitz et al. 2019). In *E. coli,* the ABC transporter (HlyB) crosses only the inner membrane where it forms a complex with the MFP (HlyD) (Kanonenberg et al. 2018). The OMP (TolC) crosses the outer membrane, and together with HlyD/B form the pore complex that exports T1SS substrates extracellular to the cell proper (Kanonenberg et al. 2018). The proteins targeted for export typically have a secretion signal on the C-terminus, are secreted in the reverse direction to translation, and the secretion sequence is not cleaved during or after transport (Kanonenberg 2018).

## Shear Force on the Biofilm Matrix

While biofilms are mostly made of biologically produced materials and cell interactions are on the μm level, they are still subjected to physical forces such as shear. Often biofilms are hydrated, and are therefore, exposed to various flow rates of the surrounding aqueous medium. Shear forces can determine biofilm structure as well as diversity. Biofilms under low flow conditions can lack cohesivity, whereas those under high flow conditions are thinner, stronger, and more dense (Liu and Tay 2002). In addition, higher shear forces have been shown to impact community dynamics and cause a decrease in biofilm diversity (Rochex et al. 2008). *Pseudomonas aeruginosa* has been shown to sense shear forces and that leads to increased levels of the biofilm signaling molecule cyclic-di-GMP and biofilm initiation (Rodesney et al. 2017). Since cyclic-di-GMP regulates whether cells attach to a surface or disperse, being able to sense the forces impacting the community is an important factor in making that decision. Shear forces might be an important parameter constraint that significantly contributes to the ability of microorganisms to form and maintain biofilm.

## Microbially-Induced Corrosion

Surface attached microbial communities are capable of chemically interacting and altering the substrates they form on. SRB growing on mild steel can consume and damage the material in a process called microbially-influenced corrosion (MIC). This is a widespread problem incurring significant financial cost to the petroleum industry which installs and maintains steel pipeline infrastructure over vast distances (Li et al. 2015). It

has been referred to as the “industrial venereal disease-it’s expensive, everybody has it, and nobody wants to talk about it” (Odom and Singletone, 1993). Carbon steel oil pipelines can slowly corrode abiotically under a variety of conditions, and when sulfate-reducing communities are present, corrosion rates can be greatly accelerated (Enning and Garrelf 2014). The cost of metal corrosion in the US alone is estimated to be 2% to 3% of GDP (Gross Domestic Product) (Enning and Garrelf 2014) and is particularly important to carbon steel energy pipeline infrastructure. Corrosion induced failures in infrastructure create hazards to health, safety, environment, and product deliverability, and adding to the wide distribution of the problem, MIC occurs under a wide variety of environmental conditions, including marine, freshwater and terrestrial locations.

MIC can involve a variety of different microorganisms that include sulfate-reducing bacteria (SRB) and iron-reducing bacteria (IRB) (Little et al. 2007, Enning and Garrelfs 2014, Bonifay et al. 2017). Together with SRBs and IRBs, microbial consortia are typically involved in two mechanisms of MIC: electrical-MIC (EMIC), directly attacking the iron via oxidation, and/or chemical-MIC (CMIC), indirectly corroding the steel by producing sulfide and/or consuming $H_2$. Historically, CMIC was the only method by which anaerobic corrosion could occur, emphasizing the importance of sulfide concentrations in relation to corrosion rate (Dinh et al. 2004). While the CMIC mechanisms have been well studied, direct interactions via EMIC between the metal and the microorganisms are poorly understood.

Conventional corrosion research also attributed non-CMIC to consumption of the cathodically produced $H_2$ by the SRB. There are a few reasons why this mechanism is not

able to explain the increased corrosion observed when bacteria are present. $H_2$ production by mild steel and water is quite slow and limited by proton availability (Kaesche 2012). Electrochemical measurements made while growing a corrosive SRB (*D. corrodens* IS4) vs. a non-corrosive hydrogen consumer (*Desulfovibrio* sp. Strain HS3) showed a large increase in current in a metal coupon when in the presence of the corrosive SRB (Ref ?). A *Desulfobacterium*-like isolate was observed reducing sulfate with metallic iron as the electron donor faster than the rate of abiotic $H_2$ production (Dinh et al. 2004). In addition, an isolated *Methanobacterium*-like archeon was shown to use iron to produce methane faster than known hydrogenotrophic methanogens (Dinh et al. 2004). These results suggest a mechanism of direct (or indirect) electron uptake is necessary to explain the increased corrosion rates observed that cannot be explained by abiotically produced hydrogen and subsequent bacterial consumption.

Recent work postulates that SRBs contribute to MIC under various conditions and can conserve energy from $Fe^0$ oxidation through direct interactions with carbon steel (Venzlaff et al. 2013; Enning and Garrelfs 2014, Li et al. 2015). Extracellular electron transfer (EET-electron exchange between biotic and extracellular abiotic substrates), which is shown to enhance MIC, is now recognized as a more widespread microbial phenotype and suggests that EMIC could be a major mechanism for biocorrosion world-wide (Nealson and Saffarini, 1994, Kato 2016). In addition to heme redox centers of cytochromes, cell-secreted molecules have been shown to serve as electron carriers in EET processes in both *Shewanella oneidensis* and *Geobacter sulfurreducens* (Marsili et al. 2008; Okamoto et al. 2014), and more recently, FMN and riboflavin were proposed to

function in a diffusion-based EET (2 $e^-$) or bifurcated direct EET (1 $e^-$) in *Shewanella* (Okamoto et al. 2014). Future work should focus to elucidate the physiological conditions under which EET mechanisms contribute to overall biocorrosion.

Carbon starvation was shown to be associated with more aggressive corrosion by *Desulfovibrio vulgaris* biofilms (Xu and Gu 2014, Chen et al. 2015) and demonstrated the prolonged survival of *D. vulgaris* biofilms in the absence of organic electron donors. Recent work demonstrated that DvH had altered metal tolerance (i.e., Cr(VI)) under altered carbon and energy stoichiometries (Franco et al., 2018) but the mechanisms were not elucidated. Recent studies with *D. vulgaris* 7757 showed that the addition of $FAD^+$ or riboflavin could accelerate metal corrosion of 304 stainless steel and 1018 carbon steel (Li et al. 2015; Zhang et al. 2015), and electron transfer was hypothesized to be a limiting step for biocorrosion. However, a mechanistic link between nutrient/energy deprivation, corrosion, and electron-transfer systems have not been shown.

## Corrosion Minerals

When biofilms grow on steel and cause corrosion, the chemical reactions catalyzed by the cells produce corrosion products that form within the biofilm. In the presence of SRB and the subsequent sulfide, the ionized iron quickly forms iron sulfide minerals (Enning and Garrelf 2014). There are six iron sulfide minerals that occur naturally, mackinawite, pyrrhotite, greigite, smythite, marcasite, and pyrite. In aqueous settings at low temperature and pressure where SRB can grow and produce hydrogen sulfide, most of these minerals originate as mackinawite, and are then converted to one of the other species (Smith and Miller, 1975). Subsequent forms that are created depend on local chemical

equilibrium. The exception to this is smythite, which precitipitates as itself and can be converted to the other species. When iron sulfides form on a metal surface, the succession order the species go through is mackinawite, pyrrhotite, and then pyrite (Smith and Miller 1975).

## Nutrient Limitation

The recognition of changing environmental conditions, such as nutrient availability, is essential to organismal growth and survival, and microorganisms are acutely adept at maximizing available resources for biomass and energy conservation. However, most microbial studies have been conducted on planktonic cells grown in suspension due to utility for study and sampling, and not the more predominant life-style of attached growth (*i.e.*, biofilm). Bacteria have the ability to sense extracellular signals, via two-component regulatory systems for example, and can then feed those signals into transcriptional regulatory systems, resulting in a change in gene expression and subsequent adjustment of metabolism to better perform under given external constraints (Rajeev et al. 2011). Another layer of extracellular sensing is the cell's ability to coordinate control of multiple inputs and adjust accordingly. For example, *E. coli* carbon utilization can be coordinated with nitrogen availability, and carbohydrate transport can be coordinated with the regulation of carbohydrate-utilizing enzymes (*i.e.*, glucose and the Lac operon). In the instance of coordinated N and C utilization, α-ketoglutarate inhibits enzyme I of the phosphotransferase system, and subsequently glucose uptake is adjusted in response to N availability (Doucette et al. 2011), thereby using the α-ketoglutarate/glutamate metabolic node of the TCA (tricarboxylic acid cycle) to help control influx of carbon (*i.e.*, glucose)

in light of available N in terms of α-ketoglutarate/glutamate/glutamine. In another example, carbon and sulfur metabolisms are linked by CysB, a transcriptional regulator of the sulfur metabolism in *E. coli* and *Salmonella* that regulates an operon encoding genes required for uptake of sulfur sources and for the synthesis of cysteine. When *cysB* is mutated, the organism has 50% less enzyme activity for enzymes involved in carbon source uptake and utilization (Quan et al. 2002).

In *D. vulgaris,* dissimilatory sulfate reduction and carbon uptake and utilization are presumably coordinated as well, although the mechanism has not yet been elucidated. One potential player in this coordination is RexB, a repressor of sulfate adenylyl transferase (*sat*), the gene that encodes the enzyme responsible for activating sulfate in the first step of sulfate reduction. RexB is regulated by cellular levels of NAD/NADH+$H^+$ in that NADH+$H^+$, but not $NAD^+$, binds with RexB and prevents it from binding DNA. Elevated intracellular levels of NADH+$H^+$ therefore prevent RexB from repressing *sat* transcription, allowing the first step of sulfate reduction to commence (Christensen et al. 2015). While RexB certainly links sulfate reduction to the redox state of the cell through the NAD/NADH+$H^+$ ratio, it could also be a link to the central carbon metabolism, as NADH is a product of the TCA cycle.

Previous work by Franco et al. (2018) demonstrated that altering the ratio of electron donor and electron acceptor can greatly affect the physiology of *D. vulgaris* Hildenborough. *Desulfovibrio vulgaris* Hildenborough was grown under three conditions, electron donor limited (EDL), electron acceptor limited (EAL), and a balanced condition (BAL). Cells grown under the EAL condition had higher

susceptibility to chromium toxicity than genetically identical cells grown under the EDL and BAL condition. In addition, large extracellular membranous structures were observed in the biofilm at increased levels under the EAL condition compared to BAL condition. (Franco et al. 2017). These results demonstrated that physiology of a single species biofilm can be altered by changing the ratio of available nutrients, and the surrounding redox potential and state of the cell(s) are likely to play important roles.

## Thesis Objectives

For the presented results in chapter two, I hypothesized that changing the nutrient ratio on a G20 biofilm would create differences in the biofilm physiology of *D. vulgaris* Hildenborough and alter the flow of electrons through metabolic pathways that could impact overall corrosion rates. Two different carbon/energy stoichiometry conditions were used: the EAL condition (electron-acceptor limited) in which sulfate was the limiting substrate and the EDL (electron donor limited) condition in which lactate was limiting substrate. Biofilms were grown under both conditions on three surface types to identify biofilm physiological differences on each: glass, 316 stainless steel, and 1018 carbon steel. Several differences in biofilm physiology were observed, including the increased corrosion rate on the 1018 carbon steel substrate under the EDL condition compared to the EAL condition. The mechanism allowing G20 to achieve this effect was unknown, so global metabolomics was done comparing the EAL and EDL condition on 1018 carbon steel. Interest in molecular mechanisms in the extracellular polymeric space arose once the metabolomics results suggested the presence of a flavin-based extracellular electron transfer molecule was increased under the EDL condition.

Given the importance of biofilms to metal corrosion and the role of proteins in DvH biofilms, Chapter three focused on the characterization of the two most abundant proteins in the extracellular fraction of a DvH biofilm grown under sulfate-reducing conditions: DVU1012 and DVU1545. The predicted polypeptides are quite large at 3038 and 2414 amino acids, respectively, and therefore, despite a high investment cost (i.e., energy for biosynthesis) the presumptive proteins must play crucial roles for biofilms. Previous work by De Leon, Zane, Trotter, Krantz et al. (2017) showed that a double deletion strain was biofilm deficient compared to single deletion or wild type strains (see appendix). In the presented results, characterization was performed with wild-type, mono-mutant, and double mutant strains as well as bioinformatic protein structure predictions.

The goals for chapter four were to take the two single deletion and wild-type strains from chapter three and characterize biofilm physiology and corrosion behavior when grown on 1018 carbon steel (a substrate with high corrosion rates demonstrated in chapter 2). I hypothesized that based upon the described structural roles for DVU1012 and 1545 gene products, corrosion behavior and corrosion mineral formation would be impacted as a large variety of corrosion products were previously observed (chapter two).

The metabolomics dataset from chapter two was done in collaboration with Dr. Gary Suizdak's laboratory at The Scripps Institute. This dataset was used to test a mobile metabolomics platform for smartphone use and the subsequent manuscript was published in *Analytical Chemistr*y (Appendix A). The same metabolomic dataset was also used as

a proof of concept for a multiomics analysis tool implemented as part of XCMS Online, which is a powerful online metabolomics analysis platform developed by Gary Suizdak's laboratory with the use of described dataset. A corrosion RNA-seq dataset run by Dr. Mike Franklin's laboratory was combined with the metabolomics dataset and was published in *Nature Methods* (Appendix B). In a previous study by Franco et al. 2017, nutrient limitation was characterized in DvH and a metabolomics dataset was generated as part of this described work. Appendix C compares the DvH metabolomics dataset from Franco et al. 2017 with the G20 nutrient limitation metabolomics dataset from chapter two.

Chapter five is an overall presentation and discussion of the presented results within the context of previous work with *Desulfovibrio* biofilms and corrosion. Namely, the function prediction via physiology and bioinformatics for two previously unknown biofilm proteins is discussed related to potential modes of action compared to proteins with similar domains. The potential role of the structural biofilm proteins in metal corrosion is also discussed.

References

Liu, Y. & Tay, J.-H. The essential role of hydrodynamic shear force in the formation of biofilm and granular sludge. *Water Res.* **36**, 1653–1665 (2002).

Scarascia, G. *et al.* Quorum sensing effect on the ability of Desulfovibrio vulgaris to form biofilm and to biocorrode carbon steel in saline conditions. *Appl. Environ. Microbiol.* (2019). doi:10.1128/AEM.01664-19

Stylo, M., Neubert, N., Roebbert, Y., Weyer, S. & Bernier-Latmani, R. Mechanism of Uranium Reduction and Immobilization in Desulfovibrio vulgaris Biofilms. *Environ. Sci. Technol.* **49**, 10553–10561 (2015).

Kurczy, M. E. *et al.* Comprehensive bioimaging with fluorinated nanoparticles using breathable liquids. *Nat. Commun.* **6**, 5998 (2015).

Rabus, R. *et al.* A Post-Genomic View of the Ecophysiology, Catabolism and Biotechnological Relevance of Sulphate-Reducing Prokaryotes. *Adv. Microb. Physiol.* **66**, 55–321 (2015).

Holman, H.-Y. N. *et al.* Real-time molecular monitoring of chemical environment in obligate anaerobes during oxygen adaptive response. *Proc. Natl. Acad. Sci. U. S. A.* **106**, 12599–12604 (2009).

Brileya, K. A., Camilleri, L. B., Zane, G. M., Wall, J. D. & Fields, M. W. Biofilm growth mode promotes maximum carrying capacity and community stability during product inhibition syntrophy. *Front. Microbiol.* **5**, 693 (2014).

Kaesche, H. *Corrosion of Metals: Physicochemical Principles and Current Problems*. (Springer Science & Business Media, 2012).

Smith, J. S. & Miller, J. D. A. Nature of Sulphides and their Corrosive Effect on Ferrous Metals: A Review. *Br. Corros. J.* **10**, 136–143 (1975).

Okamoto, A., Nakamura, R., Nealson, K. H. & Hashimoto, K. Bound Flavin Model Suggests Similar Electron-Transfer Mechanisms in Shewanella and Geobacter. *CHEMELECTROCHEM* **1**, 1808–1812 (2014).

Marsili, E. *et al.* Shewanella secretes flavins that mediate extracellular electron transfer. *Proc. Natl. Acad. Sci. U. S. A.* **105**, 3968–3973 (2008).

Rochex, A., Godon, J.-J., Bernet, N. & Escudié, R. Role of shear stress on composition, diversity and dynamics of biofilm bacterial communities. *Water Res.* **42**, 4915–4922 (2008).

El-Kirat-Chatel, S., Beaussart, A., Boyd, C. D., O'Toole, G. A. & Dufrêne, Y. F. Single-cell and single-molecule analysis deciphers the localization, adhesion, and mechanics of the biofilm adhesin LapA. *ACS Chem. Biol.* **9**, 485–494 (2014).

Rusconi, R., Guasto, J. S. & Stocker, R. Bacterial transport suppressed by fluid shear. *Nat. Phys.* **10**, 212 (2014).

Payne, D. E. & Boles, B. R. Emerging interactions between matrix components during biofilm development. *Curr. Genet.* **62**, 137–141 (2016).

Hooper, S. L. & Burstein, H. J. Minimization of extracellular space as a driving force in prokaryote association and the origin of eukaryotes. *Biol. Direct* **9**, 24 (2014).

Odom, J. M. & Singleton, R. *The Sulfate-Reducing Bacteria: Contemporary Perspectives*. (Springer, New York, NY, 1993).

Odom, J. M. & Peck, H. D., Jr. Hydrogen cycling as a general mechanism for energy coupling in the sulfate-reducing bacteria, Desulfovibrio sp. *FEMS Microbiol. Lett.* **12**, (1981).

Foti, M. *et al.* Diversity, activity, and abundance of sulfate-reducing bacteria in saline and hypersaline soda lakes. *Appl. Environ. Microbiol.* **73**, 2093–2100 (2007).

Castro, H. F., Williams, N. H. & Ogram, A. Phylogeny of sulfate-reducing bacteria(1). *FEMS Microbiol. Ecol.* **31**, 1–9 (2000).

Pester, M., Knorr, K.-H., Friedrich, M. W., Wagner, M. & Loy, A. Sulfate-reducing microorganisms in wetlands - fameless actors in carbon cycling and climate change. *Front. Microbiol.* **3**, 72 (2012).

Krantz, G. P. *et al.* Bulk phase resource ratio alters carbon steel corrosion rates and endogenously produced extracellular electron transfer mediators in a sulfate-reducing biofilm. *Biofouling* 1–15 (2019).

Hugenholtz, P., Pitulle, C., Hershberger, K. L. & Pace, N. R. Novel division level bacterial diversity in a Yellowstone hot spring. *J. Bacteriol.* **180**, 366–376 (1998).

Rabus, R. *et al.* The genome of Desulfotalea psychrophila, a sulfate-reducing bacterium from permanently cold Arctic sediments. *Environ. Microbiol.* **6**, 887–902 (2004).

Dupraz, C. & Visscher, P. T. Microbial lithification in marine stromatolites and hypersaline mats. *Trends Microbiol.* **13**, 429–438 (2005).

Spitz, O. *et al.* Type I Secretion Systems-One Mechanism for All? *Microbiol Spectr* **7**, (2019).

Kanonenberg, K., Spitz, O., Erenburg, I. N., Beer, T. & Schmitt, L. Type I secretion system-it takes three and a substrate. *FEMS Microbiol. Lett.* **365**, (2018).

Persat, A. *et al.* The mechanical world of bacteria. *Cell* **161**, 988–997 (2015).

Bill Costerton, Gill Geesey, K.J. Cheng. How Bacteria Stick. (1978). doi:10.1038/scientificamerican0178-86

Flemming, H.-C. EPS-Then and Now. *Microorganisms* **4**, (2016).

Smith, T. J., Font, M. E., Kelly, C. M., Sondermann, H. & O'Toole, G. A. An N-Terminal Retention Module Anchors the Giant Adhesin LapA of Pseudomonas fluorescens at the Cell Surface: a Novel Subfamily of Type I Secretion Systems. *J. Bacteriol.* **200**, (2018).

Hobley, L., Harkins, C., MacPhee, C. E. & Stanley-Wall, N. R. Giving structure to the biofilm matrix: an overview of individual strategies and emerging common themes. *FEMS Microbiol. Rev.* **39**, 649–669 (2015).

Flemming, H.-C. & Wingender, J. The biofilm matrix. *Nat. Rev. Microbiol.* **8**, 623–633 (2010).

Little, B. J. & Lee, J. S. *Microbiologically Influenced Corrosion*. (John Wiley & Sons, 2007).

Nealson, K. H. & Saffarini, D. Iron and manganese in anaerobic respiration: environmental significance, physiology, and regulation. *Annu. Rev. Microbiol.* **48**, 311–343 (1994).

Bonifay, V. *et al.* Metabolomic and Metagenomic Analysis of Two Crude Oil Production Pipelines Experiencing Differential Rates of Corrosion. *Front. Microbiol.* **8**, 99 (2017).

Clark, M. E., Edelmann, R. E., Duley, M. L., Wall, J. D. & Fields, M. W. Biofilm formation in Desulfovibrio vulgaris Hildenborough is dependent upon protein filaments. *Environ. Microbiol.* **9**, 2844–2854 (2007).

De León, K. B. *et al.* Unintended Laboratory-Driven Evolution Reveals Genetic Requirements for Biofilm Formation by Desulfovibrio vulgaris Hildenborough. *MBio* **8**, (2017).

Dinh, H. T. *et al.* Iron corrosion by novel anaerobic microorganisms. *Nature* **427**, 829–

832 (2004).

Kato, S. Microbial extracellular electron transfer and its relevance to iron corrosion. *Microb. Biotechnol.* **9**, 141–148 (2016).

Clark, M. E. *et al.* Transcriptomic and proteomic analyses of Desulfovibrio vulgaris biofilms: Carbon and energy flow contribute to the distinct biofilm growth state. *BMC Genomics* **13**, (2012).

Keller, K. L. & Wall, J. D. Genetics and Molecular Biology of the Electron Flow for Sulfate Respiration in Desulfovibrio. *Front. Microbiol.* **2**, (2011).

Xu, D. & Gu, T. Carbon source starvation triggered more aggressive corrosion against carbon steel by the Desulfovibrio vulgaris biofilm. *Int. Biodeterior. Biodegradation* **91**, 74–81 (2014).

Zhang, P., Xu, D., Li, Y., Yang, K. & Gu, T. Electron mediators accelerate the microbiologically influenced corrosion of 304 stainless steel by the Desulfovibrio vulgaris biofilm. *Bioelectrochemistry* **101**, 14–21 (2015).

Chen, Y. *et al.* Long-term survival of Desulfovibrio vulgaris on carbon steel and associated pitting corrosion. *Corros. Sci.* doi:10.1016/j.corsci.2014.09.016

Hauser, L. J. *et al.* Complete Genome Sequence and Updated Annotation of Desulfovibrio alaskensis G20. *J. Bacteriol.* **193**, 4268–4269 (2011).

Heidelberg, J. F. *et al.* The genome sequence of the anaerobic, sulfate-reducing bacterium Desulfovibrio vulgaris Hildenborough. *Nat. Biotechnol.* **22**, 554–559 (2004).

Li, H. *et al.* Extracellular Electron Transfer Is a Bottleneck in the Microbiologically Influenced Corrosion of C1018 Carbon Steel by the Biofilm of Sulfate-Reducing Bacterium Desulfovibrio vulgaris. *PLoS One* **10**, e0136183 (2015).

Enning, D. & Garrelfs, J. Corrosion of iron by sulfate-reducing bacteria: new views of an old problem. *Appl. Environ. Microbiol.* **80**, 1226–1236 (2014).

Venzlaff, H. *et al.* Accelerated cathodic reaction in microbial corrosion of iron due to direct electron uptake by sulfate-reducing bacteria. *Corros. Sci.* **66**, 88–96 (2013).

# CHAPTER TWO

## BULK PHASE RESOURCE RATIO ALTERS CARBON STEEL CORROSION RATES AND ENDOGENOUSLY PRODUCED EXTRACELLULAR ELECTRON TRANSFER MEDIATORS IN A SULFATE-REDUCING BIOFILM

### Contributions of Authors and Co-Authors

Manuscript in Chapter 2

Author: Gregory P. Krantz

Contributions: Developed experimental design, performed experiments, analyzed data, wrote and revised the manuscript.

Author: Kilean Lucas

Contributions: Performed experiments, analyzed data.

Author: Erica L. - Wunderlich

Contributions: Analyzed data, wrote and revised the manuscript.

Author: Linh T. Hoang

Contributions: Performed experiments, analyzed data.

Author: Recep Avci

Contributions: Analyzed data, wrote and revised the manuscript.

Author: Gary Suizdak

Contributions: Analyzed data, wrote and revised the manuscript.

Author: Matthew W. Fields

Contributions: Developed experimental design, analyzed data, wrote and revised the manuscript.

Manuscript Information

Gregory P. Krantz, Kilean Lucas, Erica L.- Wunderlich, Linh T. Hoang, Recep Avci,

Gary Siuzdak & Matthew W. Fields

Biofouling

Status of Manuscript:

____ Prepared for submission to a peer-reviewed journal
____ Officially submitted to a peer-reviewed journal
____ Accepted by a peer-reviewed journal
__X__ Published in a peer-reviewed journal

Taylor and Francis Group
November 19, 2018
August 11, 2019
2019, VOL. 35, NO. 6, 669–683

Abstract

*Desulfovibrio alaskensis* G20 biofilms were cultivated on 316 steel, 1018 steel, or borosilicate glass under steady-state conditions in electron-acceptor limiting (EAL) and electron-donor limiting (EDL) conditions with lactate and sulfate in a defined medium. Increased corrosion was observed on 1018 steel under EDL conditions compared to 316 steel, and biofilms on 1018 carbon steel under the EDL condition had at least twofold higher corrosion rates compared to the EAL condition. Protecting the 1018 metal coupon from biofilm colonization significantly reduced corrosion, suggesting that the corrosion mechanism was enhanced through attachment between the material and the biofilm. Metabolomic mass spectrometry analyses demonstrated an increase in a flavin-like molecule under the 1018 EDL condition and sulfonates under the 1018 EAL condition. These data indicate the importance of S-cycling under the EAL condition, and that the EDL is associated with increased biocorrosion via indirect extracellular electron transfer mediated by endogenously produced flavin-like molecules.

## Introduction

Microbiologically influenced corrosion (MIC) is a widespread problem incurring significant financial cost to the petroleum industry, the country, and communities. Carbon steel (CS) oil pipelines can slowly corrode abiotically under a variety of conditions, and when sulfate-reducing communities are present, corrosion rates can be greatly accelerated (Whitney 1903; Enning et al. 2012; Enning and Garrelfs 2014, and references therein). The cost of metal corrosion in the USA alone is estimated to be 2–3% of GDP (gross domestic product) (Enning and Garrelfs 2014) and is particularly important to the CS energy pipeline infrastructure. Corrosion induced failures in infrastructure create hazards to health, safety, environment, and product deliverability. Adding to the scale of the problem, MIC occurs under a wide variety of environmental conditions, including marine, freshwater and terrestrial locations. MIC can involve a variety of different microorganisms that include sulfate-reducing bacteria (SRB) and iron-reducing bacteria (IRB) (Little and Lee 2007; Enning and Garrelfs 2014; Bonifay et al. 2017). Together with SRB and IRB, microbial consortia are typically involved in two mechanisms of MIC: Type I is extracellular electron transfer (EET-MIC), which involves cross membrane electron transfer (indirect and/or direct) (Kato 2016 and references therein); and Type II is metabolite-MIC (M-MIC), i.e. biocorrosion caused by secreted metabolites (e.g. $H_2$, organic acids, sulfides) as opposed to chemical corrosion which can refer to direct metal–oxidant interactions (Li et al. 2018; Kannan et al 2018). Both EET-MIC and MMIC are electrochemical corrosion processes (Li et al. 2018; Dinh et al. 2004), and different EET mechanisms can promote the transfer of electrons to or from extracellular

solid compounds (Gralnick and Newman 2007; Kato 2016). The process of EET can be mediated directly with metal surfaces via cellular connections and/or conductive extracellular structures (e.g. Gorby et al. 2006) or indirectly via diffusible redox molecules (Watanabe et al. 2009). The goal of this study was to elucidate nutrient ratio impacts on potential M-MIC and/or EET-MIC mechanisms during initial biofilm formation under continuous growth conditions in a defined growth medium. Extracellular electron transfer, which is shown to enhance MIC, is now recognized as a more widespread microbial phenotype, suggesting that EET-MIC could be a major mechanism for biocorrosion worldwide (Nealson and Saffarini, 1994; Kato 2016; Huang et al. 2018). Previous work postulated that some SRBs contribute to MIC under various growth conditions through $Fe^0$ oxidation via interactions with CS (Gu, 2012; Venzlaff et al. 2013; Enning and Garrelfs 2014; Li et al. 2015). In addition to heme redox centers of cytochromes, cell-secreted molecules have been shown to serve as electron carriers in EET processes in both *Shewanella oneidensis* and *Geobacter sulfurreducens* (Marsili et al. 2008; Okamoto et al. 2014), and, more recently, flavin mononucleotide (FMN) and riboflavin were proposed to function in a diffusion-based EET (2 $e^-$) or bifurcated direct EET (1 $e^-$) in *Shewanella* (Okamoto et al. 2014). Therefore, future work should focus on elucidating the physiological conditions under which EET mechanisms contribute to overall biocorrosion. Carbon starvation was previously shown to be associated with more aggressive corrosion by *Desulfovibrio vulgaris* biofilms (Xu and Gu 2014; Chen et al. 2015), and the prolonged survival of *D. vulgaris* biofilms was demonstrated in the absence of organic electron donors. Studies with *D. vulgaris* 7757 showed that the

addition of flavin adenine dinucleotide (FAD) or riboflavin could accelerate corrosion of 304 stainless steel (SS) and 1018 CS (Li et al. 2015; Zhang et al. 2015), and electron transfer was hypothesized to be a limiting step for biocorrosion by *D. vulgaris*. While a relationship between nutrient deprivation and continued/accelerated biocorrosion has been shown for *Desulfovibrio*, the mechanism (Type I or II) under the nutrient deprived state is not known. Franco et al. (2018) demonstrated that nutrient ratios impacted metal interactions (i.e. Cr(VI) sensitivity) in *Desulfovibrio*, and we therefore hypothesized that nutrient imbalance would impact reduction–oxidation reactions in *Desulfovibrio* biofilms grown on a metal surface. In the present study, the corrosion rates and biofilm growth parameters under specific limiting nutritional ratios (i.e. electron donor : acceptor imbalance) were measured with chemostat biofilms under defined culture conditions (i.e. without yeast extract). Desulfovibrio alaskensis G20, isolated from a producing oil well in Ventura, CA (Hauser et al. 2011), was grown as a biofilm on glass, 316 SS and 1018 CS with lactate as electron donor and sulfate as electron acceptor in a defined medium. Electron-acceptor (EAL) and electron-donor (EDL) limited growth was achieved by adjusting relative concentrations (EAL50:15; EDL-15:15) in the chemostat medium. *Desulfovibrio* G20 demonstrated increased corrosion on 1018 CS under the EDL condition, and biofilm attachment with the steel was required for maximal corrosion rates. Global metabolomic results show increased sulfolactate levels under the EAL condition, which may indicate that sulfonate compounds are recycled for use as electron acceptors when sulfate is limited. Additionally, increased lumichrome levels were observed under the EDL condition on 1018 CS, and these results suggested *Desulfovibrio*

G20 produced flavin molecules that could be used to mediate extracellular electron transfers from steel $Fe^0$ .

## Materials and methods

### Microorganism

*Desulfovibrio alaskensis* G20 was grown in a defined (without yeast extract) lactate/sulfate (LS4D) medium prepared anoxically as previously described under a variety of conditions (see below). Modifications to the original recipe included adjusting the lactate and sulfate concentrations to 50 mM lactate:15 mM sulfate for EAL conditions and 15 mM lactate:15 mM sulfate for EDL conditions. As previously described, the medium was not prepared with a reducing agent (Clark et al. 2006), and the use of resazurin in the culture medium served as a general indicator of oxidative-reduction potential (ORP). Sodium hydrosulfite (18 $\mu g\ l^{-1}$) was added to the 10% resazurin solution to shift the solution from purple to pink.

### Planktonic growth

*D. alaskensis* G20 was cultivated in media with respective nutrient ratios at 37 C, 30 C and 20 C for initial planktonic cultures. The defined growth medium for both planktonic and biofilm growth was anoxically prepared and used as previously described (Clark et al. 2006, 2007; Klonowoska et al. 2008; Clark et al. 2012; DeLeon et al. 2017). All N2 gas (99.995% purity) was run through an oxygen-scrubber before being used to sparge any liquids or head-space as previously described at a rate of ~1 ml $min^{-1}$ (Brileya et al. 2014; Franco et al. 2018). Each batch condition was grown in triplicate in a Balch

tube with anoxic N2 headspace and sealed with butyl stoppers and a crimp seal. Optical density (600 nm) was measured with a UNICO 1100RS spectrophotometer (Dayton, NJ, USA) and compared with uninoculated medium.

Biofilm growth

Biofilm samples were grown in CDC biofilm reactors (Biosurface Technologies Corp., Bozeman, MT, USA) with the headspace sparged with anoxic N2 gas (run through an oxygen-scrubber). Separate reactors were used to cultivate G20 biofilms on each surface type: glass, 316 SS, and 1018 CS under each limiting nutrient condition. The 1018 and 316 CS coupons were not polished and used as received from Biosurface Technologies Corp. Reactors were inoculated with 40 ml of an exponential-phase culture and allowed to grow in batch mode for  24 h. The medium pump flow rate was set to 0.3 ml min1 ($D = 0.05\ h^{-1}$) 24 h post-inoculation and continuous flow was maintained until final samples were harvested. The dilution rate was chosen because the influent growth medium did not contain additional reducing agent as previously reported (Clark et al. 2006, 2012) and in situ growth rates are typically slower. The starting pH of medium was ~7.2 and during growth was 7.6–7.8. The glass coupon dimensions were 7.1 x 1.25 x 0.1 cm and the metal coupon dimensions were 7.6 x 1.5 x 0.1 cm. Modified coupon holders were used as previously described to provide increased material surface area (Clark et al. 2012).

Biofilm and coupon harvesting

Biofilm coupons were removed from the reactor and biofilm was immediately removed from the coupon using a sterile scraper. Biomass was scraped into 3 ml of dH2O

and homogenized by adding sand and vortexing prior to growth parameter measurements. The scraped coupon was dried and then treated according to standard practice for cleaning and evaluating corrosion samples (ASTM G1-03) with Clark Solution (6 M HCl, 3.5 g $l^{-1}$ hexamethylenetetramine) for 0.5 min before washing in nanopore H2O and dried with dry nitrogen gas as previously described (Avci et al. 2013). The coupons incubated in sterile, anoxic medium (EAL or EDL levels of lactate and sulfate) for the same time period displayed 0.01 ± 0.01 mm $y^{-1}$ mass loss. The post-exposure coupon mass was subtracted from the pre-exposure mass to obtain the mass loss, and the value of mm $y^{-1}$ or mg $cm^2$ was calculated as described in ASTM G1-03. Relative electrochemical measurements were made to the reference electrode in the presence of cells and compared between the EDL and EAL conditions.

Preparation of samples for imaging

Biofilm samples were fixed by treatment in Karmovsky's fixative (3.2% w v–1 paraformaldehyde, 2.5% w w–1 glutaraldehyde, 0.05 M sodium cocodylate) for 16 h. Samples were soaked 4x in dH2O for 5 min to remove fixative. Ethanol (EtOH) dehydration involved 5 min in 25% EtOH, 5 min in 50% EtOH, 5 min in 75% EtOH, 15 min in 95% EtOH, and 2 x 45 min in 100% EtOH before storage in 100% EtOH. Dehydrated samples were dried in a Tousimis Samdri-795 Critical Point Dryer (Tousimis Research Corporation, Rockland, MD, USA) using liquid CO2 and a 10 min purge time. Dried samples were coated with iridium for 30 s with an Emitech K575X Sputter Coater. Electron microscopy samples were imaged with a Zeiss Supra 55VP field emission scanning electron microscope (FE-SEM) (Carl Zeiss, Oberkochen, Germany) equipped

with energy dispersive X-ray analysis (EDX). Images were falsecolorized using Pixelmator (Vilnius, Lithuania) and Adobe Photoshop (San Jose, CA, USA).

Microscopy of biofilm cross sections

Biofilm coupons were incubated in acridine orange solution (4 g $l^{-1}$) for 1.5 h before being coated with Optimal Cutting Temperature Compound (Fisher Health Care, Pittsburgh, PA) and frozen on a block of dry ice. The frozen biofilm was removed from the metal coupon by bending the steel coupon, and stored at 80 C. The frozen biofilm samples were cut in half and sectioned with a Leica (Wetzlar, Germany) CM1850 cryostat (20 °C; 5 μm slices) and applied to a microscope slide for imaging. Images were taken with a Nikon Eclipse E800 microscope (Nikon Corporation, Minato, Tokyo, Japan) with a Photometrics Coolsnap MYO camera (Photometrics, Tucson, AR, USA). Images were taken at a FITC (fluorescein isothiocyanate) emission wavelength and differential interference contrast and overlaid using Metamorph software package (Molecular Devices, Sunnyvale, CA, USA).

Growth parameter measurements

Protein concentrations were measured with a Qubit Protein Assay Kit (Life Technologies, Carlsbad, CA, USA). Carbohydrate concentration was measured as previously described (Clark et al. 2006). Lactate and acetate were quantified using an Ultimate 3000 high performance liquid chromatography instrument with a 300 mm  7.8 mm HPLC Organic Acid Analysis Aminex HPX-87H Ion Exclusion Column (Thermo Scientific, Dionex Germering, Germany). Sulfate and hydrogen sulfide concentrations

were measured using a Hach Colorimeter (Hach, Co., Loveland, CO, USA) with the associated sulfate assay (Method 10248) and sulfide assay (Method 8131).

Protected 1018 steel coupons

Round 1018 steel coupons (127 mm) were placed in Spectra/Por Standard RC dialysis membranes (Spectrum Labs, Rancho Dominguez, CA) with a 6–8 kD molecular weight cutoff during the reactor run. The clamped membranes with steel coupons inside were suspended in the growth medium of a CDC biofilm reactor, and growth parameters and inoculation was the same as for biofilm cultivation.

Metabolomics and data processing

At 192 h, biofilm coupons (EAL and EDL on 1018 CS) were dipped in degassed dH2O and the biofilm biomass scraped into a sterile microcentrifuge tube with degassed dH2O (4 °C). The tubes were centrifuged at 10,000 rpm for 5 min at 4 °C. The supernatant was removed and the cell pellet frozen with liquid $N_2$ and stored at 80 °C. Samples were processed and data analyzed as previously described (Ivanisevic et al. 2013; Benton et al. 2015; Montenegro-Burke et al. 2016; Huan et al. 2017).

## Results and Discussion

| | Sulfate Yields | Lactate Yields | Acetate Yields |
|---|---|---|---|
| EAL | 0.042 ± 0.006 | 0.014 ± 0.002 | 0.033 ± 0.004 |
| EDL | 0.042 ± 0.008 | 0.032 ± 0.006 | 0.021 ± 0.004 |
| 60:50 Media | 0.025 ± 0.003 | 0.018 ± 0.002 | 0.027 ± 0.003 |

Table 1. Growth yields are shown from EAL, EDL, and 60:50 media calculated from sulfate consumption and lactate consumption over protein production.

Planktonic growth under different resource ratios

Planktonic growth was impacted by temperature, and *D. desulfuricans* G20 grew fastest at 37 °C and slowest at 20 °C in defined medium with lactate and sulfate (60:50 ratio). The specific growth rates were 0.05, 0.12, and 0.19 $h^{-1}$ , respectively, for 20 °C, 30 °C, and 37 °C, and the final yields were similar. *Desulfovibrio* G20 formed the thickest biofilm at 37 °C based on protein content in biofilm samples (data not shown), which is closest to elevated temperatures of some oil pipelines. In addition, 37 °C is the most commonly used temperature in the literature for *D. alaskensis* G20; therefore, all subsequent experiments were done at 37 °C. Growth rates were measured for planktonic cultures under the varied nutritional ratios that were tested in the experiments described. Maximum growth rates were similar at 0.21 $h^{-1}$ for EAL, 0.19 $h^{-1}$ for EDL, and 0.20 $h^{-1}$ for the 60:50 condition. As expected, final yields (OD values) were higher in media that had increased lactate concentrations. The 60:50 condition had the highest final biomass yield due to increased lactate and sulfate concentrations. The 60:50 condition is the standard SRB medium recipe used in numerous *Desulfovibrio* studies (Zhou et al. 2011) and was used as a basis for comparison in the study described. When planktonic biomass yields (protein) were compared in terms of sulfate or acetate ($Y^{Sulfate}$ or $Y^{Acetate}$) consumed, the EAL and EDL conditions were similar (Table 1). When the conditions were compared based upon $Y^{Lactate}$, the EDL condition had a higher yield that was twice the $Y^{Lactate}$ for the EAL condition. However, in terms of $Y^{Acetate}$, the EAL condition was 1.5-fold higher compared to EDL and similar to the 60:50 condition. The planktonic culture results suggested that biomass generation from a given amount of electrogenic

flow to sulfate was more efficient under the altered ratios for batch planktonic cells. The observations coincide with the theoretically low value of 0.06 mole of biomass ($C_5H_7O_2N$) produced per mole of lactate consumed (Equation 1) based upon assumed cellular stoichiometries for bacterial growth (McCarty 1971). The results suggest that planktonic cultures grown under the altered resource ratios (EAL and EDL) processed resources differently to the 60:50 condition in terms of lactate oxidized to acetate produced:

Equation 1 - $0.36\ SO_4^{-2} + 0.54\ H^+ + CH_3CHOHCOO^- + 0.06\ NH_3 + 0.11\ H_2O \rightarrow 0.18\ H_2S + 0.18\ HS^- + 0.72\ CO_2 + CH_3COO + 0.06\ C_5H_7O_2N\ \Delta G^{o'} = -88.96\ kJ\ mol^{-1}$ (1)

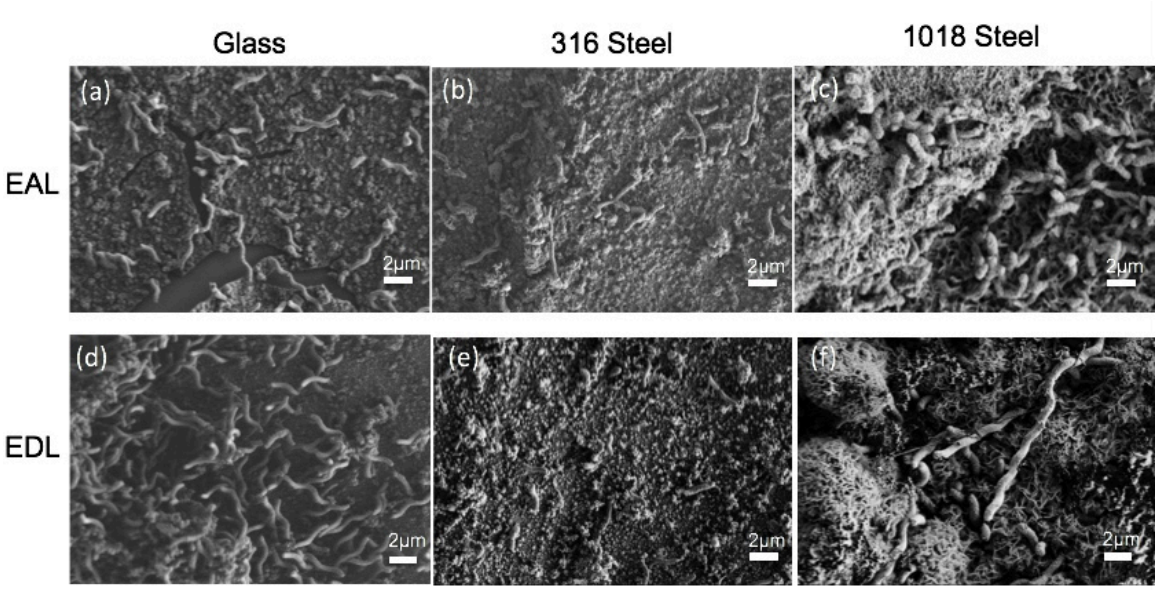


Figure 1. Field emission scanning microscopy images were taken at 15,000X magnification.

Biofilm on metal and glass

*Desulfovibrio* G20 formed and maintained visible biofilm on glass, 316 steel, and 1018 CS within 48 h under the tested EDL and EAL growth conditions; and as expected,

the 1018 CS surface appeared to have visible biofilm form earlier. The FE-SEM images show the presence of biofilm cells and other material that is most likely a combination of cellular material and mineral precipitates (Figure 1). In addition, the biofilms on glass and 316 SS had a lower cell density compared to the biofilms on 1018 steel (Figure 1), and this result corresponded to measured protein levels (Figure 2). As expected, the biofilm was visually less pronounced on the 316 SS surface, and biofilm/ metal precipitates were easier to remove from the 316 SS compared to the 1018 steel under both EAL and EDL. The observed biofilms on 1018 steel were visually more complex and heterogeneous under both EDL and EAL conditions. False-colored FE-SEM images showed a mixture of aggregated cells embedded within mineral precipitates for the EAL and EDL conditions (Figure 3a and b). Energy dispersive X-ray spectroscopy was used to differentiate materials based on elemental composition (data not shown), and the corrosion products (colored in orange) are abundant and likely composed of iron sulfide minerals that have been previously shown to be conductive (Thauer et al. 2007). The EDL biofilm displayed a combination of organic material that was most likely carbohydrate-based EPS and extracellular filaments in addition to cells. Filaments appeared similar to structures previously observed in *Desulfovibrio vulgaris* biofilms cultivated on glass under a nutrient ratio of 60:50 (Clark et al. 2006); however, the exact role of these structures is not known. However, *flaG* (gene DVU1442 annotated as a flagellin in *D. vulgaris* genome) was up-expressed in *D. vulgaris* biofilms (Clark et al. 2012); and a *ΔflaG* mutant was deficient in biofilm formation but not motility

(unpublished data). Further work is needed to determine the exact role(s) of extracellular structures in SRB biofilms grown on different surfaces and conditions.

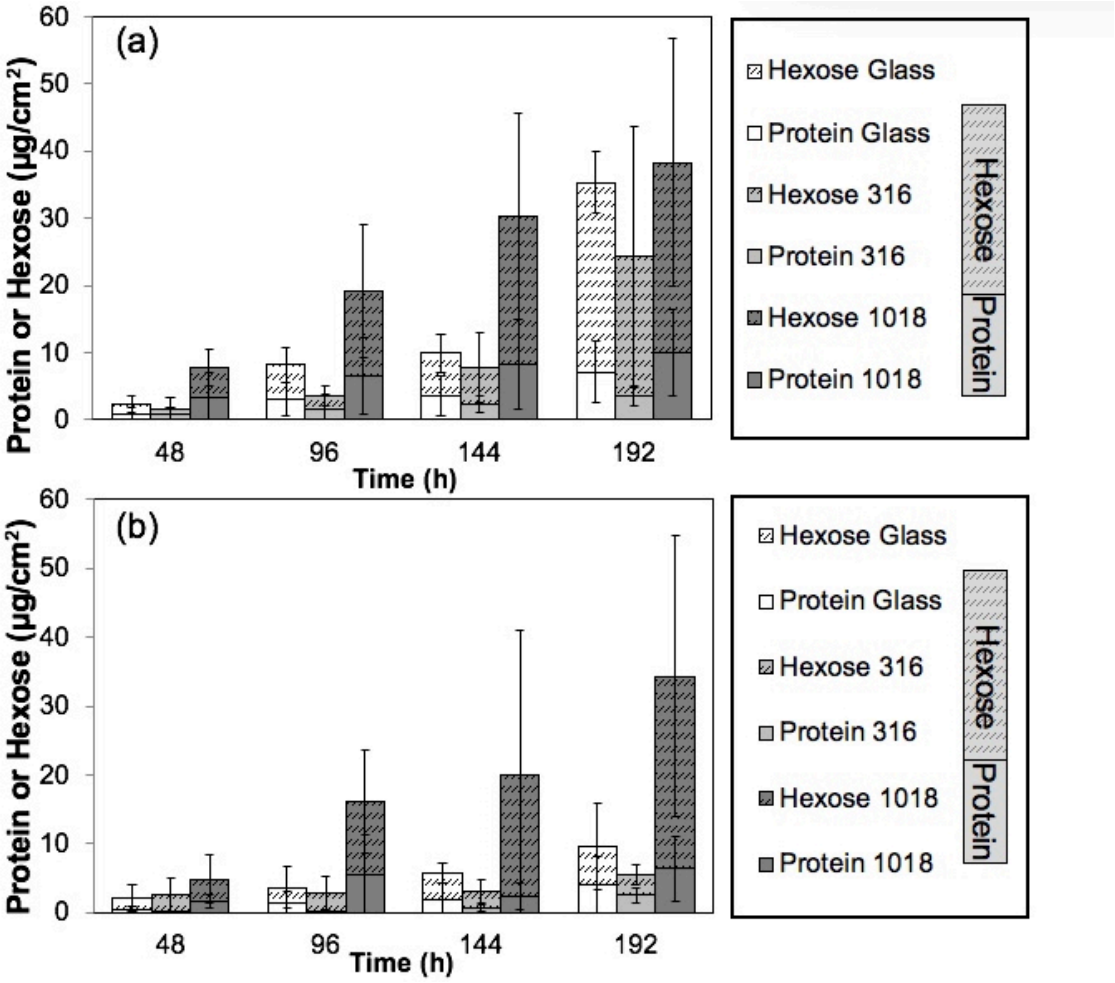


Figure 2. (a) Hexose and protein levels on glass, 316 stainless steel, and 1018 carbon steel coupons under EAL conditions. (b) Hexose and protein on glass, 316 stainless steel, and 1018 carbon steel coupons under EDL coupons.

Biofilm biomass

Carbohydrate and protein were quantified every 48 h for glass, 316 steel, and 1018 steel surfaces for both EAL and EDL conditions. The two metal surfaces under both EAL and EDL conditions displayed increasing biofilm (both protein and carbohydrate) over the

tested time course (192 h) with a trend of more biofilm under EAL conditions and most biofilm overall on 1018 steel (Figure 2). Under EAL conditions, glass and 316 steel biofilms had higher carbohydrate to protein (C:P) ratios compared to 1018 steel, and the biofilms on all three surfaces increased carbohydrate levels from 144 to 192 h as the biofilm matured (Figure 2). Under EDL conditions, carbohydrate and protein levels remained low on the glass and 316 steel biofilms. For EDL 1018 steel biofilms at 192 h, the C:P ratio was higher (4.36) compared to the 1018 EAL 192 h biofilms (2.86). The C:P ratios were higher for 192 h glass and 316 steel EAL biofilms (4.0 and 6.0, respectively) than the 192 h glass and 316 steel EDL biofilms (1.5 and 1.2, respectively) (Figure 2). These results suggest that carbon allocation is altered in biofilms on different surfaces and nutrient ratios, namely carbohydrate allocation under EAL conditions and protein in EDL conditions. The location (intracellular vs extracellular) is unknown for the protein and carbohydrate allocation. The biofilm composition data suggest that the biofilms responded differently to different types of energy restriction and coincides with previous work that has shown *Desulfovibrio* biofilm has altered physiology (i.e. electron flow is altered) even when compared to sulfate-reducing planktonic cells (Clark et al. 2012). Images were taken of the EAL and EDL biofilm cross-sections to measure biofilm thickness and show the distribution of *Desulfovibrio* G20 cells. The EAL biofilm (200 μm) was approximately fourfold thicker than the 50 μm EDL biofilm (Figure 4). The accumulation of corrosion products may aid in forming a textured surface to attach to, as well as an extracellular matrix to grow within; however, the accumulation of thicker biofilms under EAL conditions was not associated with increased corrosion. The

availability of more carbon source likely contributed to thicker biofilm at the 192 h time point on glass and 316 steel under EAL conditions than compared to EDL conditions. The 1018 steel biofilms had higher hexose levels than protein under both EAL and EDL conditions. Previous research by Clark et al. (2006) showed protein to be the major component of *D. vulgaris* Hildenborough (DvH) biofilms, with carbohydrate levels being relatively low. The current observations with glass and steel under EAL and EDL

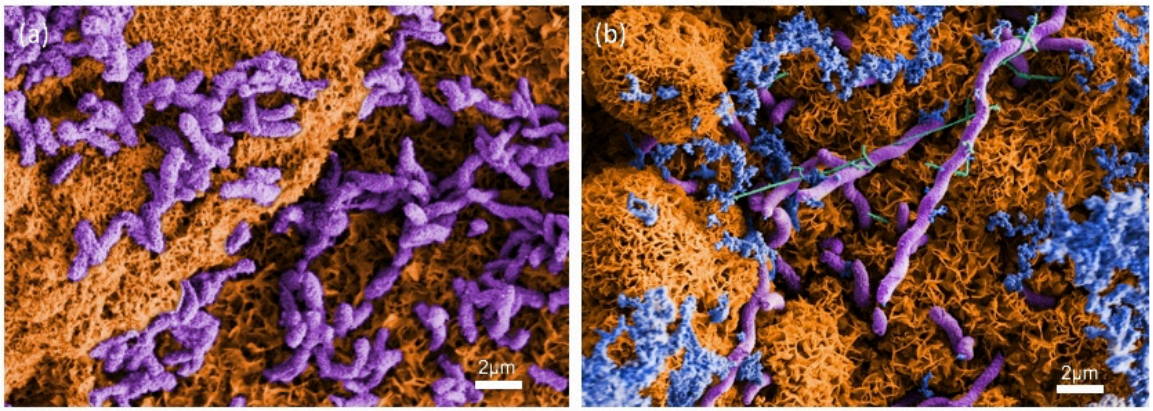


Figure 3. False colored field emission scanning electron microscopy images for (a) EAL and (b) conditions. The colorized structures correspond to: purple: G20 cells, gold: iron sulfides, blue: carbon-containing EPS, green: extracellular filaments.

demonstrate that hexose levels can be altered in *Desulfovibrio* biofilms (up to 50% of biomass), and in several samples allocation under EAL conditions and protein in EDL conditions. The location (intracellular vs extracellular) is unknown for the protein and carbohydrate allocation. The biofilm composition data suggest that the biofilms responded differently to different types of energy restriction and coincides with previous work that has shown *Desulfovibrio* biofilm has altered physiology (i.e. electron flow is altered) even when compared to sulfate-reducing planktonic cells (Clark et al. 2012).

Images were taken of the EAL and EDL biofilm cross-sections to measure biofilm thickness and show the distribution of *Desulfovibrio* G20 cells. The EAL biofilm (~200 μm) was approximately fourfold thicker than the ~50 μm EDL biofilm (Figure 4). The accumulation of corrosion products may aid in forming a textured surface to attach to, as well as an extracellular matrix to grow within; however, the accumulation of thicker biofilms under EAL conditions was not associated with increased corrosion.

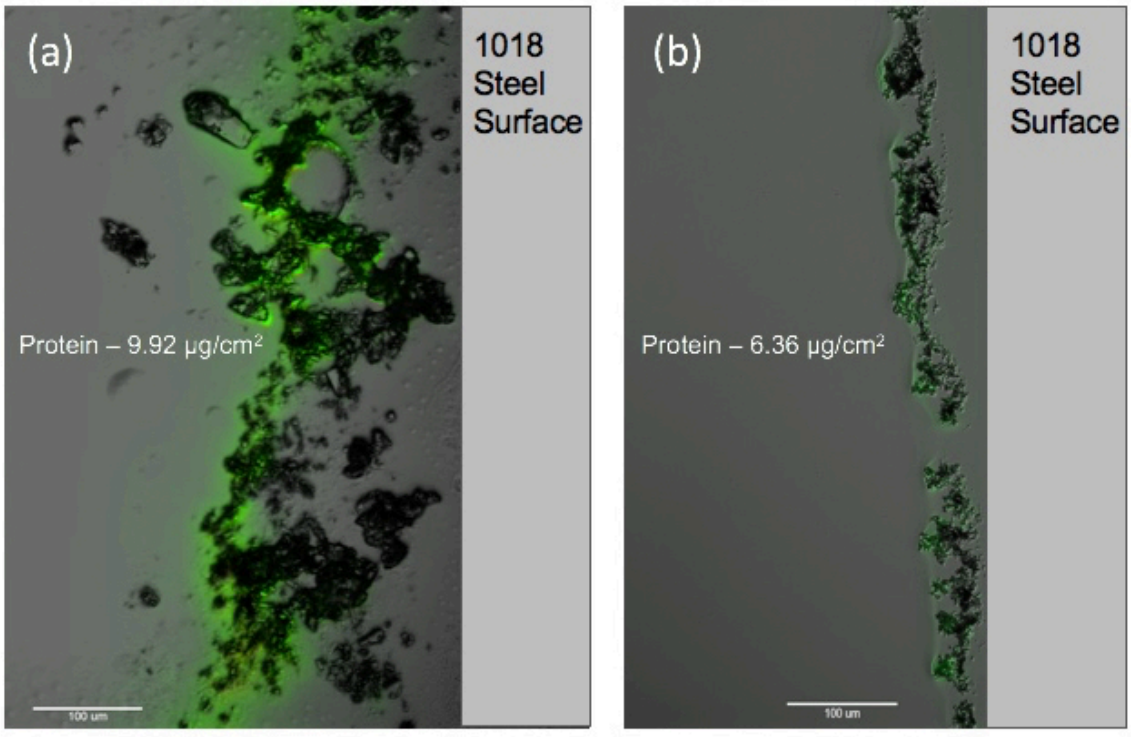


Figure 4. Epifluorescence microscopy images of thin-sectioned biofilm cross sections grown on 1018 carbon steel under (a) EAL and (b) EDL conditions. G20 cells are stained green. Substratum (steel surface) is on the right.

The availability of more carbon source likely contributed to thicker biofilm at the 192 h time point on glass and 316 steel under EAL conditions than compared to EDL conditions. The 1018 steel biofilms had higher hexose levels than protein under both

EAL and EDL conditions. Previous research by Clark et al. (2006) showed protein to be the major component of *D. vulgaris* Hildenborough (DvH) biofilms, with carbohydrate levels being relatively low. The current observations with glass and steel under EAL and EDL demonstrate that hexose levels can be altered in *Desulfovibrio* biofilms (up to 50% of biomass), and in several samples accounted for a majority of the biomass. Although DvH and G20 are both members of the genus *Desulfovibrio*, there are significant physiological differences between the two microorganisms. Under the EDL condition, there is significantly less protein and hexose on the glass and 316 steel surfaces than on the 1018 steel. Though G20 was fed the same levels of nutrients on all surfaces under the EDL condition, the protein levels were increased on 1018 compared to glass and 316.

Lactate/acetate levels

Lactate and acetate levels were measured from the biofilm reactors to assess growth physiology under biofilm reactor conditions (Figures S1, S2, and S3 in Supplemental material). Typically for *Desulfovibrio* species, lactate is converted to acetate in a 1:1 ratio (Equation 1). Because G20 consumes lactate and sulfate in a 2:1 ratio, the 15 mM of available sulfate allows G20 to oxidize 30 mM (of the 50 mM available in the EAL condition) lactate, producing 30 mM of acetate. Measured levels of lactate and acetate were similar to predicted stoichiometries (Figure S1). Under the EAL condition (50 mM lactate:15 mM sulfate) *Desulfovibrio* G20 used slightly more than 30 mM of the 50 mM lactate available, corresponding to 15 mM lactate in the effluent for all three surface types. Theoretically, there should be 20 mM lactate remaining under this condition and the missing carbon likely was used for biomass biosynthesis. The EAL

acetate levels were ~30 mM at 50 h and remained near this level at the last time point (192 h). Under the EDL condition, which contained 15 mM lactate:15 mM sulfate, growth would be limited by lactate, which is expected to be entirely consumed. Within 50 h, lactate was not detectable in the EDL reactors after inoculation and remained below detection during reactor operation. With all of the lactate being consumed, the EDL acetate levels would be expected to be at 15 mM. Acetate levels reached ~12 mM at 50 h and remained at this level during reactor operation, likely representing carbon incorporation into biomass (Figure S1).

Sulfate levels

Under the EAL condition (50:15), as expected, the sulfate levels approached 2 mM or lower at 50 h and remained almost non-detectable during reactor operation for all three surface types (Figure S2). According to the 2:1 ratio of lactate:sulfate consumption, the EDL condition (which contained 15 mM lactate:15 mM sulfate) would theoretically have 7.5 mM sulfate remaining in the medium. The EDL reactors (all surface types) approached 4 to 6 mM during reactor operation (Figure S2). While the measured sulfate levels are close to theoretical, there could have been some additional sulfate reduction dependent upon the oxidation of biomass in the reactor system (or $Fe^0$ from the CS).

Sulfide levels

*Desulfovibrio* G20 reduces sulfate to sulfide, and sulfide levels were measured for both the planktonic and biofilm fractions normalized to protein levels for a given volume (planktonic) or surface area (biofilm) (Figure S3). Within each nutritionally limiting condition, the three surface types had similar planktonic sulfide concentrations; however,

greater variation was observed at the last time point for EAL samples. The EAL planktonic samples maintained ~1 to 2 μg $\mu g^{-1}$ (sulfide/protein) for each surface type, and the EDL condition maintained ~0.5 μg $\mu g^{-1}$ (sulfide/protein) for each surface type (Figure S3). The results indicate that aqueous phase sulfide levels were higher under EAL conditions compared to EDL conditions for all tested surface types, and from a metal interaction perspective, higher sulfide levels generally translate to increased corrosion rates of CS (Dinh et al. 2004). The concentration of sulfide differed in biofilms grown on different surfaces (Figure S3). Under both EAL and EDL conditions, sulfide levels were higher on 1018 than on 316 steel or glass. EDL biofilms on average had higher sulfide levels, especially on 1018 CS, than EAL biofilms. Despite the fact there was a thinner biofilm on 1018 under the EDL condition (Figure 2), the G20 biofilm produced more sulfide per unit surface area than under the EAL condition. This result was unexpected because the planktonic sulfide was lower under EDL compared to the EAL condition and suggested altered physiological conditions under the different energy restriction conditions (e.g. more sulfide associated with biofilm biomass).

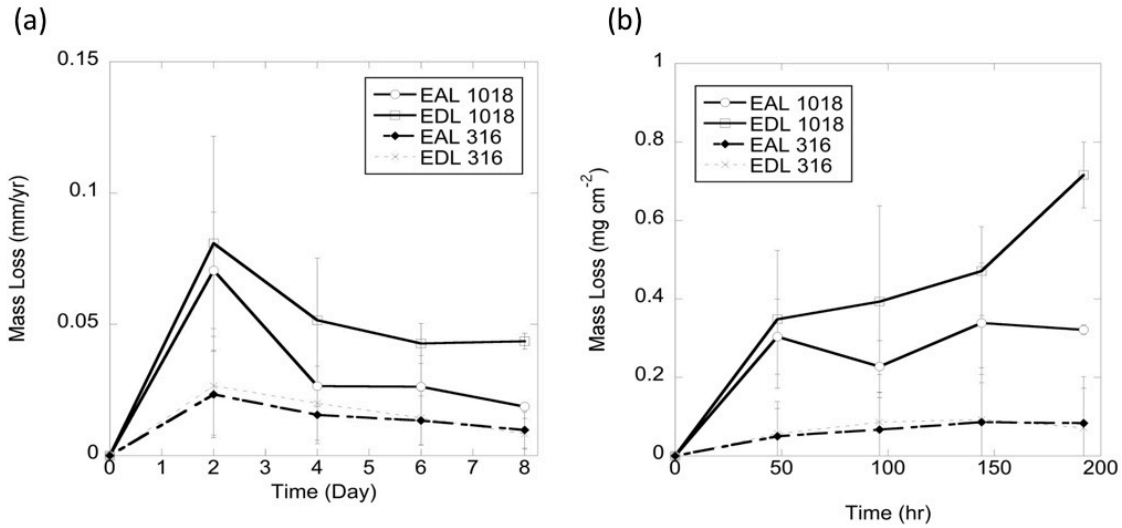


Figure 5. (a) Corrosion rate (mm y-1) for 316 SS and 1018 CS coupons during exposure to biofilm growth under EDL and EAL conditions. (b) Corrosion rate (mg cm-2) for 316 SS and 1018 CS coupons during exposure to biofilm growth under EDL and EAL conditions.

Corrosion rates

Corrosion for 316 SS was minimal while the 1018 CS showed general corrosion under the tested conditions and time (data not shown). Corrosion rates calculated from mass loss (ASTM G1-03) were higher for the 1018 CS compared to the 316 SS coupons under both EAL and EDL conditions and less biofilm (protein and carbohydrate) was maintained on the 316 over the tested time period. These results suggest that the anti-corrosive properties of 316 can impede the type of corrosion observed with 1018 steel under the EDL condition. After eight days, the estimated corrosion rate was highest for 1018 steel under the EDL condition (Figure 5). Despite the higher planktonic sulfide levels under EAL conditions and the thinner biofilm under EDL (Figures 4 and S3), the highest corrosion rate was observed under the EDL condition on 1018 steel (Figure 5). The increased EDL corrosion was further confirmed by electrochemical measurements

and differences in $R^{-1}$ values between EAL and EDL conditions on 1018 CS (~3x). Electrochemical measurements can quantify the instantaneous corrosion rate, and the initial spike in corrosion occurred when the reactor was inoculated and a passivation layer of $FeS_2$ had not yet formed, likely due to abiotic processes. The EDL condition on 1018 steel had elevated the electrochemical corrosion rate, and increased corrosion has also been observed by Xu and Gu (2014) and Chen et al. (2015) when *Desulfovibrio* biofilms were starved of nutrients under batch conditions.

Biofilm contact

In order to evaluate the importance of biofilm formation and presence on the metal surface for corrosion, biofilm formation on the metal was prevented by incubating 1018 CS coupons in sealed 6–8 kD molecular weight cutoff dialysis tubing suspended in a CDC biofilm reactor growing *Desulfovibrio* G20. In addition, the same reactor contained coupons not in dialysis tubing (normal) to allow direct biofilm colonization and planktonic cell growth in the bulk medium. Under the normal condition where biofilm can form directly on the metal surface, EDL showed increased corrosion (mass loss) compared to EAL; however, under the protected condition corrosion was decreased for both EDL and EAL (Figure 6). Moreover, the reduction in corrosion was greater (approximately threefold decline) for the protected metal under the EDL condition (Figure 6). The results demonstrate that SRB biofilm attachment to and biofilm formation

on the 1018 CS surface was needed for maximal corrosion rates.

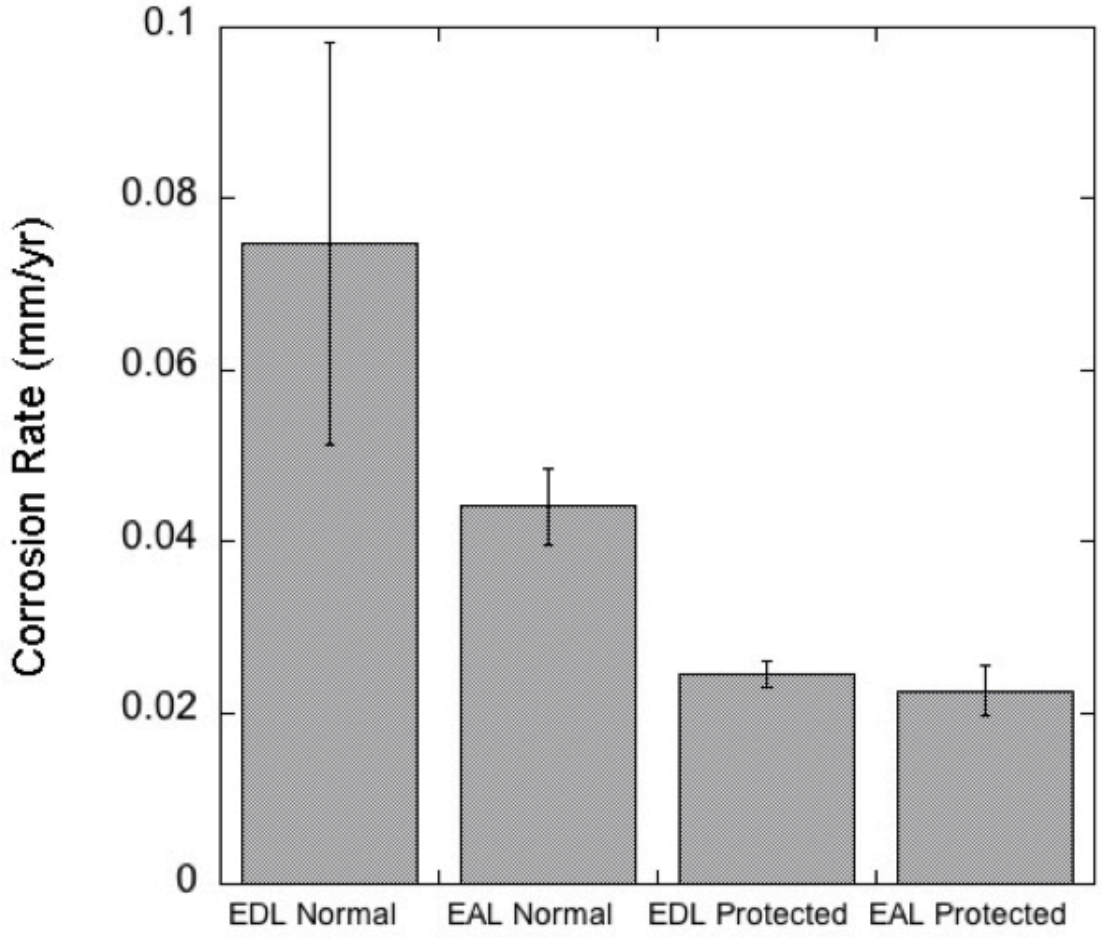


Figure 6. Corrosion rate of 1018 carbon steel coupons under normal exposure to SRB culture compared to coupons protected inside of dialysis tubing submerged in culture.

Metabolomic analysis on biofilm

Having observed a difference in corrosion rate between EAL and EDL biofilms on 1018 CS, the mechanism involved in the increased corrosion caused by EDL grown *Desulfovibrio* G20 was unknown. Metabolomic mass spectrometry analyses combined with XCMS data processing (Smith et al. 2006) was done on biofilm scraped from 1018 CS grown under EAL and EDL conditions. A total of 1,157 features were detected

between EDL and EAL ($p < 0.01$) (Figure 7). Based on significance values and MS/MS confirmation, three metabolites of interest displayed significant fold changes (10- to 20-fold) (Table 2).

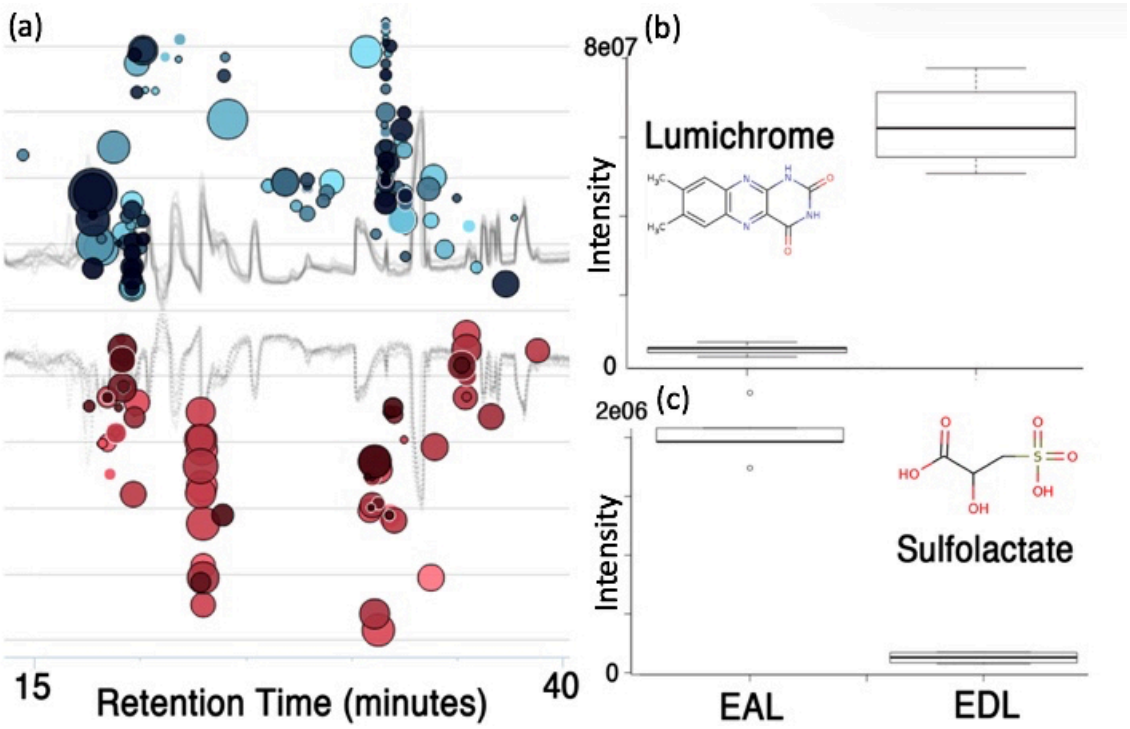


Figure 7. (a) Cloud plot of dysregulated features comparing EAL vs EDL conditions on 1018 carbon steel. (b) Intensities of lumichrome peaks EAL vs EDL. (c) Intensities of sulfolactate peaks EAL vs. EDL.

| Metabolite | Condition | Fold Change | p-value | q-value |
|---|---|---|---|---|
| Sulfolactate | Up in EAL | 15.7 | 0.00003 | 0.00229 |
| Cysteine-s-sulfate-related | Up in EAL | 20.1 | 0.0025 | 0.01224 |
| Lumichrome (metabolite of riboflavin) | Up in EDL | 10.1 | 0.00185 | 0.00185 |

Table 2. Metabolites that differ significantly between EAL vs. EDL and have been confirmed with MS/MS.

Sulfur cycling

One of the confirmed dysregulated metabolites, sulfolactate, was increased 15.7-fold under EAL conditions on 1018 steel (Figure 7). Sulfolactate is a sulfonate compound related to the cysteine/methionine processing pathways in some microorganisms. A complete pathway from cysteine to sulfolactate is not predicted in the Desulfovibrio G20 genome whereas the genome is annotated to contain an aminotransferase that could convert cysteate to sulfopyruvate (E.C. 2.6.1.1; KEGG). However, the genome annotation does not contain an identified enzyme to catalyze the conversion of sulfopyruvate to sulfolactate. The commonly identified enzymes with this activity include sulfolactate dehydrogenase (R and S) and malate dehydrogenase and would provide additional electron acceptor (reduction of sulfopyruvate to sulfolactate) via recycling of cysteine through cysteate and could account for the elevated sulfolactate levels that were detected under EAL conditions. The Desulfovibrio G20 genome is annotated to have a gene that encodes a protein with potential malate dehydrogenase activity (Dde1008, $NAD^+$-linked). Sequence comparisons and biochemical studies have recently expanded the functionality of previously annotated malate and lactate dehydrogenases to have other activities such as sulfolactate dehydrogenase (Muramatsu et al. 2005); however, the potential role of Dde1008 in conversion of sulfopyruvate to sulfolactate is unknown. The source of sulfopyruvate may be from the degradation of the sulfur-containing amino acids cysteine and methionine, taking advantage of normal amino acid recycling as a means of generating sulfite (an additional electron acceptor). Other members of the Desulfovibrio family have demonstrated growth capabilities on sulfonate compounds such as cysteate or isethionate, as is the case with *Desulfovibrio desulfuricans* IC1 (Lie et al. 1996).

Cysteate is the product from cysteine degradation and can be converted to 3-sulfopyruvate by cysteine lyase. However, cysteine lyase has not been identified in the *Desulfovibrio* G20 genome via annotation. The *Desulfovibrio* G20 genome is annotated to have the gene for aspartate aminotransferase (EC 2.6.1.1) that can convert cysteate to 3-sulfopyruvate. To explore whether G20 was able to utilize cysteate, planktonic growth with cysteate alone or with lactate was tested at similar ratios. Significant growth with cysteate was not observed with the tested growth medium (data not shown), and these results suggest that *Desulfovibrio* G20 cannot utilize cysteate as a sole source of carbon and energy. Under the EAL condition, another significant metabolite that was identified at increased levels with high confidence was a cysteine-S-sulfate-related molecule (Table 2). Given the complexity of S-cycling, particularly in SRB, the exact role of this compound is not known. A cysteine-S-sulfate molecule could be involved in cycling any available intracellular sulfate, but a known annotated pathway has not been identified in *Desulfovibrio* G20. The results presented demonstrate the importance of S-cycling in *Desulfovibrio* G20 under EAL conditions, and further work is needed to fully elucidate the turnover of methionine/ cysteine in SRBs and the potential effect on growth when limited for sulfate.

Role of electron shuttles

Under the EDL condition with increased 1018 steel corrosion, the metabolite lumichrome was increased 10-fold compared to the EAL condition (Table 2; Figure 7). Lumichrome is a by-product of riboflavin biosynthesis, and riboflavin is a predicted intermediate for the biosynthesis of FAD and FMN in both *D. vulgaris* and *Desulfovibrio* G20 genomes

(Figure 8). *Desulfovibrio* G20 has annotated genes for the biosynthesis of riboflavin to FMN and FAD but does not have an annotated gene for the riboflavinase that can catalyze the conversion of riboflavin to lumichrome and ribitol (Figure 8). However, photolysis has been shown to drive the formation of lumichrome from riboflavin (Treadwell and Metzler 1972; Birss et al. 1997), particularly in anoxic conditions even under normal laboratory lighting, and the current anoxic reactors were exposed to ambient light during growth and the samples were processed in the light.

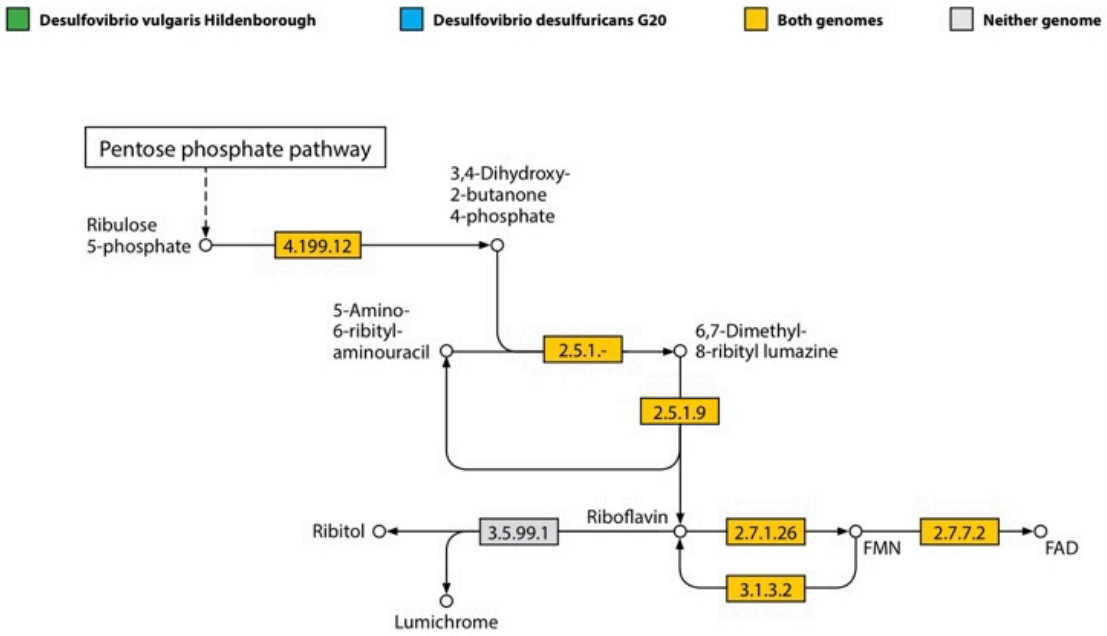


Figure 8. Predicted riboflavin biosynthesis pathway in *Desulfovibrio* G20 and *D. vulgaris* based on KEGG predictions.

The solubility of riboflavin, FMN, and FAD in water (0.12, 92, and 50 g $l^{-1}$, respectively) is much higher than lumichrome (0.0048 g $l^{-1}$). In addition, lumichrome has been shown to be an inhibitor of flavin oxidoreductase in Escherichia coli (Fieschi et al. 1995), and a protein family (dodecins) with high preference for lumichrome has been suggested to

play a role in “trapping” riboflavin photolytic degradation products (i.e. lumichrome) (Grininger et al. 2006). While lumichrome could play an unknown role in biofilm physiology, it is more likely that lumichrome is a photolytic by-product from riboflavin that has been shown previously to impact metal corrosion in SRBs (Kato 2016; Chen et al. 2015). Based upon these data and given that *Desulfovibrio* G20 does not have an annotated riboflavinase, the detected lumichrome is likely related to riboflavin or flavin family molecules (i.e. FMN and/or FAD).

Moreover, two metabolic features with the likely identity of FAD were increased 2.8- and 3.6-fold under the EDL condition. The p-values for these were 0.2, and while not meeting the statistical cutoff of 0.01, the FAD molecules likely have biological (and corrosion) significance. Recent work in *Shewanella oneidensis* has demonstrated a role for FMN and riboflavin in which one-electron and two-electron mechanisms can play extracellular electron transfer roles under different conditions (Brutinel and Gralnick 2012; Okamoto et al. 2013). Interestingly, recent research demonstrated that adding FAD or riboflavin to *D. vulgaris* cultures increased metal corrosion rates in batch (Kato 2016; Chen et al. 2015). The present data further extend the role of flavin cofactors in metal corrosion and demonstrates a physiological condition (i.e. EDL) in which biofilm would produce elevated levels of these compounds under metal-corroding conditions.

When considering the EDL condition and increased corrosion, elemental Fe could serve as a source of electrons for the biofilm under EET-MIC. The present data further support the hypothesis that endogenous flavin compounds (i.e. riboflavin, FMN, and FAD) could serve the role of extracellular electron transfer mediators for biofilm grown

on 1018 CS. When considering riboflavin, a one-electron transfer (semiquinone flavin) from $Fe^0$ ($E_m$ = -0.167 V; Ksenzhek and Petrova 1983) would provide a favorable DG' value (-52 kJ) and if the semiquinone was further reduced the $DG^{0'}$ value of the subsequent reaction would be -34 kJ. For the FMN/FMNH2 couple ($E^{0'}$ = -0.21 V; Mayhew 1999), a two-electron transfer from $Fe^0$ would provide a favorable $\Delta G^{0'}$ value (-44 kJ). For the FAD/ FADH2 couple ($E_0'$ = -0.3 V; Curley et al. 1991), a two-electron transfer from $Fe^0$ would provide a favorable $\Delta G^{0'}$ value (-27 kJ). Based solely upon thermodynamic estimations under standard conditions, riboflavin would be the preferred molecule, and this corresponds to more corrosion previously observed with riboflavin compared to FAD with *D. vulgaris* on 1018 CS (Li et al. 2015). The results indicate that *Desulfovibrio* G20 biofilms likely produced endogenous flavin-like molecules when grown under EDL conditions on a metal surface.

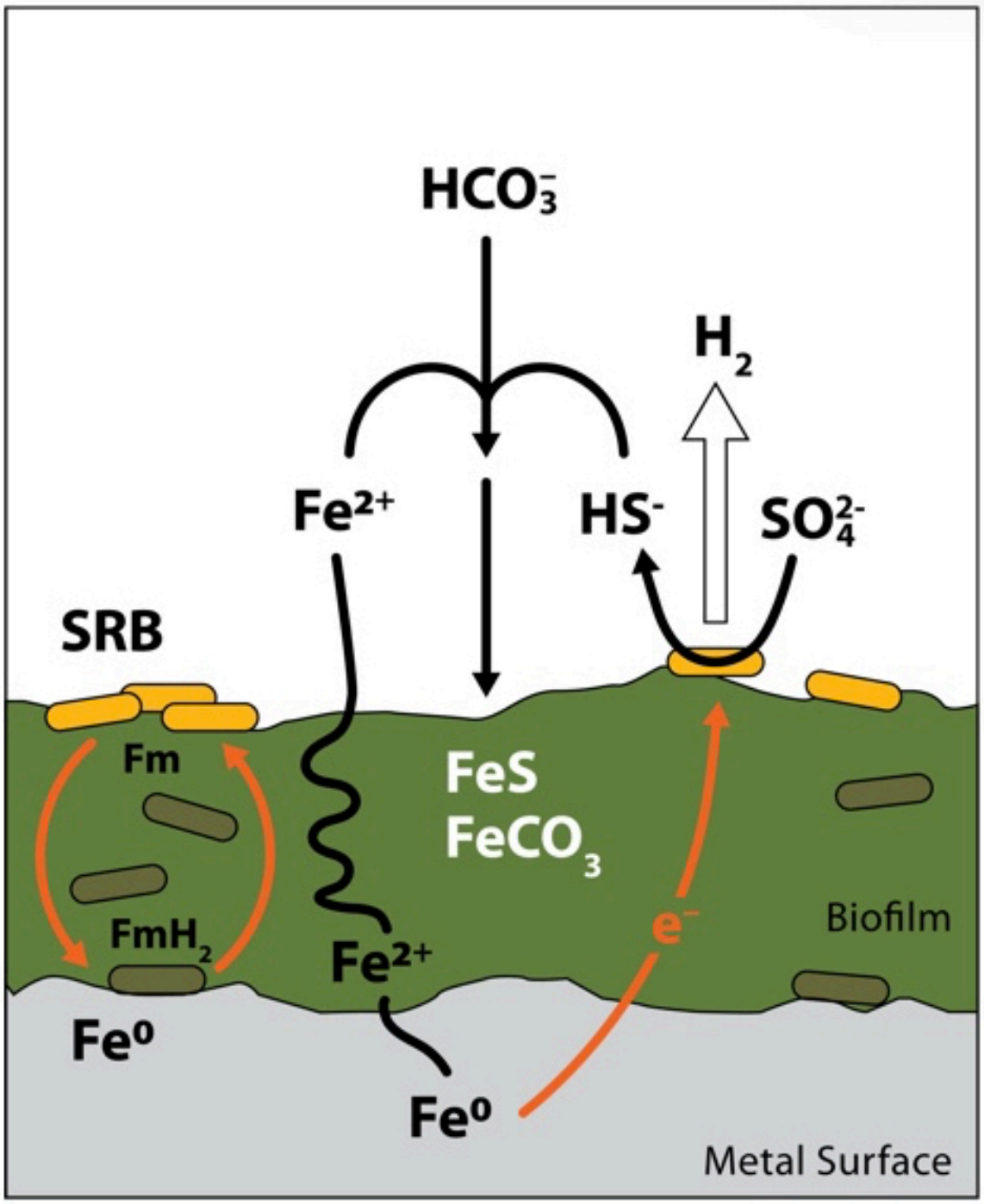


Figure 9. Classic model of corrosion with the addition of cycling endogenously produced flavin-based extracellular electron transfer molecules (Fm) with elemental $Fe^0$ within the biofilm as a form of EET (extracellular electron transfer)-MIC.

## Conclusions

The results demonstrate that energy restriction (EAL vs EDL) greatly impacted biofilm growth and the physiology of *Desulfovibrio* G20 biofilms grown on CS. Less corrosion was observed on 316 SS compared to 1018 CS for both the EAL and EDL condition; however, the EDL condition promoted more corrosion of 1018 steel despite a thinner biofilm with decreased aqueous sulfide levels compared to the EAL condition. However, despite being limited for electrons under the EDL condition, more biofilm-associated sulfide was observed and corrosion was increased. In addition, the increased corrosion was dependent upon biofilm interaction with the metal surface. These results suggest that the metal surface was serving as an additional electron source (i.e. $Fe^0$ ). Untargeted metabolomics indicated that the EAL grown biofilm on 1018 steel altered cysteine/methionine cycling while the EDL-grown biofilm had elevated levels of flavin-like compounds. The flavin molecules likely serve a role in extracellular electron transfer when interacting with the metal surface ($Fe^0$) in EET-MIC (Figure 9), and this was further supported by the need for biofilm to interface directly with the metal surface for elevated corrosion. The endogenously produced flavin molecules likely play a role in harvesting electrons from $Fe^0$ when limited for electron donor, allowing continued biofilm growth under nutrient-restricted conditions. In essence, when lactate was limiting, sulfate reduction was coupled to $Fe^0$ oxidation at the steel surface, thus promoting increased CS corrosion. The results also suggest that the EDL condition could be relevant to the common practice of seawater injection into reservoir formations for enhanced oil extraction. Seawater has an average sulfate level of 28 mM, nearly twice the

concentration used in this study. In hydrocarbon environments carbon/electron sources can be limiting due to slower degradation rates and/or competition for resources. Thus, the introduction of increased sulfate levels could shift the nutrient ratio in the EDL direction, thereby promoting increased corrosion rates via EET-MIC. Further work is needed to better understand the impact of energy imbalance on sulfate reducing communities in different environments and the outcome on CS materials.

References

McCarty, P. L. Energetics and bacterial growth. *Organic compounds in aquatic environments* **1**, 157–172 (1971).

Grininger, M., Zeth, K. & Oesterhelt, D. Dodecins: a family of lumichrome binding proteins. *J. Mol. Biol.* **357**, 842–857 (2006).

Fieschi, F., Nivière, V., Frier, C., Décout, J. L. & Fontecave, M. The mechanism and substrate specificity of the NADPH:flavin oxidoreductase from Escherichia coli. *J. Biol. Chem.* **270**, 30392–30400 (1995).

Birss, V. I., Guha-Thakurta, S., McGarvey, C. E., Quach, S. & Vanýsek, P. An electrochemical study of the photolysis of adsorbed flavins. *J. Electroanal. Chem.* **423**, 13–21 (1997).

Treadwell, G. E. & Metzler, D. E. Photoconversion of riboflavin to lumichrome in plant tissues. *Plant Physiol.* **49**, 991–993 (1972).

Okamoto, A., Hashimoto, K., Nealson, K. H. & Nakamura, R. Rate enhancement of bacterial extracellular electron transport involves bound flavin semiquinones. *Proc. Natl. Acad. Sci. U. S. A.* **110**, 7856–7861 (2013).

Brutinel, E. D. & Gralnick, J. A. Shuttling happens: soluble flavin mediators of extracellular electron transfer in Shewanella. *Appl. Microbiol. Biotechnol.* **93**, 41–48 (2012).

Curley, G. P., Carr, M. C., Mayhew, S. G. & Voordouw, G. Redox and flavin-binding properties of recombinant flavodoxin from Desulfovibrio vulgaris (Hildenborough). *Eur. J. Biochem.* **202**, 1091–1100 (1991).

Ksenzhek, O. S. & Petrova, S. A. Electrochemical properties of flavins in aqueous solutions. *J. Electroanal. Chem. Interfacial Electrochem.* **156**, 105–127 (1983).

Muramatsu, H. *et al.* A new family of NAD(P)H-dependent oxidoreductases distinct from conventional Rossmann-fold proteins. *J. Biosci. Bioeng.* **99**, 541–547 (2005).

Zhou, J. *et al.* How sulphate-reducing microorganisms cope with stress: lessons from systems biology. *Nat. Rev. Microbiol.* **9**, 452–466 (2011).

Little, B. J. & Lee, J. S. *Microbiologically Influenced Corrosion*. (John Wiley & Sons, 2007).

Nealson, K. H. & Saffarini, D. Iron and manganese in anaerobic respiration:

environmental significance, physiology, and regulation. *Annu. Rev. Microbiol.* **48**, 311–343 (1994).

Bonifay, V. *et al.* Metabolomic and Metagenomic Analysis of Two Crude Oil Production Pipelines Experiencing Differential Rates of Corrosion. *Front. Microbiol.* **8**, 99 (2017).

Mayhew, S. G. The effects of pH and semiquinone formation on the oxidation--reduction potentials of flavin mononucleotide: a reappraisal. *Eur. J. Biochem.* **265**, 698–702 (1999).

Malinauskas, A., Ruzgas, T. & Gorton, L. Tuning the redox potential of riboflavin by zirconium phosphate in carbon paste electrodes. *Bioelectrochem. Bioenerg.* **49**, 21–27 (1999).

Thauer, R. K., Stackebrandt, E. & Hamilton, W. A. Energy metabolism and phylogenetic diversity of sulphate-reducing bacteria. *Sulphate-reducing bacteria: Environmental and engineered systems* 1–37 (2007).

Clark, M. E., Edelmann, R. E., Duley, M. L., Wall, J. D. & Fields, M. W. Biofilm formation in Desulfovibrio vulgaris Hildenborough is dependent upon protein filaments. *Environ. Microbiol.* **9**, 2844–2854 (2007).

Klonowska, A. *et al.* Hexavalent chromium reduction in Desulfovibrio vulgaris Hildenborough causes transitory inhibition of sulfate reduction and cell growth. *Appl. Microbiol. Biotechnol.* **78**, 1007–1016 (2008).

Dinh, H. T. *et al.* Iron corrosion by novel anaerobic microorganisms. *Nature* **427**, 829–832 (2004).

Kato, S. Microbial extracellular electron transfer and its relevance to iron corrosion. *Microb. Biotechnol.* **9**, 141–148 (2016).

Huan, T. *et al.* Systems biology guided by XCMS Online metabolomics. *Nat. Methods* **14**, 461–462 (2017).

Clark, M. E. *et al.* Transcriptomic and proteomic analyses of Desulfovibrio vulgaris biofilms: Carbon and energy flow contribute to the distinct biofilm growth state. *BMC Genomics* **13**, (2012).

Clark, M. E. *et al.* Temporal Transcriptomic Analysis as Desulfovibrio vulgaris Hildenborough Transitions into Stationary Phase during Electron Donor Depletion. *Appl. Environ. Microbiol.* **72**, 5578–5588 (2006).

Xu, D. & Gu, T. Carbon source starvation triggered more aggressive corrosion against carbon steel by the Desulfovibrio vulgaris biofilm. *Int. Biodeterior. Biodegradation* **91**,

74–81 (2014).

Zhang, P., Xu, D., Li, Y., Yang, K. & Gu, T. Electron mediators accelerate the microbiologically influenced corrosion of 304 stainless steel by the Desulfovibrio vulgaris biofilm. *Bioelectrochemistry* **101**, 14–21 (2015).

Chen, Y. *et al.* Long-term survival of Desulfovibrio vulgaris on carbon steel and associated pitting corrosion. *Corros. Sci.* doi:10.1016/j.corsci.2014.09.016

Hauser, L. J. *et al.* Complete Genome Sequence and Updated Annotation of Desulfovibrio alaskensis G20. *J. Bacteriol.* **193**, 4268–4269 (2011).

Smith, C. A., Want, E. J., O'Maille, G., Abagyan, R. & Siuzdak, G. XCMS: Processing Mass Spectrometry Data for Metabolite Profiling Using Nonlinear Peak Alignment, Matching, and Identification. *Anal. Chem.* **78**, 779–787 (2006).

Ivanisevic, J. *et al.* Toward 'Omic Scale Metabolite Profiling: A Dual Separation–Mass Spectrometry Approach for Coverage of Lipid and Central Carbon Metabolism. *Anal. Chem.* **85**, 6876–6884 (2013).

Benton, H. P. *et al.* Autonomous Metabolomics for Rapid Metabolite Identification in Global Profiling. *Anal. Chem.* **87**, 884–891 (2015).

Li, H. *et al.* Extracellular Electron Transfer Is a Bottleneck in the Microbiologically Influenced Corrosion of C1018 Carbon Steel by the Biofilm of Sulfate-Reducing Bacterium Desulfovibrio vulgaris. *PLoS One* **10**, e0136183 (2015).

Enning, D. & Garrelfs, J. Corrosion of iron by sulfate-reducing bacteria: new views of an old problem. *Appl. Environ. Microbiol.* **80**, 1226–1236 (2014).

Venzlaff, H. *et al.* Accelerated cathodic reaction in microbial corrosion of iron due to direct electron uptake by sulfate-reducing bacteria. *Corros. Sci.* **66**, 88–96 (2013).

Montenegro-Burke, J. R. *et al.* Smartphone Analytics: Mobilizing the Lab into the Cloud for Omic-Scale Analyses. *Anal. Chem.* **88**, (2016).

Supplemental Information

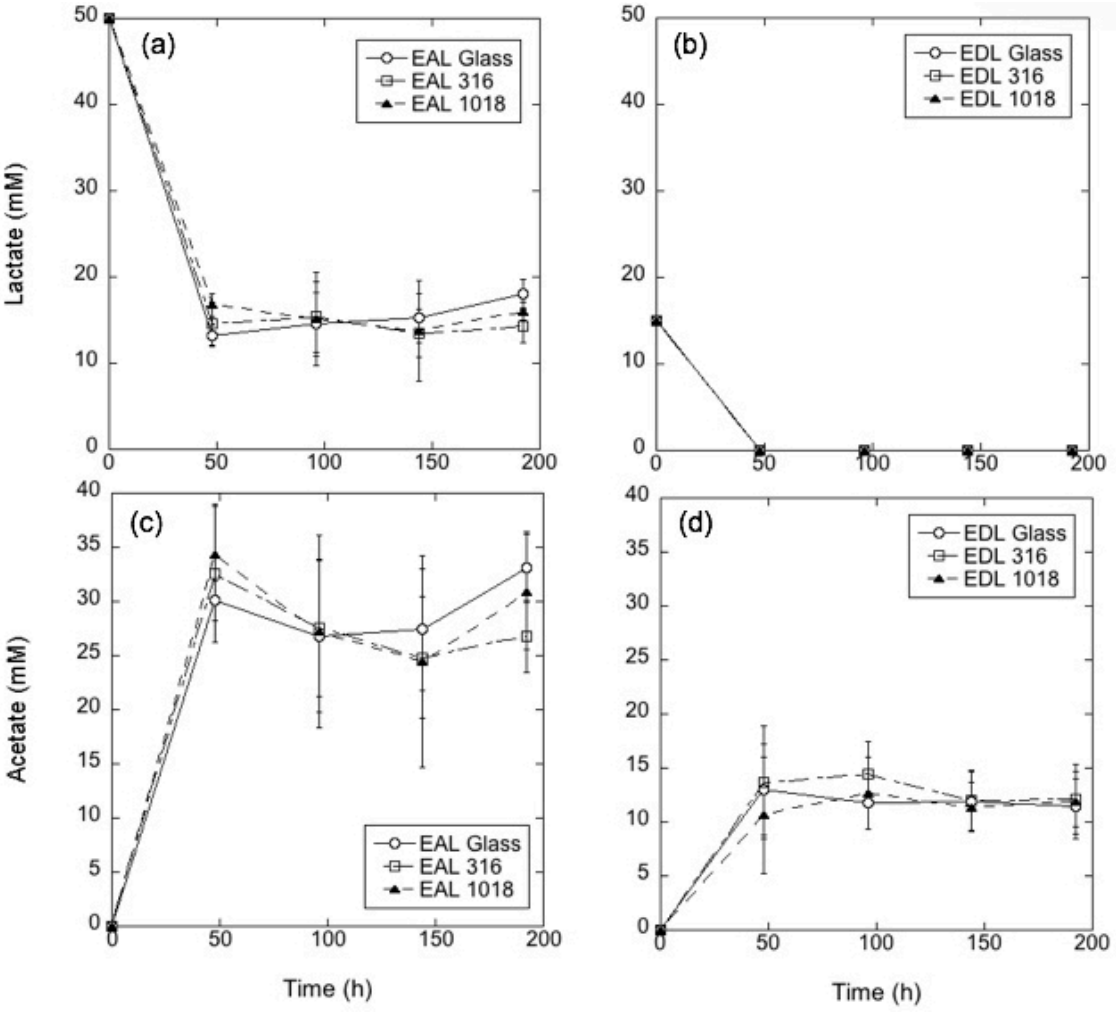


Figure S1. Carbon utilization on glass, 316 stainless steel, and 1018 carbon steel surfaces. (a) Lactate levels under EAL conditions (b) Lactate levels under EDL conditions. (c) Acetate levels under EAL conditions. (d) Acetate levels under EDL conditions.

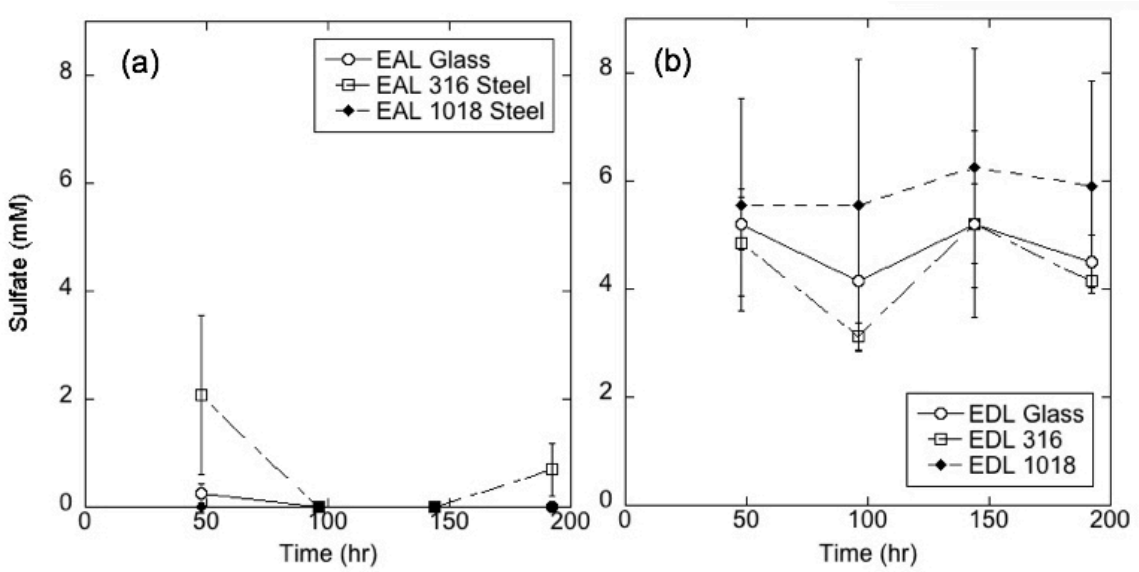


Figure S2. Sulfate utilization on glass, 316 stainless steel, and 1018 carbon steel surfaces. (a) Sulfate levels under EAL conditions (b) Sulfate levels under EDL conditions.

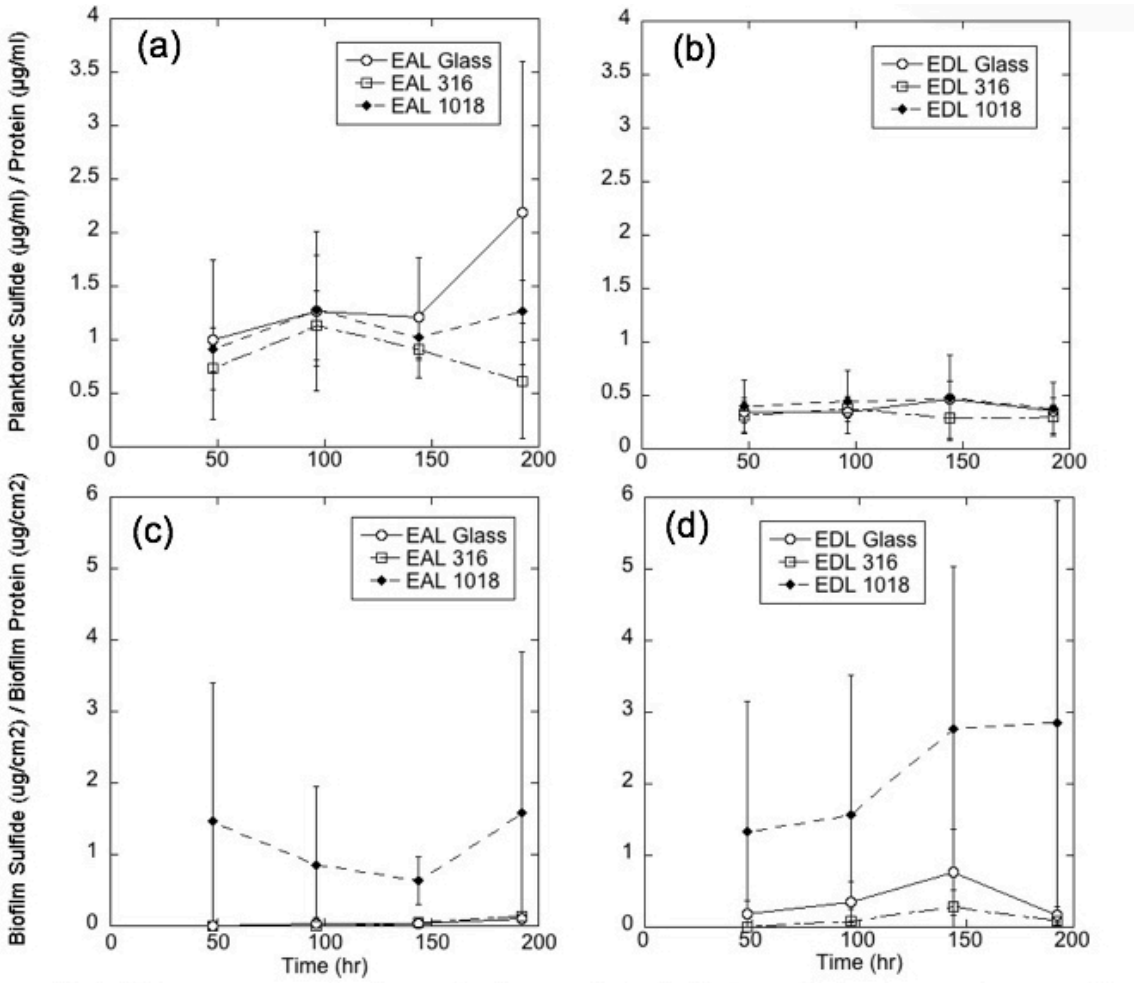


Figure 10. Sulfide production was measured and normalized to protein levels. Biofilm sulfide levels were normalized to surface area and protein levels. (a) Planktonic sulfide levels under EAL conditions (b) Planktonic sulfide levels under EDL conditions. (c) Biofilm sulfide levels under EAL conditions (d) Biofilm sulfide levels under EDL conditions.

# CHAPTER THREE

## LARGE EXTRACELLULAR PROTEINS SENSE HYDRODYNAMIC FORCE AND DRIVE BIOFILM FORMATION IN *DESULFOVIBRIO VULGARIS*

### Contributions of Authors and Co-Authors

Manuscript in Chapter 3

Author: Gregory P. Krantz

Contributions: Developed experimental design, performed experiments, analyzed data, wrote and revised the manuscript.

Author: Peter J. Walian

Contributions: Performed experiments, analyzed data, wrote and revised the manuscript.

Author: Marty Boyl-Davis

Contributions: Performed experiments.

Author: Kara B. De Leon

Contributions: Performed experiments, analyzed data, wrote and revised the manuscript.

Author: Judy D. Wall

Contributions: Analyzed data, wrote and revised the manuscript.

Author: Matthew W. Fields

Contributions: Developed experimental design, analyzed data, wrote and revised the manuscript.

Manuscript Information

Gregory P. Krantz, Peter J. Walian, Marty Boyl-Davis, Kara De Leon, Judy D. Wall, &

Matthew W. Fields

Status of Manuscript:
__X__ Prepared for submission to a peer-reviewed journal
____ Officially submitted to a peer-reviewed journal
____ Accepted by a peer-reviewed journal

## Abstract

Proteins can be a major component of the extracellular polymeric substance in biofilms of sulfate-reducing bacteria of the genus *Desulfovibrio.* However, very little is known about the potential functions of these proteins in biofilm formation, maintenance, or activity. Two large proteins encoded in genes of *Desulfovibrio vulgaris* Hildenborough (DvH) have previously been shown to be expressed and enriched in the extracellular fraction of biofilms. The two proteins, referred to as DVU1012 and DVU1545, were detected in the extracellular biofilm fraction of a monoculture DvH biofilm. Protein DVU1012 is predicted to be a 3,038 amino acid polypeptide that contains both von Willebrand (IPR002035) and protease (IPR011049) domains. Protein DVU1545 is predicted to be a 2,414 amino acid polypeptide with hemolysin-like domains. Both proteins have type 1 secretion signals and $Ca^{2+}$-binding domains. Mutant strains (Δ*dvu1012* or Δ*dvu1545*) of single deletions of each gene were able to grow and maintain biofilm under the tested continuous conditions in biofilm reactors (Reynold's number (Re)=621 and 192 h growth). Despite similar protein levels, electron microscopy indicated that the Δ*dvu1012* and Δ*dvu1545* biofilms differed in appearance. The double mutant strain (Δ*dvu1012/*Δ*dvu1545*) lagged in biofilm formation during the first 144 h of growth (~3.5x less protein) and had approximately 1.8x less protein at 192 h. Wild-type biofilms grown under conditions of an increased Reynold's number (Re=993) had increased biofilm biomass (2.8x higher protein) compared to biofilm grown at the lower shear (Re=621). However, the Δ*dvu1012/*Δ*dvu1545* mutant strain had even lower biofilm biomass at the higher shear force and the double mutant biofilm biomass was 12.8x lower after the 192 h growth period compared to wild-type biofilm. Structural predictions with I-TASSER (Iterative Threading ASSEmbly Refinement) identified homology with large-pore toxin proteins and S-layer proteins with both membrane-spanning and cytoplasmic/extra-cytoplasmic regions. Protein DVU1012 was enriched in wild-type biofilm relative to planktonic biomass and electron microscopy of negatively-stained particles indicates a hollow cylinder-like structure with an estimated inner diameter range of 3.5 to 5.5 nm. Overall, the results demonstrate that DVU1012 and DVU1545 are novel structural proteins important to *Desulfovibrio* biofilm formation that likely play a role in coordination of cellular response to shear force and biofilm formation/maintenance.

## Introduction

The biofilm EPS (exo-polymer substance) is an all-inclusive term for the extracellular macromolecules that enable cells to adhere to surfaces and each other, and the understanding of the biofilm matrix has progressed to include, but are not limited to polysaccharides, extracellular DNA, membrane vesicles, cell debris from lysed cells, enzymes, and structural proteins (Flemming and Wingender, 2010; Flemming, 2016). While some of these components have been identified and a function established for a particular species, there are still many matrix components that have not been identified or described for the breadth of bacterial diversity. Moreover, the biofilm matrix is increasingly being realized to contain a variety of intra- and inter-matrix interactions that contribute and may control biofilm behavior (Schooling and Beveridge, 2006; Payne and Boles, 2016). More recently, Hooper and Burstein posited that the minimization of extracellular space in prokaryotic (*i.e.*, *Bacteria* and *Archaea*) biofilms promoted cellular associations that impacted metabolism and may have contributed to the evolution of *Eukarya* (Hooper and Burstein, 2014).

The biofilm EPS is thought to play a crucial role in the evolutionary advantages of microbial life adhered to a surface (Costerton et al. 1978) by providing adhesion and cohesion properties as well as protection from predation, dessication, and detrimental products (*e.g.*, biocides). In addition, to the many molecular components that comprise the biofilm matrix, the biofilm can serve as a local repository for cellular materials that can be utilized (or recycled) in the future (Fleming and Wingender 2010). *Desulfovibrio vulgaris* Hildenborough (DvH) is a model strain for study of the sulfate-reducing bacteria

and it produces a biofilm that is predominantly dependent upon protein when grown on a glass substrate (Clark et al., 2007; Clark et al. 2012). Many microorganisms produce polymers that promote interactions with both biotic and abiotic surfaces (Costerton et al. 1978), and historically carbohydrate/polysaccharide interactions in the biofilm matrix have been a research focus (Costerton et al., 1978; Fleming and Wingender 2010; Fleming 2016 and references therein). Therefore, much less is known about biofilm matrix proteins and the roles played in biofilm formation, maintenance, and disassembly.

Recently, bacteria such as *E. coli* and *P. fluorescens* Pf0-1 have been shown to synthesize extracellular proteins such as curli (CsgA) and LapA that play a role in binding cells together in the biofilm (Hobley et al. 2015, Smith et al. 2018). pBLAST search results of these proteins against the DvH genome produced no results for CsgA, but LapA does have homology to DVU1012, DVU1545, and the hypothetical protein DVUA0041. In addition, we previously showed that DVU1012 and DVU1545 were the most abundant peptides detected in an extracellular biofilm fraction (Clark et al., 2012) and our recent work (De Leon et al., 2017) demonstrated that DVU1012 and DVU1545 were important for biofilm formation and were exported by the type 1 secretion system (T1SS). However, little is known about these two large, extracellular proteins nor the potential roles played in biofilm formation. Here we report on initial structural studies of DVU1012 and the impacts on biofilms caused by the loss of each of these large proteins from DvH.

## Materials and Methods

### Microorganism and Growth Medium

*Desulfovibrio vulgaris* Hildenborough ATCC 29579 (DvH) was grown in a defined lactate/sulfate (LS4D) medium prepared anoxically as previously described (Clark et al., 2007). Mutant strains*Δdvu1012, Δdvu1545,* and *Δdvu1012/Δdvu1545* as well as their parental strain (Δ*upp*, uracil phosphoribosyltransferase, used as wild-type in this study), were recently described (De Leon et al., 2017). Modifications to the original recipe included adjusting the lactate and sulfate concentrations to 25 mM and 16.6mM, respectively. As previously described, no sulfide was added to the sterile media (Clark et al., 2006), and the use of resazurin in the culture medium served as a general indicator of oxidative-reduction potential (ORP). A small amount of sodium hydrosulfite (~20 μg/l) was added to the 10% resazurin solution to shift the solution from purple to pink.

### Measurement of Growth

DvH was cultured in LS4D medium at 30°C, and each condition was grown in triplicate in a Balch tube with $N_2$ headspace. Optical Density (600 nm) was measured with a UNICO 1100RS spectrophotometer (New Jersey) and compared with uninoculated medium.

### Biofilm Growth

Biofilm samples were grown in modified CDC Biofilm Reactors (Biosurface Technologies Corp., Bozeman, MT) with the headspace sparged with anoxic $N_2$ gas. Separate reactors were grown for each strain [wild-type*, Δdvu1012, Δdvu1545*,

*Δdvu1012/dvu1545*]. Reactors were inoculated with 40 ml of an exponential-phase culture with an approximate O.D.600 of 1 and allowed to grow in batch mode for approximately 24 hours at which point the medium pump was turned on at a flow rate of 0.7 ml/min ($D = 0.11^{-h}$) and continuous flow was maintained until the final samples were harvested. A stir rate of either 50 or 80rpm was used depending on desired flow regime. Glass coupon dimensions were 7.1 x 1.25 x 0.1cm. Modified coupon holders were used as previously described to provide increased material surface area (Clark et al., 2012). Biofilm coupons were removed from the reactor and biofilm was immediately removed from the coupon using a sterile scraper. Biomass was scraped into 5 ml of $dH_2O$ and vortexed prior to growth parameter measurements. Biomass was boiled for 10 minutes before being sub-sampled for protein and carbohydrate measurements.

Growth Parameter Measurements

Protein concentrations were measured with a Qubit Protein Assay Kit (Life Technologies, Carlsbad, CA). Carbohydrate concentration was measured as previously described (Clark et al. 2006). Lactate and acetate were quantified using an Ultimate 3000 High Performance Liquid Chromatography instrument with a 300mm x 7.8mm HPLC Organic Acid Analysis Aminex HPX-87H Ion Exclusion Column (Thermo Scientific, Dionex Germering, Germany). Sulfide was determined using a colorimetric copper sulfate method with sodium sulfide as the standard (Ref).

Preparation of Samples for Imaging and
Scanning Electron Microscopy

Biofilm samples were fixed to each surface by treatment in Karmovsky's Fixative (3.2% w/v paraformaldehyde, 2.5%w/w glutaraldehyde, 0.05M sodium cocodylate) for 16 h. Samples were soaked 4x in $dH_2O$ for 5 min to remove fixative. Ethanol (EtOH) dehydration involved 5 minutes in 25% EtOH, 5 minutes in 50% EtOH, 5 minutes in 75% EtOH, 15 minutes in 95% EtOH, and 2x 45 minutes in 100% EtOH before storage in 100% EtOH. Dehydrated samples were dried in a Tousimis Samdri-795 Critical Point Dryer (Tousimis Research Corporation, Rockland MD) using liquid $CO_2$ and a 10 min purge time. Dried samples were coated with iridium for 30 seconds with an Emitech K575X Sputter Coater. Electron microscopy samples were imaged with a Zeiss Supra 55VP Field Emission Scanning Electron Microscopy (FE-SEM) (Carl Zeiss, Oberkochen, Germany) at 1keV.

Structural Predictions

Iterative Threading ASSEmbly Refinement (I-TASSER) was used to predict 3D structural models of DVU1012 and DVU1545 proteins (Zhang 2008, Roy et al. 2010, Yang et al. 2015). Due to I-TASSER's 1500 amino acid limit, a prediction was performed on the first 1500 amino acids of each protein, and then a separate prediction was performed on the second portion of the protein.

Structure Analysis

The predicted structure models were downloaded from I-TASSER results and images were generated in Pymol (The PyMOL Molecular Graphics System, Version

2.2.0 Schrödinger, LLC). Structures were also viewed in UCSF Chimera (Regents of the University of California, Version 1.13.1). Dimer and trimer models were constructed using the Matchmaker tool in UCSF Chimera to align the predicted monomer model from I-TASSER with monomers from the nearest homolog crystal structure used to guide the alignment.

Single Particle Analysis of DVU1012

DVU1012 was isolated from DvH (ATCC 29579) cell membranes as previously described (Walian et al., 2012) and included a final molecular sieve step (Superdex 200, GE Healthcare). For electron microscopy studies, 4 µl of sample (concentrated to about 0.1 mg /ml in a buffer of 20 mM HEPES pH 7.2, 100 mM NaCl and 0.01% C12E9) was applied to a glow-discharged grid (Formvar-carbon, 200 mesh copper, Electron Microscopy Sciences). After five minutes the sample was partially blotted (from the side with filter paper) to leave about 1 µl and the grid was placed sample-side down on a 75 µl water drop situated on parafilm. After two minutes the grid was transferred to a fresh drop of water. The grid was removed from the final water drop after two minutes and again partially blotted to about 1 µl to which 3 µl of 2% uranyl acetate was added. After one minute the remaining liquid was completely blotted. Sample grids were examined in a JEOL JEM-1200x electron microscope operating at 80 kV. A 2k x 2k pixel CCD camera (UltraScan, Gatan) controlled by the Digital Micrograph software package was used to record images at a magnification of 60,000X at which DVU1012 protein could be observed as hollow cylinder-like particles. The EMAN2 program suite (Tang et al.,

2007) was used to prepare a low-resolution 3D model from images of the negatively stained molecules.

Thin-section imaging of biofilms

DvH biofilms were grown on glass slides under batch conditions in LS4D media (Clark et al., 2007) for the wild-type and DVU1545 knock-out (*Δdvu1545*) strains. Biofilm samples were collected and fixed in 2% glutaraldehyde in PBS at pH 7.2. Samples were further processed by post-fixing with 1% osmium tetroxide, step-wise acetone dehydration and Epon-Araldite resin embedment. Thin sections (90 nm) were cut from polymerized resin blocks, transferred to electron microscopy grids and post-stained with Reynolds lead citrate and 2% uranyl acetate. Grids were examined using a JEOL JEM-1200x electron microscope operating at 80 kV. Images were recorded at a magnification range of 10 – 40 kX using a 2k x 2k pixel CCD camera (UltraScan, Gatan) controlled by the DigitalMicrograph software package. The ImageJ software package (Schneider et al., 2012) was used in the analysis of the collected images.

Multiple Sequence Alignment

Sequences were obtained through BLAST searches with the DVU1012 VWF protein sequence against the Non-redundant protein sequences database on the National Center for Biotechnology Information website, and bootstrapping using the human VWF domain sequence as a search query. Amino acid sequences: HvWF - *H. sapiens* gi317373549, PATR – *P. troglodytes* gi974593, CAJA – *C. jacchus* gi296211156, BOTA - *B. taurus* gi328887902, MUMU - *M. musculus* gi115511022, GAGA - *G. gallus* gi363728239, RvWF - *R. norvegicus* gi109474242, DARE - *D. rerio* gi326670654,

ACJO – *A. johnsonii* SH046 gi262371395, AESA - *A. salmonicida subsp. salmonicida* A449 gi145298663, D/1 - *Desulfovibrio sp.* A2 gi347732370, PSBR - *P. brassicacearum subsp. brassicacearum* NFM421 gi330808169, PSFL - *P. fluorescens* F113 gi378949442, PSFL *P. fluorescens* Pf0-1 gi77457690, PSEN – *P. entomophila* L48 gi104782921, CHLI – *C. limicola* DSM 245 gi189347157, CYSP - *Cyanobium sp*. PCC 7001 gi254430946, D/1 - *Desulfovibrio sp.* A2 gi347731967, DVVWF - *D. vulgaris str.* Miyazaki F gi218886590, DV12 - *D. vulgaris* Hildenborough gi46579425, DV45 - *D. vulgaris* Hildenborough gi46579956, MEMO – *M. mobilis* JLW8 gi253996156, DEPS - *D. psychrophila* LSv54 gi51244368, MOPE - *Moritella sp.* PE36 gi149911640, SHSE - *S. sediminis* HAW-EB3 gi157375479, DeAC - *D. acetiphilus* DSM 12809 gi291288403, D6_1/1 - *Desulfovibrio sp*. 6_1_46AFAA gi345891085, STAL – *S. albus* J1074 gi291452634, CHRE – *C. reinhardtii* gi|159485740 were obtained from the genomic database. The sequences were trimmed and aligned with Mafft. The sequences were manually adjusted to remove large gaps, while small gaps were left and are indicated by dashes.

## Results

### Planktonic Growth

The four strains wild-type (*Δupp*), *Δdvu1012, Δdvu1545,* and *Δdvu1012/Δdvu1545* did not display any differences in planktonic growth under the tested condition with 25 mM lactate: 16.6 mM sulfate in LS4D medium (Figure 1). Growth rates were similar for wild-type, *Δdvu1012,* and *Δdvu1545* ($0.088^{-h}$, $0.086^{-h}$, and

$0.088^{-h}$ respectively). The growth rate for the *Δdvu1012/Δdvu1545* strain was slightly lower at $0.078^{-h}$. Final O.D. 600 values were similar as well (0.7 to 0.8). The two strains with the *dvu1012* gene deleted (*Δdvu1012, Δdvu1012/dvu1545*) had slightly lower final max O.D. 600 readings.

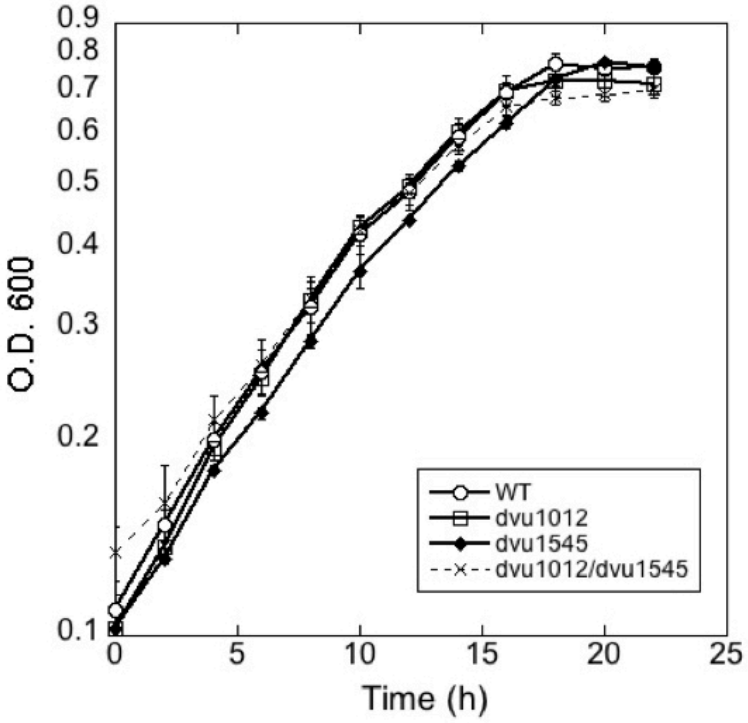


Figure 11. *Desulfovibrio vulgaris* Hildenborough strains were grown in batch culture at 30° C.

Biofilm Growth and Composition

Biofilms were grown continuously in CDC biofilm reactors with the same LS4D medium used for planktonic growth, with a stir rate of 50 rpm (Re=621) and dilution rate of 0.07/h. These stirring and dilution rates have been used routinely for the cultivation of *D. vulgaris* Hildenborough biofilm under sulfate-reducing conditions (Clark et al., 2012). Wild-type cultures increased biofilm biomass over 192 h and reached 46.1 $\mu g/cm^2$. The

*Δdvu1012* and *Δdvu1545* biofilms accumulated biomass at a similar rate as wild-type, and *Δdvu1012* achieved a similar biofilm protein level (47.3 μg/cm$^2$) (Figure 2). The mutant strain *Δdvu1545* produced slightly lower biofilm protein (38.5 μg/cm$^2$) (Figure 2). The double mutant strain *Δdvu1012/Δdvu1545* produced less biofilm biomass at the 96 h and 144 h time points (approximately 4x less protein) and had 20.6 μg/cm$^2$ biofilm protein at 192 h that was approximately 2x less than wild-type (Figure 2).

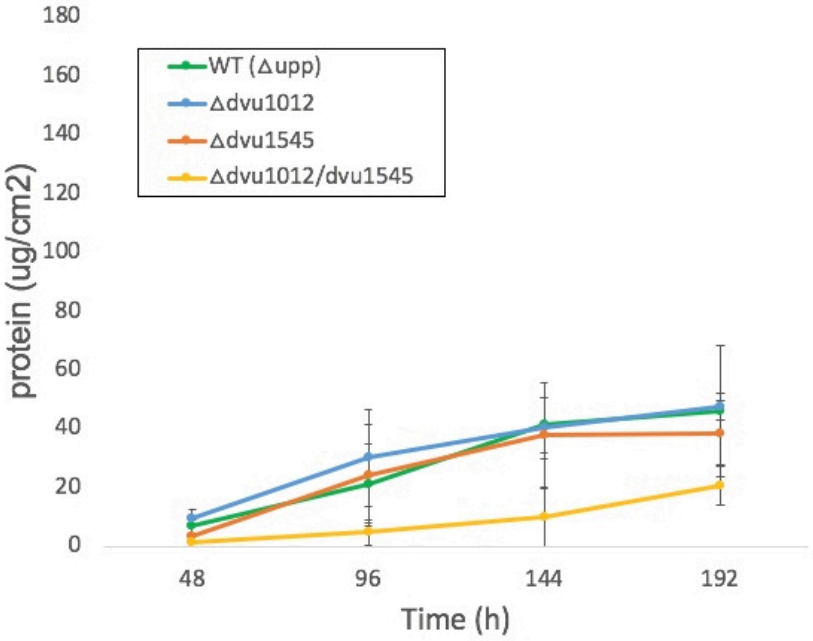


Figure 2. *D. vulgaris* Hildenborough wild-type and mutant biofilm protein levels at 50 rpm stir rate (Re= 621) for wild-type (WT), *Δdvu1012*, *Δdvu1545*, and *Δdvu1012/Δdvu1545* strains.

Hexose and protein measurements show a majority of the biofilm biomass to be comprised of protein and is similar for wild-type and the single mutant strains at later time points (Figure 3). However, the *Δdvu1545* strain had low initial biofilm that was mostly carbohydrate, and the *Δdvu1545* strain had similar biofilm biomass levels

(although slightly lower) compared to wild-type and *Δdvu1012* from 96 h to 192 h (Figure 3). At 192 h, the *Δdvu1012* strain had slightly higher carbohydrate levels compared to wild-type (8.3 versus 7.5 μg/cm$^2$) and the *Δdvu1545* strain had 1.3x lower carbohydrate levels (5.8 μg/cm$^2$) compared to wild-type (Figure 3). In addition to having lower protein levels, the *Δdvu1012/Δdvu1545* strain had lower carbohydrate levels at all time points and had 3.8x lower carbohydrate (1.96 μg/cm$^2$) at 192 h. Under the tested growth conditions, wild-type and single mutant strains had similar carbohydrate to protein ratios of 0.2 μg/μg, but the *Δdvu1012/Δdvu1545* strain had a carbohydrate to protein ratio of 0.09 μg/μg.

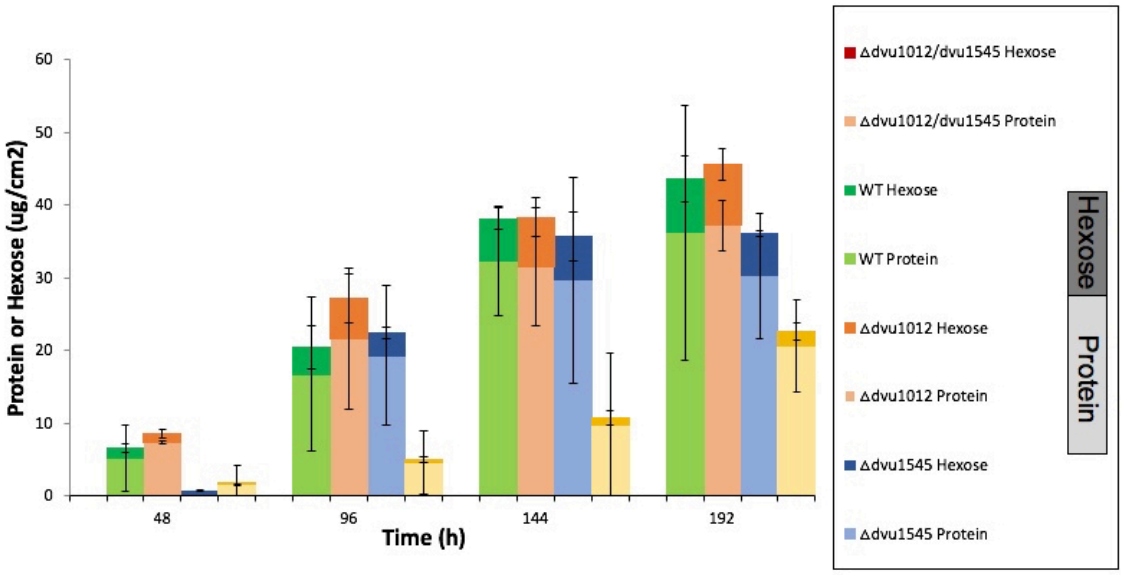


Figure 3. Hexose and protein levels for *D. vulgaris* Hildenborough wild-type and mutant biofilms.

Substrates and products

Lactate and acetate concentrations were measured throughout biofilm growth (Figure S1). Because the growth medium contained 25 mM lactate and 16.6 mM sulfate, and *D. vulgaris* Hildenborough utilizes lactate and sulfate in a 2:1 ratio, lactate levels were mostly undetectable by 48 hours. The wild-type biofilm had slightly higher lactate levels at the 48- and 96-hour time points than the other 3 strains, but by the 144-hour time point, lactate levels were undetectable and similar for all the tested strains (Figure S1). Acetate levels were similar for the wild-type, *Δdvu1012,* and *Δdvu1545* strains at 17 to 20 mM, but the *Δdvu1012/Δdvu1545* strain had higher acetate levels at 25 mM throughout the reactor run. Planktonic sulfide levels were similar for wild-type, *Δdvu1012,* and *Δdvu1545* strains at 3 to 5 μg/ml with higher initial levels for *Δdvu1012/Δdvu1545* (approximately 7.5 μg/ml; Figure S2). Biofilm sulfide levels ranged between 4 and 8 $\mu g/cm^2$ for the wild-type and *Δdvu1012* strains (Figure S2). The *Δdvu1545* strain initially had no detectable biofilm sulfide at 48 hours, but by 96 hours had reached very similar levels as wild-type and *Δdvu1012* strains (Figure S2b) and this result coincided with the initially much lower biofilm biomass levels (Figure 2 and 3). The *Δdvu1012/Δdvu1545* strain had very low, though detectable biofilm sulfide levels at 1 to 2 $\mu g/cm^2$ that also coincided with lower overall biofilm biomass (Figure 2 and 3).

Biofilm electron microscopy

The wild-type biofilm is made up of large aggregated structures of cells (30 to 60 μm) with spaces in between the clumps that penetrate to the substratum. The *Δdvu1012* biofilm had a more evenly dispersed arrangement of cells with much smaller clumps ($\leq$10

μm) and gaps that were more evenly distributed across the surface and much of the space between the small clumps occupied by single cells (Figure 4b). The *Δdvu1545* biofilm appeared similar to the *Δdvu1012* biofilm (smaller clumps) with less clumping of the biofilm compared to wild-type; however, the *Δdvu1545* biofilm could perhaps be considered as intermediate between wild-type and *Δdvu1012* in terms of aggregated cell structures (Figure 4c). There appeared to be a coating of dried salts along with attached single cells with sparsely interspersed aggregates of cells in the *Δdvu1012/Δdvu1545* biofilm (Figure 4d).

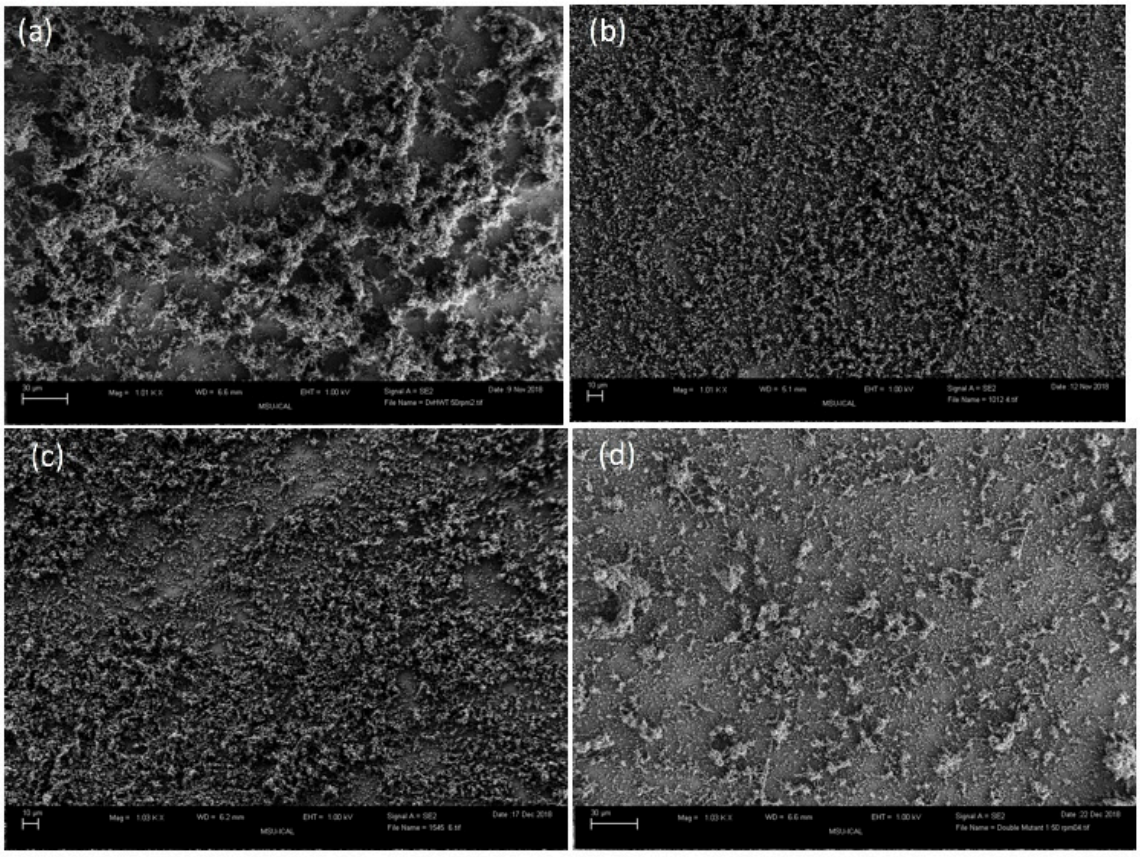


Figure 4. Field emission scanning electron microscopy images (1,000X) of DvH biofilm grown in grown in CDC biofilm reactors (192 h) on glass at 50 rpm stir rate for (a) wild-type, (b) *Δdvu1012*, (c) *Δdvu1545*, (d) and *Δdvu1012/Δdvu1545* strains.

Conserved domains

Based upon sequence comparisons with the Conserved Domains Database (CDD), DVU1012 contains multiple Type 1 secretion repeat domains (accession no. cl11927) throughout the predicted length, and these regions consist of glycine-rich sequences that can be tandem repeats that might provide a signal for type 1 secretion (Figure 5). Between residues 1318-1391 is a VCBS domain named from the multiple copies in long

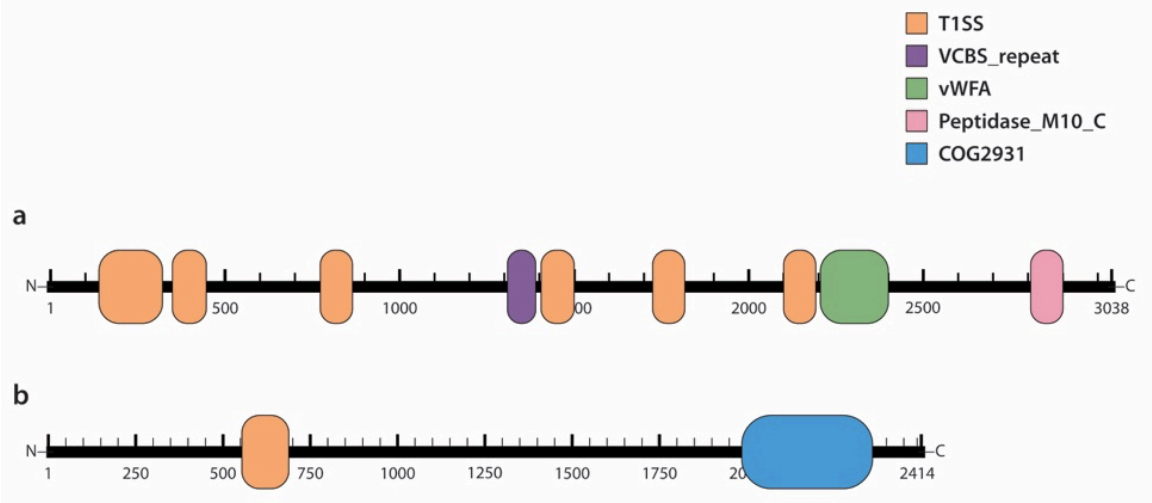


Figure 5. Conserved Domain Database (CDD) search results for DVU1012 (a) and DVU1545 (b) proteins.

proteins of *Vibrio*, *Colwellia*, *Bradyrhizobium*, and *Shewanella* species (reference), and residues 2243-2404 contain a Von Willebrand factor Type A (vWF) domain. There are multiple, presumptive interaction surfaces on this domain, and ligand binding is often mediated by a metal-ion dependent adhesion site (MIDAS) that also co-occurs in the vWF domain in DVU1012. Between residues 2851-2912 is a presumptive peptidase M10 serralysin C terminal domain that is related to mammalian matrix metallopeptidases. The domain has been shown previously to form a corkscrew and can be involved in

secretion of the protein through the cell wall and also contains a calcium-binding domain (pfam00353). The presumptive DVU1545 contained a Type 1 secretion site located at residues 563-692, and a COG2931 domain between residues 1984-2365 that is a $Ca^{2+}$-binding domain related to Rtx toxin proteins that can perform functions in biosynthesis, transport and catabolism (Figure 5). Although a von Willebrand domain was not readily identified in DVU1545, DVU1545 was annotated as a hemolysin-type Ca-binding repeat family protein as was DVU1012.

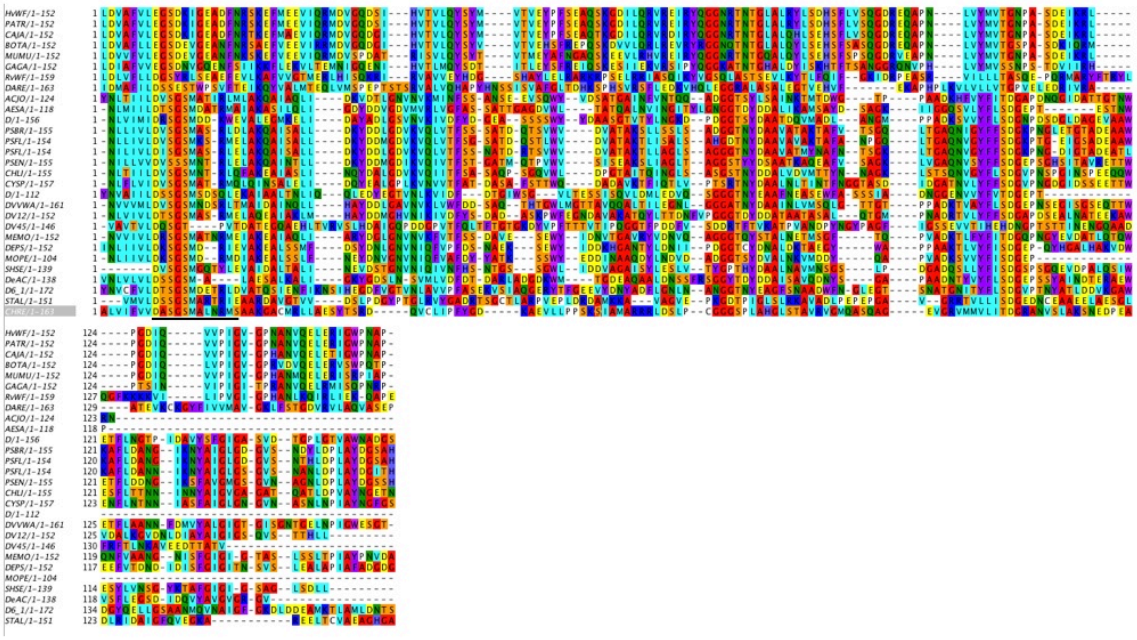

Figure 6. Multiple sequence alignment of Von Willebrand Type A (VWA) domain in DVU1012 (DV12) and DVU1545 (DV45) sequences among a collection of other VWA domains. Conservative substitution color coding was used to depict residues with similar properties as the same color to illustrate that the activity at that site may be preserved by the similar residue (i.e. function conservation). The characteristic MIDAS (metal ion dependent adhesion site) residues are underscored via the black line.

Multiple sequence alignment

Because vWF domains have a potential role in adhesion, a multiple alignment was constructed to more closely examine the domains (Figure 6). The multiple alignment has mammalian, other eukaryotic, and bacterial sequences. vWF domains have a characteristic Metal Ion Dependent Adhesion Site (MIDAS) region that contains the sequence D_S_S……T…….D (ref) and this sequence can be observed near the beginning of the alignment where the first aspartate is observed in the prokaryotic sequences (Figure 6). The DVU1012 sequence is most similar to the other bacterial sequences, and as expected, the DVU1545 sequence was quite different from the other sequences in the alignment. However, DV1545 does have the residues D_S_T……T…….D for a potential MIDAS domain. A maximum-likelihood tree grouped the vWF domain of DVU1012 with presumptive proteins from *Desulfovibrio* A2 and *D. vulgaris* Miyazaki (Figure S3).

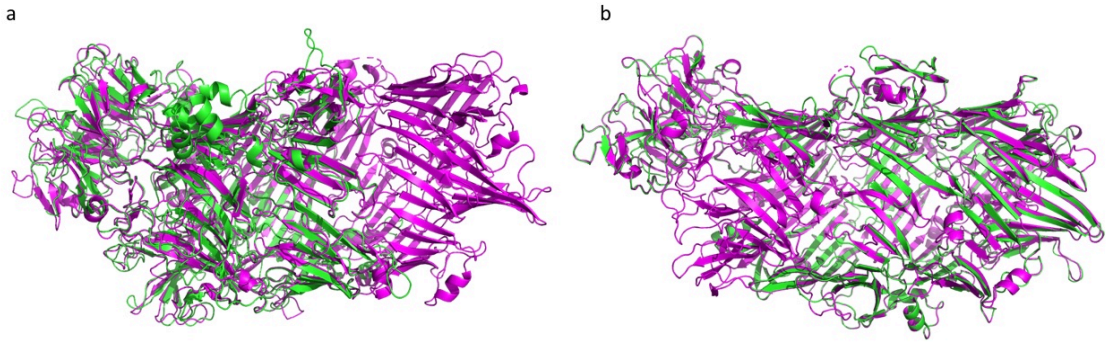


Figure 7. 3D alignment from I-TASSER of DVU1012 predicted structure and the solved crystal structure of TcdB2-TccC3 from *Photorhabdus luminescens.* The query structure is green and homolog structure is magenta. (a) DVU1012_a (amino acids 1-1500) aligned with TcdB2-TccC3. (b) DVU1012_b (amino acids 1501-3000) aligned with TcdB2-TccC3.

3D Structure Prediction

To obtain structure predictions for DVU1012 and DVU1545, the I-TASSER protein structure and function prediction server (Roy et al. 2010, Yang et al. 2015, Yang et al. 2015) was utilized. I-TASSER quantifies the quality of a predicted model by assigning a C-score (-5 to 2) to structural alignments with known proteins (higher value = better model quality). DVU1012 was run in three separate portions: residues 1-1500 (1012_a), residues 601-2100 (1012_middle), and residues 1501-3000 (1012_b) because I_TASSER can only model 1500 residues at a time. An additional comparison was done on the remaining 38 amino acids (1012_c) that resulted in no models of acceptable quality. 1012_a, 1012_middle, 1012_b, and 1012_c had C-scores of 0.05, 0.45, -0.1, and -3.17, respectively. Since I-TASSER uses a template-based modelling approach, LOMETS identifies the closest protein structure homolog in the Protein Data Bank (PDB) before threading each model. All three large portions of DVU1012 had high homology to two structures, the BC component of the ABC toxin complex in *Yersinia entomophaga* (Busby et al. 2013), and the TcdB2-TccC3 portion of the Tc toxin protein in *Photorhabdus luminescens* (Meusch et al. 2014) (PDB structures 4IGL and 4O9X, respectively). These two structures are nearly identical (Meusch et al. 2014). The alignments of 1012_a (TM-score = 0.87) and 1012_middle (TM-score = 0.99) together show complete coverage of the TcdB2-TccC3 protein that is 2,076 amino acids long. β-sheets comprise most of the secondary structure that wrap in an anticlockwise direction to form a large encapsulated chamber (Figure 7a). A β-propeller domain is present at the narrow end of the chamber offset from the axis of the other β-sheet wraps by approximately 45 degrees. The 1012_b

segment also aligned with 4IGL (TM-score = 0.95) more closely than with 4O9X (TM-score of 0.89).

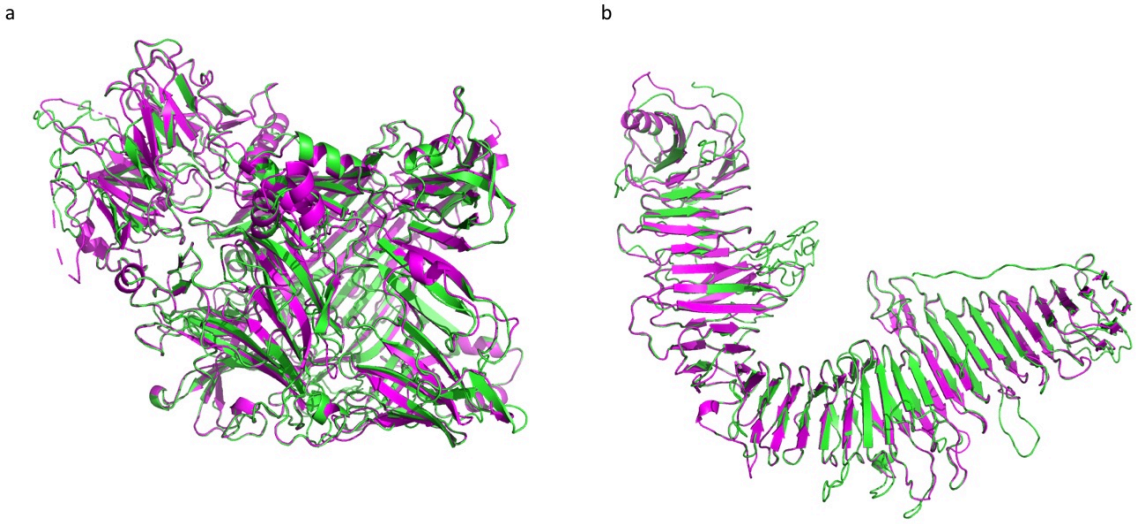


Figure 8. 3-Dimensial structure prediction of DVU1545 using I-TASSER. Query sequence is green and homolog structure is magenta. (a) DVU1545 residues 1-1500 aligned to PDB structure 4IGL. (b) DVU1545 residues 1501-2414 aligned to PDB structure 5N8P.

DVU1545 was submitted to I-TASSER in two separate portions 1545_a (amino acids 1-1500) and 1545_b (amino acids 1501-2414) with predicting model C-scores of -0.98 and -0.9, respectively. Similarly to DVU1012, DVU1545_a had the highest homology to the BC component of the ABC toxin complex in *Y. entomophaga* or Tc toxin of *P. luminescens* (TM-score = 0.91), while 1545_b was most similar to the S-layer protein RsaA from *Caulobacter cresecentus* (TM-score = 0.81) (Figure 8). These are PDB structures 4IGL and 5N8P, respectively. 1545_b is made of β-strands that form an L-shaped sheet structure with a tether sequence at one end. The S-layer protein (RsaA) in *C. crescentus* is anchored in the outer membrane by the tether sequence where it forms hexamers that coat the cell and form a protective layer (El-Kirat-Chatel et al., 2014).

Electron microscopy of DVU1012 and biofilm thin-sections

Transmission electron microscopy (TEM) and single particle analysis of images obtained from negatively-stained molecules yielded a hollow cylinder-like structural envelope for DVU1012. (Figure 9a and b). This envelope is consistent with the predominantly beta-sheet model produced through structure prediction with I-TASSER (Figure 7). The cylinder-like envelope has an outer diameter of ~11.5 nm and a length of ~15.5 nm. Thin-sections of *D. vulgaris* Hildenborough wild-type biofilms were also visualized with TEM, and cells were found making contacts with other cells as well as to matrix material via cylinder-like objects of similar size and shape to the model envelope determined for

DVU1012 (Figure 9c –f).

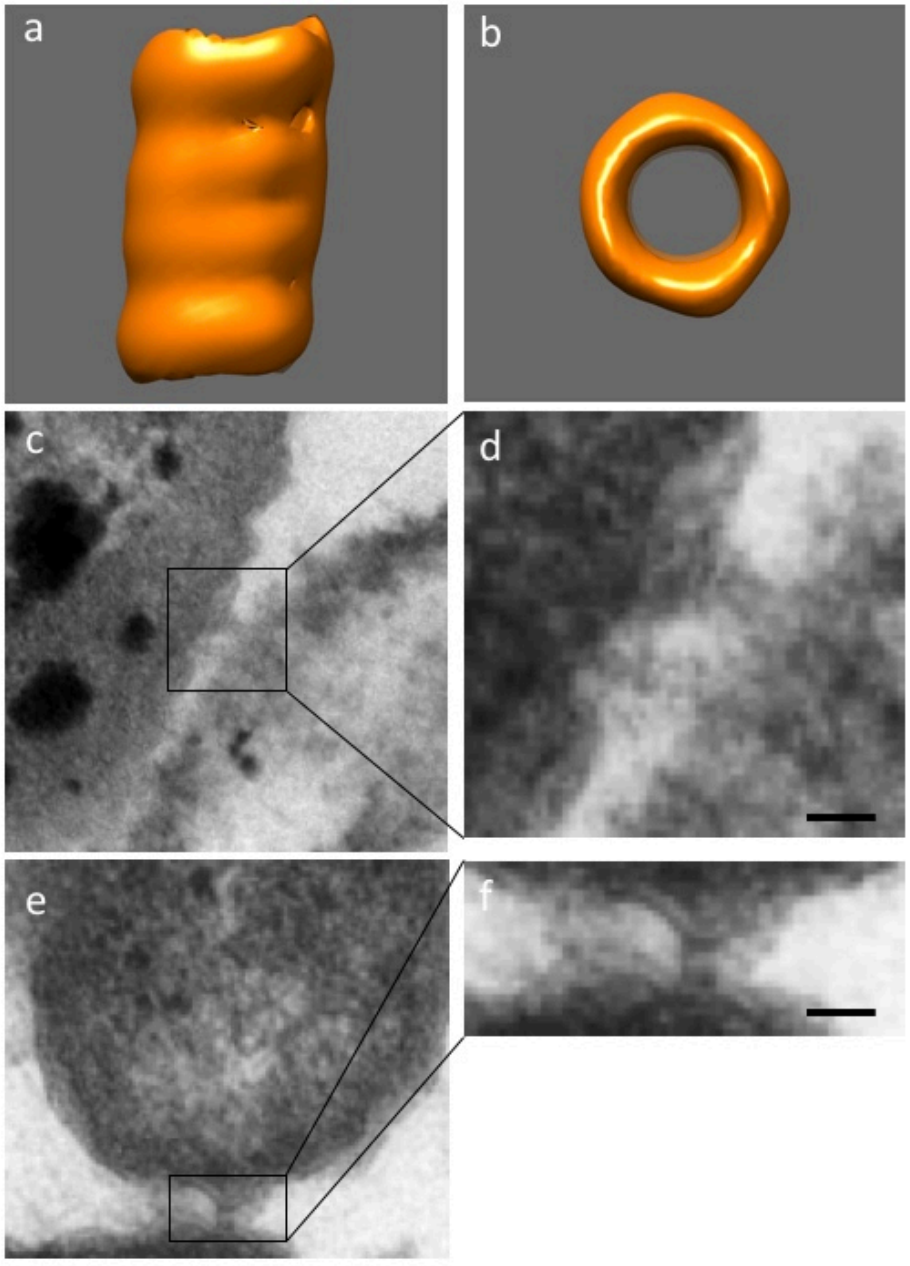


Figure 9. A DVU1012 working model. (a) Side view (outer diameter ~11.5nm, length ~15.4nm). (b) Top view. (a) Cell to cell interaction via two cylinder-like contacts in wild-type biofilm visualized via TEM. (d) Inset box showing magnification of interaction (scale bar 20 nm). (e) Cell to cell interaction via cylinder-like contact in wild-type biofilm visualized via TEM. (f) Inset showing magnification of interaction (scale bar 20 nm).

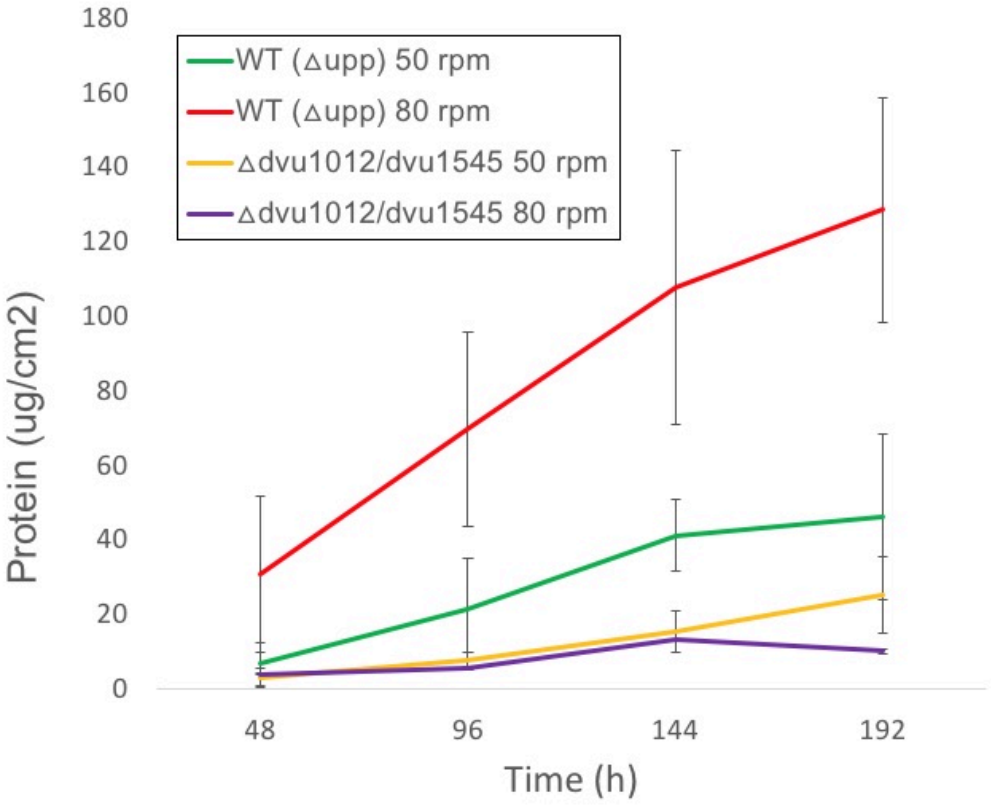


Figure 10. *Desulfovibrio vulgaris* Hildenborough biofilm grown in CDC biofilm reactor at low shear (Re= 621) and high shear stress (Re=993) for wild-type and *Δdvu1012/Δdvu1545* strain.

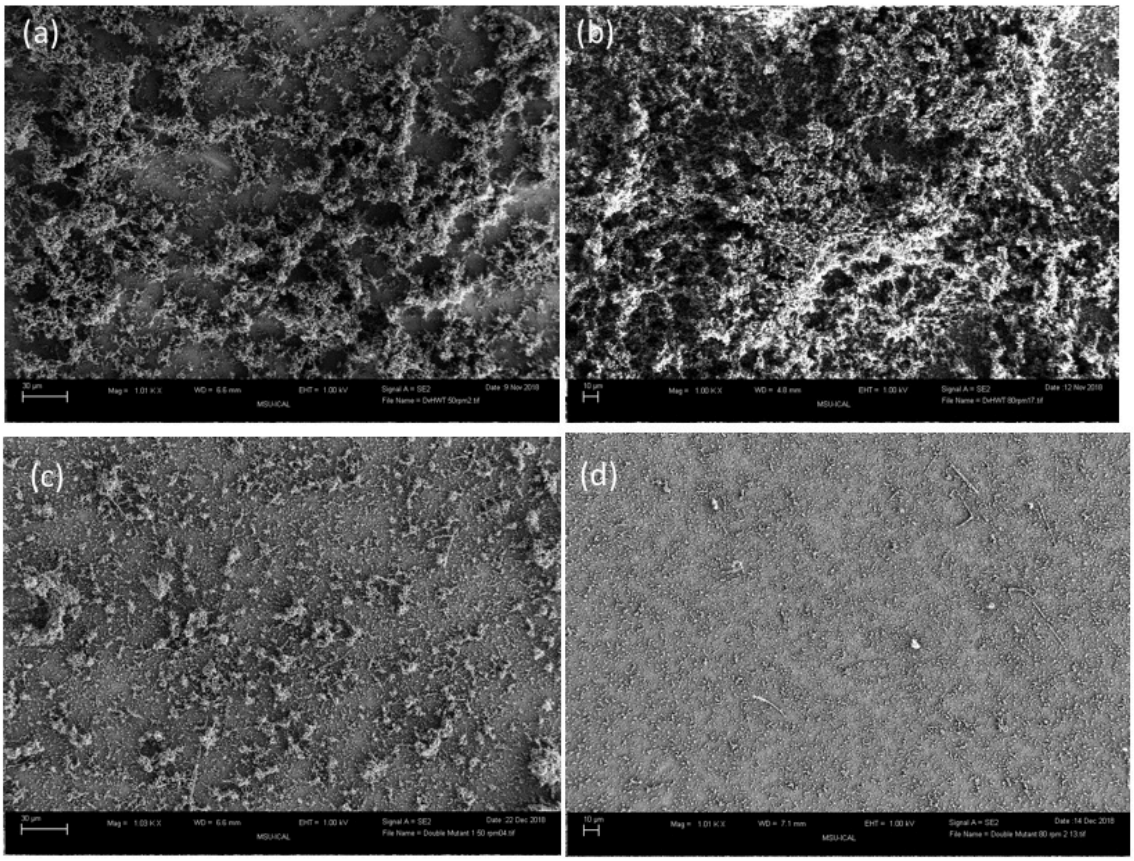


Figure 11. FE-SEM images (1,000X) of *Desulfovibrio vulgaris* Hildenborough biofilms grown in CDC biofilm reactors (192 h) on glass at 50 rpm stir rate (a and c) and 80 rpm stir rate (b and d) for wild-type (a and b) and *Δdvu1012/Δdvu1545* strain (c and d).

Biofilm formation and shear force

Given our initial findings indicating a significant role for DVU1012 and DVU1545 in biofilm architecture, as well as the structural similarity of the C-terminal region of DVU1545 with an S-layer protein of the stalked bacterium *C. crescentus*, we hypothesized that DVU1012 and/or DVU1545 may be important to the biofilm in when it experiences increased shear force. Wild-type biofilm growth at a lower stir rate (50 rpm; Re=621) had lower biofilm biomass (*i.e.*, protein levels) than wild-type biofilms cultivated at an increased stir rate of 80 rpm (increased shear force, Re=993) (Figure 10).

Wild-type biofilm at high shear had 2.8x more biofilm (μg protein/cm$^2$) compared to wild-type biofilm cultivated at low shear, and denser biofilm biomass could be observed for the biofilm cultivated at higher shear stress (Figure 11). Notably, the *Δdvu1012/Δdvu1545* double-mutant strain had 2.5x lower biofilm biomass (μg protein/cm$^2$) at the higher shear compared to the already low biofilm at low shear, and less biofilm was visualized via electron microscopy (Figure 10 and 11). Moreover, at high shear stress, the *Δdvu1012/Δdvu1545* biofilm was 12.7x less than wild-type biofilm (10.1 μg/cm$^2$ versus 128.5 (μg/cm$^2$) (Figure 10).

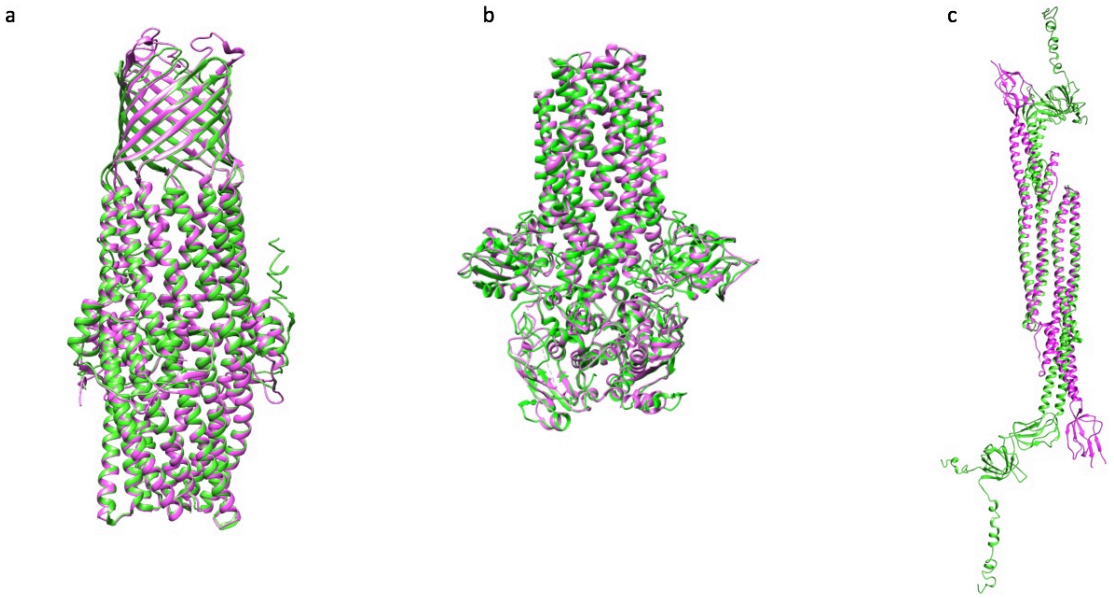


Figure 12. 3 dimensional alignments of structure predictions from I-TASSER aligned with nearest homolog. Query structure is green and nearest homolog is magenta. (a) DVU1013 trimer aligned to PDB structure 1TQQ. (b) DVU1017 dimer aligned to PDB structure 4RY2. (c) DVU1018 dimer aligned to PDB structure 5C21.

Structural predictions for DVU1012 operon products

The LapA protein in *Pseudomonas fluorescens* Pf0-1 is essential for biofilm formation, plays a role in cell adhesion, and contains vWF and T1SS export domains. Smith et al. (2018) showed LapA to be anchored in the outer membrane by LapE, a Type 1 secretion system outer membrane TolC-like pore protein. Recently, we showed that the presumptive proteins DVU1013 and DVU1017-DVU1020 have similar properties to the gene products of the Lap operon of *P. fluorescens* (De Leon et al., 2017). A pBLAST search with LapE against the DvH genome results in hits on genes DVU1013 and DVU3097, both of which are located to the outer membrane (Walian et al. 2012). Structure predictions were obtained for the presumptive gene products of the DVU1012 gene locus using I-TASSER allowing for comparison to the those of the Lap system. DVU1013 is predicted to be in an operon with DVU1012 while DVU1017-DVU1020 form a separate operon.

DVU1013 is a putative TolC-like outer membrane protein (Figure 12a) with the closest structure homolog identified as the TolC protein in *Escherichia coli* (Figure 12a). The C-score for the DVU1013 model was -0.29 and the alignment with the *E. coli* TolC crystal structure had a TM-score of 0.89. The assembled trimer forms an outer membrane β-barrel and a connecting α-helical barrel that projects across the periplasm and into the cytosol. The closest homolog to DVU1017 is an ABC transporter in *Clostridium thermocellum* (ATCC 27405) (Figure 12b). The C-score on the model is -0.49 and the TM-score on the alignment is 0.89. DVU1017 forms a dimer with an α-helical barrel forming the transmembrane domain, and the rest of the protein is predicted to be inside the

cell. A structure model was predicted for DVU3097 and it aligned closely to the same structure as DVU1013 with a C-score of 0.5 and a TM-score of 0.92 (data not shown).

LOMETS ( part of the I-TASSER tool suite) identified the nearest homolog to DVU1018 as the HlyD protein in *E. coli.* The C-score on the I-TASSER model is -2.50, suggesting it is lower quality than the other predicted models, and the TM-score of the alignment is 0.71. HlyD forms a dimer with no transmembrane domains. The lower TM-score can be visualized in the alignment (Figure 12c) with large differences in structure on the outer ends of the dimer. Both the predicted model and HlyD monomers have two α-helices that align towards the middle of the dimer. On the outer ends where the α-helices transition to β-sheets, the location and orientation of the β-sheets are quite different, and the DVU1018 predicted structure extends farther than HlyD, with additional α-helices. The structure was predicted for DVU1019 but the C-score was -2.51 similar to DVU1018 and the alignment had a poor TM-score of 0.55 (data not shown). The predicted model of DVU1020 aligned with the monomers comprising the octamer of an exocyst complex from *Saccharomyces cerevisiae* (ATCC 204508) with a C-score of -0.8 and TM-score of 0.92 (structural prediction and alignment not shown).

## Discussion

The conserved domain results for both DVU1012 and DVU1545 showed Type 1 secretion domains, and these result suggested the proteins are extracellular. These results corroborate previous results that observed both proteins as abundant polypeptides in the extracellular fraction of a sulfate-reducing DvH biofilm (Clark et al., 2012). DVU1012

(3,038 amino acids) was shown to have Type 1 secretion protein domains similar to the RtxA protein from *Vibrio cholerae* related to the export of toxin components, and ORFs immediately upstream of DVU1012 are annotated as *rtx*B and *rtx*D in the DvH genome (microbesonline.org). DVU1012 also has a predicted vWF (type A) domain and Ca-binding domain. When the entire polypeptide sequence was considered, an ortholog was identified (99.8% homology) in *Desulfovibrio vulgaris* DP4 that was annotated as an outer membrane adhesion protein (microbesonline.org). The first half of the polypeptide sequence had sequence homology with *Vibrio parahaemolyticus* strains (AQ3810 and RIMD 2210633), and the second half had sequence homology with *Denitrovibrio acetophilus* and *Pseudomonas entomophila* (microbesonline.org). DVU1545 is predicted to be a mono-cistronic protein (2,414 amino acids) that has a COG2931 conserved domain as well as a small metalloprotease domain. When the entire polypeptide sequence was considered, an ortholog was observed (53.5% identity) in *Desulfovibrio vulgaris* Miyazaki (microbesonline.org). Despite both being abundant in extracellular biofilm fractions with two similar domains, DVU1012 and DVU1545 have only 35.3% sequence identity over 52% of the polypeptide sequence. However, both polypeptides display sequence similarity to putative proteins involved in toxin secretion as well as protein adhesion.

The predicted structural models of DVU1012 and DVU1545 showed homology to the BC domains of ABC toxin delivery proteins. The BC domain in these systems forms a “cocoon” that encapsulates what is thought to be the unfolded toxin protein (Busby et al. 2013). The alignment of the predicted structural DVU1012 model and TcdB2-TccC3

showed a high degree of similarity, and the TEM-based DVU1012 structural envelope was similar to the I-TASSER predicted structure comprised largely of β-sheets arranged to form a barrel-like structure. The TEM-based structure of the captured confirmation is open on both ends suggestive of an open pore and not a toxin cage, and membrane association could be visualized when purified DVU1012 was incubated with bovine RBC membranes (unpublished results, Walian). A similar virulence protein, GtxA in *Gallibacterium anatis*, is a T1SS toxin with broad hemolysin activity that might also be involved in the disruption of linkages of integrins to the host actin cytoskeleton (Persson and Bojesen, 2015). The DVU1012 structure predictions also showed strong similarity to the B and C components of a *Photorhabdus luminescens* toxin that has insecticidal activity, and *P. luminescens* colonizes the gut of infective entomophathogenic nematodes where the toxins force actin polymerization/clustering (Lang et al., 2010). TEM images of biofilm thin-sections showed cells, and cells and EPS, making contacts through cylinder-like structures similar in size and shape to the DVU1012 structure. These results in combination with a predicted role in adhesion/cell interactions suggested DVU1012 likely plays a role binding cells together in the *Desulfovibrio* biofilm.

DVU1012 (residue 2,243 – 2,404) had sequence homology to von Willebrand factor type A domain (vWF) as well as structural similarity to the vWF domain in the BC component of the ABC toxin of *Y. entomophaga*. The putative domain had high sequence identity with vWFs from eukaryotes including humans, and vWF domains have more recently been identified in bacteria (Figure S3). vWF domains are typically identified in proteins that are involved in adhesion via protein-protein interactions. In

humans, vWFs can be part of multimeric glycoproteins that are crucial to the cessation of bleeding after tissue damage (hemostasis) (Ruggeri and Ware, 1993). During clotting, vWFs mediate the attachment of platelets to exposed tissue leading to platelet thrombi and thereby hemodynamic conditions with high shear stress (Ruggeri and Ware, 1993). von Willebrand disease (*i.e*., hemophilia) is the most common hereditable blood-clotting disorder in humans in which blood is unable to clot properly (Swystun and James, 2017).

Similar to DVU1012, the first 1500 amino acid residues of DVU1545 had the highest homology to toxin complexes of *P. luminescens* or *Y. entomophaga*. The second half of DVU1545 (residues 1,501-2,414) had the strongest similarity with an S-layer protein (RsaA) from *Caulobacter crescentus.* The S-layer protein, RsaA, forms a hexameric S-layer lattice with $Ca^{2+}$ ions used to stabilize interfaces as the stalked cell experiences variable shear forces in freshwater environments (Bharat et al., 2017). S-layer proteins assemble to form planar sheets around Gram-negative and Gram-positive bacteria (and archaea) anchored to other surface molecules and play roles in mechanical stability as well as pathogenicity (Albers and Meyer, 2011; Fagan and Fairweather, 2014). The RsaA S-layer is thought to act as a tough yet flexible barrier around *C. crescentus* that can adopt different conformations, and a similar role might be played for *D. vulgaris* biofilms as DVU1545 could provide strong yet flexible structural integrity for the biofilm. Interestingly, trypsin was used to aid in purification of RsaA portions from *C. crescentus* (Bharat et al., 2017), and we have previously shown that *D. vulgaris* biofilms (both early and mature) were susceptible to trypsin treatment (Clark et al., 2007).

Previous studies have shown LapA in *Psuedomonas fluorescens* to be essential for biofilm formation, and LapA is a T1SS export protein with a vWF domain that also has a large, tandomly repeated 100 amino acid segment (El-Kirat-Chatel et al., 2014). Similar proteins to LapA with large repeat regions have been recently reported in *Bordetella bronchiseptica* and *Shewanella oneidensis* (Zhou et al., 2015; Ambrosis et al., 2016). The predicted structures for DVU1012 and DVU1545 did not have significant structural similarity to LapA or the LapA-like proteins, and response to shear force stimuli have not been reported for LapA.

The mutant strains were not affected in planktonic growth, and while the single mutants formed a similar amount of biofilm as wild type, the double mutant produced less biofilm at all stages of biofilm development over the tested 192 h. The *Δdvu1012* mutant was most similar to wild-type biofilms in terms of protein/carbohydrate levels as well as microscopic appearance. The *Δdvu1545* mutant lagged in initial biofilm formation in the first 48 h of growth and had less biofilm biomass (protein and carbohydrate) at the latest time point compared to wild-type. Based upon these results as well as the different sequences, predicted structures, and different appearance of the respective biofilms, DVU1012 and DVU1545 have different but complementary roles in biofilm formation and maintenance. It is unknown if DVU1012 and DVU1545 directly interact for synergistic function, and further work is needed to delineate the mechanistic roles of each.

In a flow environment, fluid viscosity can generate hydrodynamic (shear) force on attached cells (and biofilm) that is tangential to the surface and is the primary force

experienced by biofilms (Stewart, 2012; Persat et al., 2015). Typically, bacterial cell adhesion forces range from a few to hundreds of pN (picoNewtons) in flow environments, but prosthecated *C. crescentus* can withstand forces as high as 1 μN (Persat et al., 2015). Interestingly, *C. crescentus* has a curved cell and because attached bacterial cells orient in the direction of flow, shear stress generates torque on curved cells that causes rotation of the distant cell pole to the substratum (Persat et al., 2014). This not only drives both cell poles to the substratum, but also leads to the 'deposition' of daughter cells onto the substratum surface that contributes to biofilm formation. *Desulfovibrio* also has a curved cell morphology, and therefore, the curved cell morphology could aid in biofilm formation. Multiple examples exist for increased cell attachment to surfaces when shear stress in increased, including *Escherichia coli* and *Pseudomonas aeruginosa* via fimbriae or pili, respectively (Thomas et al., 2004; Lecuyer et al., 2011). In *Staphylococcus aureus*, vWF proteins were shown to be involved in initial attachment to intact endothelium (Pappelbaum et al., 2013), and more recently in streptococcal adhesion in blood flow (Jagau et al., 2019).

Increasing the stir rate to 80 rpm (and thus shear force), demonstrated the importance of DVU1012 and DVU1545 in responding to shear stress. The wild-type biofilm greatly increased biofilm in response to increased shear force, but *Δdvu1012/Δdvu1545* made even less biofilm compared to the lower shear force condition. These results indicated that DVU1012 and DVU1545 functioned directly or indirectly to respond to shear stress and could provide the mechano-sensitive mechanism to form and maintain biofilm. We previously showed that the respective single mutants

(*Δdvu1012* or *Δdvu1545*) made wild-type levels of biofilm under higher shear (De Leon et al., 2017), and the DvH genome does not contain paralogs based upon sequence homology. Given the sequence and structural similarity to the vWF domain of DVU1012 and the role in shear force driven cell interactions in humans, *Staphylococcus*, and *Streptococcus* as well as the sequence and structural similarity to RsaA of DVU1545, it is interesting to speculate that DVU1012 is a mechano-sensitive extracellular protein that senses shear force and DVU1545 is an extracellular "armor-like" S-layer protein that provides the flexible structural integrity for the biofilm. The results suggest that DVU1012 and DVU1545 are compensatory and/or there are other components (*e.g.*, proteins, carbohydrate) that DVU1012 or DVU1545 can interact to sense hydrodynamics and regulate biofilm formation; however, both DVU1012 and DVU1545 together are required for maximal response to hydrodynamic force and biofilm formation.

Because DVU1012 is most similar to TccB2-TccC3 in *Y. entomophaga*, and DVU1012 and DVU1013 are adjacent in the DvH genome, comparing DVU1013 to TcA in *Y. entomophaga* bears consideration. The structures are similar in forming membrane pore complexes, but TcA is formed by a pentamer, the transmembrane domains are formed by α-helices, and a considerable portion of the protein remains outside the cell. DVU1013 is predicted to be a trimer where the β-barrel forms the transmembrane domain, and most of the protein complex is located inside the cytosol. Based upon these comparisons, the structural details appear quite different. Both TccB-TccC3 and LapA bind to a transmembrane pore complex that anchors to the outer membrane, and these results suggest that DVU1012 and DVU1545 may do the same but no current data

demonstrates a direct interaction between these proteins and DVU1013. LapE, which anchors LapA in the outer membrane in *Pseudomonas*, has sequence similarity with DVU1013 and DVU3097, and these results further suggest DVU1013 could be an anchor protein. The LapE/LapA interaction depends on a retention module that is the N-terminus of LapA. The binding of these two proteins allows *Pseudomonas fluorescens* Pf0-1 cells to adhere and form a biofilm (Smith et al. 2018). Yet neither DVU1012 nor DVU1545 are predicted to have such a retention module, so the potential binding mechanism for this presumptive system is unknown. The β-propeller domain of TccB-TccC3 binds TcA in *Y. entomophaga* that opens upon binding and releases the toxin cargo into the pore complex (Meusch et al. 2014). DVU1012 may function as a cocoon for delivery of a toxin but based upon the presented results a more likely function is an adhesin between cells, bound to transmembrane proteins.

DVU1017 has been demonstrated to be essential for biofilm formation (De Leon et al. 2017) and its deletion creates a similar phenotype to the *Δdvu1012/Δdvu1545* strain, and these data suggest that DVU1017 is necessary for the transport of DVU1012 and DVU1545 outside the cell. These results also coincide with the type 1 secretion domains in DVU1012 and DVU1545 and that DVU1017 is annotated as a transmembrane ABC transporter. The *Pseudomonas* LapG had low sequence homology to DVU1019 in the predicted DvH operon (De Leon et al., 2017), and LapG is a periplasmic cysteine protease that cleaves the N-terminal domain of LapA releasing it from LapE and causing dispersal of biofilm cells. The low quality of the predicted DVU1019 structural model in

combination with the lack of related crystal structures makes drawing predictions from the model difficult.

The fact that DVU1012 and DVU1545 both contain type 1 secretion sites suggests that they are translocated outside the cell through a Type 1 Secretion System (T1SS). The *E.coli* T1SS mechanism is the most well studied system and it requires an ABC transporter, a membrane fusion protein (MFP), and an outer membrane protein (OMP) (Spitz et al. 2019). In *E.coli,* the ABC transporter (HlyB) crosses only the inner membrane where a complex is formed with the MFP (HlyD) (Kanonenberg et al. 2018). The OMP (TolC) crosses the outer membrane, and together form the pore complex that exports T1SS substrates (Kanonenberg et al. 2018). Looking for homologs to this system in DvH identifies DVU1017 as an ABC transporter required for secretion of DVU1012 and DVU1545, and DVU1018 as a potential MFP. One significant difference between *E.coli* and DvH is that the predicted structure of DVU1017 crosses both membranes, and this prediction raises the question of whether the TolC and MFP are necessary for Type 1 secretion in DvH. Further investigation of the mechanisms for secretion of DVU1012, DVU1545, and potentially interacting components is needed.

An additional question is the potential role of DVU1013 annotated as a TolC-like protein, predicted to be in an operon with DVU1012. Further similarities emerge between *E.coli* and DvH because HlyA (a pore forming toxin), displays sequence homologies to DVU1012 and DVU1545. Upstream of the C-terminal secretion signal, HlyA has nonapeptide repeats of GgxGxDxUx that bind extracellular $Ca^{2+}$ and initiate folding upon

secretion. DVU1012 has two of these consensus sequences and DVU1545 has one, all near the C-terminus.

Microorganisms typically occupy dynamic fluid environments and can be concentrated via fluid shear (Rusconi et al., 2014), and the feedback between hydrodynamic conditions and mechanical properties of microbial cells subsequently influences the formation and behavior of biofilms (Persat et al., 2015). The presented results demonstrated an essential role of DVU1012 and DVU1545 together for optimal response to hydrodynamic force and biofilm formation. The proteins are secreted via a T1SS similar to adhesin and toxin systems in Gram-negative bacteria and remain cell associated via possible interactions with the outer membrane. The vWF domain would provide a mechanism for responses to hydrodynamics, and the unique predicted structure of DVU1545 would provide flexible but strong mechanical strength. The ability of DvH to readily form biofilm impacts multiple large-scale processes including metal pipeline corrosion, concrete corrosion, contributions to global carbon and sulfur cycling in the subsurface microbiome, and colon cancer in humans. Further work is needed to delineate the potential interactions between DVU1012 and DVU1545 and other cellular components important to biofilm formation and maintenance in different environments with hydrodynamic forces.

## Acknowledgements

This material is funded by ENIGMA- Ecosystems and Networks Integrated with Genes and Molecular Assemblies (http://enigma. lbl.gov), a Scientific Focus Area Program at Lawrence Berkeley National Laboratory is based upon work supported by the U.S.

Department of Energy, Office of Science, Office of Biological & Environmental Research under contract number DE-AC02-05CH11231.

References

Yang, J. & Zhang, Y. I-TASSER server: new development for protein structure and function predictions. *Nucleic Acids Res.* **43**, W174–81 (2015).

Rusconi, R., Guasto, J. S. & Stocker, R. Bacterial transport suppressed by fluid shear. *Nat. Phys.* **10**, 212 (2014).

Payne, D. E. & Boles, B. R. Emerging interactions between matrix components during biofilm development. *Curr. Genet.* **62**, 137–141 (2016).

Schooling, S. R. & Beveridge, T. J. Membrane vesicles: an overlooked component of the matrices of biofilms. *J. Bacteriol.* **188**, 5945–5957 (2006).

Hooper, S. L. & Burstein, H. J. Minimization of extracellular space as a driving force in prokaryote association and the origin of eukaryotes. *Biol. Direct* **9**, 24 (2014).

Spitz, O. *et al.* Type I Secretion Systems-One Mechanism for All? *Microbiol Spectr* **7**, (2019).

Kanonenberg, K., Spitz, O., Erenburg, I. N., Beer, T. & Schmitt, L. Type I secretion system-it takes three and a substrate. *FEMS Microbiol. Lett.* **365**, (2018).

Thomas, S., Holland, I. B. & Schmitt, L. The Type 1 secretion pathway - the hemolysin system and beyond. *Biochim. Biophys. Acta* **1843**, 1629–1641 (2014).

Holland, I. B., Schmitt, L. & Young, J. Type 1 protein secretion in bacteria, the ABC-transporter dependent pathway (review). *Mol. Membr. Biol.* **22**, 29–39 (2005).

Higgins, M. K. *et al.* Structure of the ligand-blocked periplasmic entrance of the bacterial multidrug efflux protein TolC. *J. Mol. Biol.* **342**, 697–702 (2004).

Pettersen, E. F. *et al.* UCSF Chimera--a visualization system for exploratory research and analysis. *J. Comput. Chem.* **25**, 1605–1612 (2004).

Kim, J.-S. *et al.* Crystal Structure of a Soluble Fragment of the Membrane Fusion Protein HlyD in a Type I Secretion System of Gram-Negative Bacteria. *Structure* **24**, 477–485 (2016).

Walian, P. J. *et al.* High-throughput isolation and characterization of untagged membrane protein complexes: outer membrane complexes of Desulfovibrio vulgaris. *J. Proteome Res.* **11**, 5720–5735 (2012).

Newell, P. D., Monds, R. D. & O'Toole, G. A. LapD is a bis-(3',5')-cyclic dimeric GMP-

binding protein that regulates surface attachment by Pseudomonas fluorescens Pf0-1. *Proc. Natl. Acad. Sci. U. S. A.* **106**, 3461–3466 (2009).

Ivanov, I. E. *et al.* Atomic force and super-resolution microscopy support a role for LapA as a cell-surface biofilm adhesin of Pseudomonas fluorescens. *Res. Microbiol.* **163**, 685–691 (2012).

Persat, A. *et al.* The mechanical world of bacteria. *Cell* **161**, 988–997 (2015).

Bill Costerton, Gill Geesey, K.J. Cheng. How Bacteria Stick. (1978). doi:10.1038/scientificamerican0178-86

Flemming, H.-C. EPS-Then and Now. *Microorganisms* **4**, (2016).

Guo, S., Vance, T. D. R., Stevens, C. A., Voets, I. & Davies, P. L. RTX Adhesins are Key Bacterial Surface Megaproteins in the Formation of Biofilms. *Trends Microbiol.* **27**, 453–467 (2019).

Smith, T. J., Font, M. E., Kelly, C. M., Sondermann, H. & O'Toole, G. A. An N-Terminal Retention Module Anchors the Giant Adhesin LapA of Pseudomonas fluorescens at the Cell Surface: a Novel Subfamily of Type I Secretion Systems. *J. Bacteriol.* **200**, (2018).

Ost, G. S., Ng'ang'a, P. N., Lang, A. E. & Aktories, K. Photorhabdus luminescens Tc toxin is inhibited by the protease inhibitor MG132 and activated by protease cleavage resulting in increased binding to target cells. *Cell. Microbiol.* **21**, e12978 (2019).

Jackson, V. A., Busby, J. N., Janssen, B. J. C., Lott, J. S. & Seiradake, E. Teneurin Structures Are Composed of Ancient Bacterial Protein Domains. *Front. Neurosci.* **13**, 183 (2019).

Gatsogiannis, C. *et al.* Membrane insertion of a Tc toxin in near-atomic detail. *Nat. Struct. Mol. Biol.* **23**, 884–890 (2016).

Li, J. *et al.* Structural Basis for Teneurin Function in Circuit-Wiring: A Toxin Motif at the Synapse. *Cell* **173**, 735–748.e15 (2018).

Jackson, V. A. *et al.* Structures of Teneurin adhesion receptors reveal an ancient fold for cell-cell interaction. *Nat. Commun.* **9**, 1079 (2018).

Hobley, L., Harkins, C., MacPhee, C. E. & Stanley-Wall, N. R. Giving structure to the biofilm matrix: an overview of individual strategies and emerging common themes. *FEMS Microbiol. Rev.* **39**, 649–669 (2015).

Flemming, H.-C., Neu, T. R. & Wozniak, D. J. The EPS matrix: the 'house of biofilm cells'. *J. Bacteriol.* **189**, 7945–7947 (2007).

Karatan, E. & Watnick, P. Signals, regulatory networks, and materials that build and break bacterial biofilms. *Microbiol. Mol. Biol. Rev.* **73**, 310–347 (2009).

Flemming, H.-C. & Wingender, J. The biofilm matrix. *Nat. Rev. Microbiol.* **8**, 623–633 (2010).

Yang, J. *et al.* The I-TASSER Suite: protein structure and function prediction. *Nat. Methods* **12**, 7–8 (2015).

Roy, A., Kucukural, A. & Zhang, Y. I-TASSER: a unified platform for automated protein structure and function prediction. *Nat. Protoc.* **5**, 725 (2010).

Zhang, Y. I-TASSER server for protein 3D structure prediction. *BMC Bioinformatics* **9**, 40 (2008).

Clark, M. E., Edelmann, R. E., Duley, M. L., Wall, J. D. & Fields, M. W. Biofilm formation in Desulfovibrio vulgaris Hildenborough is dependent upon protein filaments. *Environ. Microbiol.* **9**, 2844–2854 (2007).

De León, K. B. *et al.* Unintended Laboratory-Driven Evolution Reveals Genetic Requirements for Biofilm Formation by Desulfovibrio vulgaris Hildenborough. *MBio* **8**, (2017).

Busby, J. N., Panjikar, S., Landsberg, M. J., Hurst, M. R. H. & Lott, J. S. The BC component of ABC toxins is an RHS-repeat-containing protein encapsulation device. *Nature* **501**, 547–550 (2013).

Clark, M. E. *et al.* Transcriptomic and proteomic analyses of Desulfovibrio vulgaris biofilms: Carbon and energy flow contribute to the distinct biofilm growth state. *BMC Genomics* **13**, (2012).

Clark, M. E. *et al.* Temporal Transcriptomic Analysis as Desulfovibrio vulgaris Hildenborough Transitions into Stationary Phase during Electron Donor Depletion. *Appl. Environ. Microbiol.* **72**, 5578–5588 (2006).

Heidelberg, J. F. *et al.* The genome sequence of the anaerobic, sulfate-reducing bacterium Desulfovibrio vulgaris Hildenborough. *Nat. Biotechnol.* **22**, 554–559 (2004).

Supplementary Information

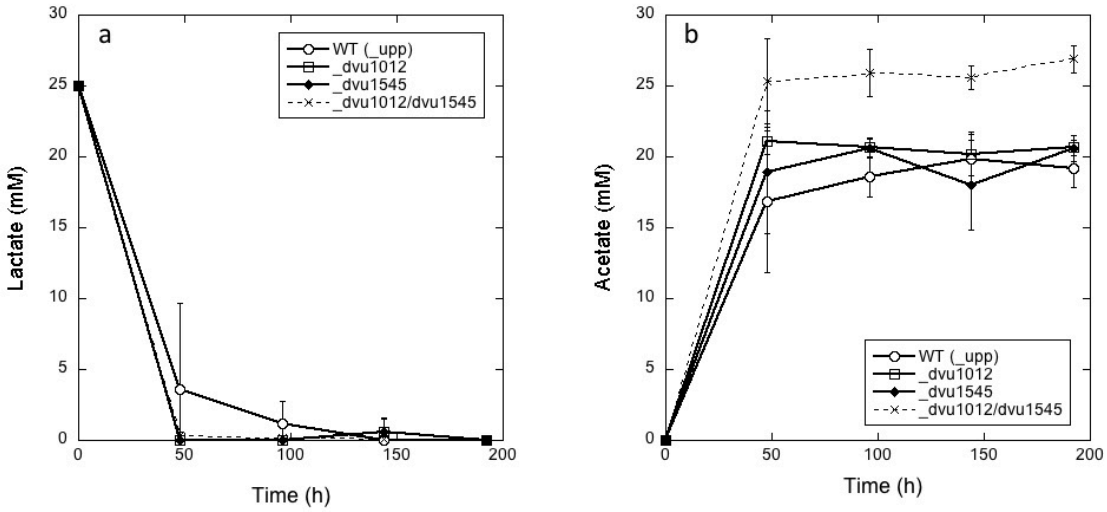


Figure S1. (a) Lactate and (b) acetate levels over time during reactor growth for the different *Desulfovibrio vulgaris* Hildenborough strains grown in CDC biofilm reactors on glass.

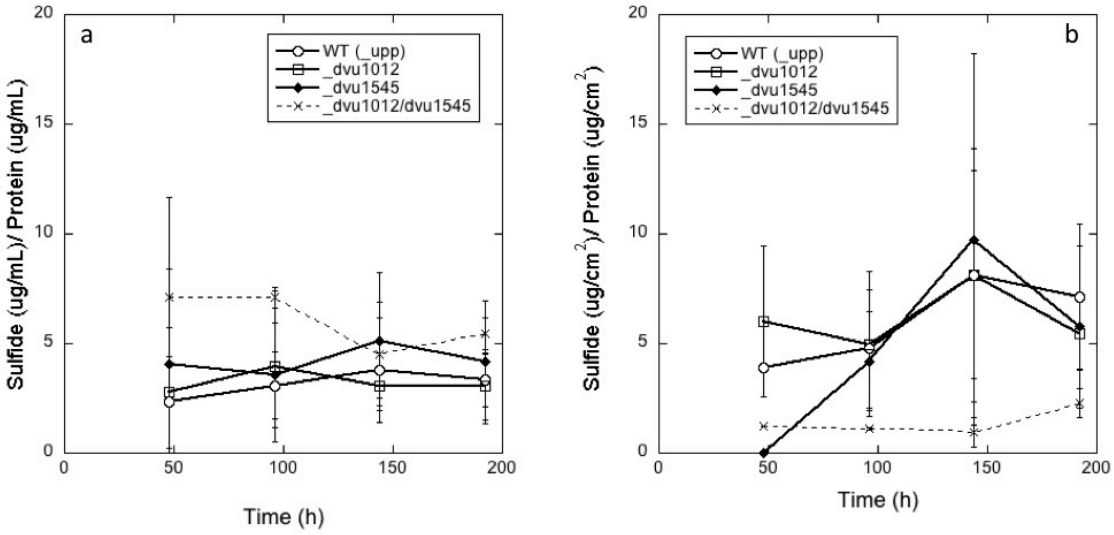


Figure S2. (a) Planktonic sulfide numbers normalized to planktonic protein levels and (b) biofilm sulfide numbers normalized to surface area and biofilm protein levels for the different *Desulfovibrio vulgaris* Hildenborough strains grown in CDC biofilm reactors on glass.

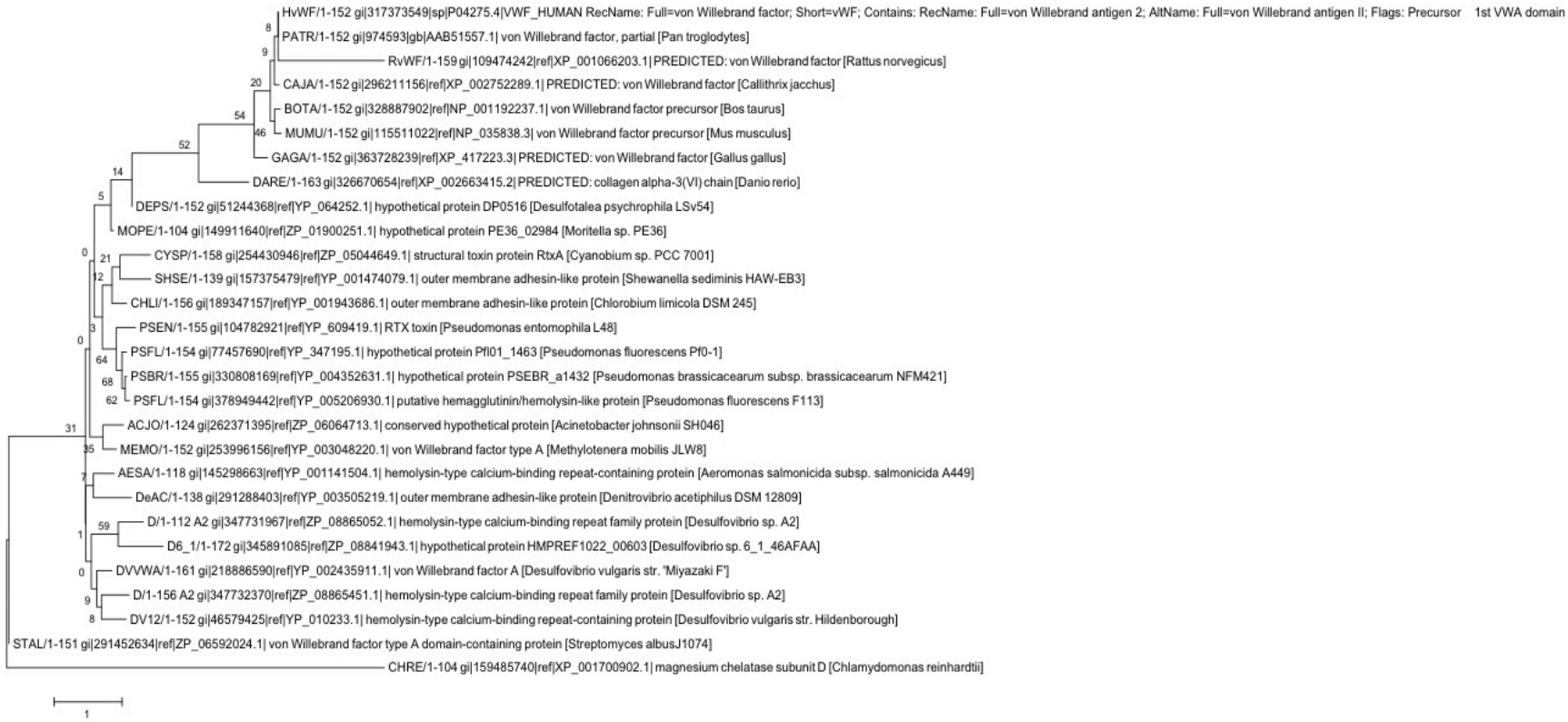
HvWF/1-152 gi|317373549|sp|P04275.4|VWF_HUMAN RecName: Full=von Willebrand factor; Short=vWF; Contains: RecName: Full=von Willebrand antigen 2; AltName: Full=von Willebrand antigen II; Flags: Precursor 1st VWA domain
PATR/1-152 gi|974593|gb|AAB51557.1| von Willebrand factor, partial [Pan troglodytes]
RvWF/1-159 gi|109474242|ref|XP_001066203.1| PREDICTED: von Willebrand factor [Rattus norvegicus]
CAJA/1-152 gi|296211156|ref|XP_002752289.1| PREDICTED: von Willebrand factor [Callithrix jacchus]
BOTA/1-152 gi|328887902|ref|NP_001192237.1| von Willebrand factor precursor [Bos taurus]
MUMU/1-152 gi|115511022|ref|NP_035838.3| von Willebrand factor precursor [Mus musculus]
GAGA/1-152 gi|363728239|ref|XP_417223.3| PREDICTED: von Willebrand factor [Gallus gallus]
DARE/1-163 gi|326670654|ref|XP_002663415.2| PREDICTED: collagen alpha-3(VI) chain [Danio rerio]
DEPS/1-152 gi|51244368|ref|YP_064252.1| hypothetical protein DP0516 [Desulfotalea psychrophila LSv54]
MOPE/1-104 gi|149911640|ref|ZP_01900251.1| hypothetical protein PE36_02984 [Moritella sp. PE36]
CYSP/1-158 gi|254430946|ref|ZP_05044649.1| structural toxin protein RtxA [Cyanobium sp. PCC 7001]
SHSE/1-139 gi|157375479|ref|YP_001474079.1| outer membrane adhesin-like protein [Shewanella sediminis HAW-EB3]
CHLI/1-156 gi|189347157|ref|YP_001943686.1| outer membrane adhesin-like protein [Chlorobium limicola DSM 245]
PSEN/1-155 gi|104782921|ref|YP_609419.1| RTX toxin [Pseudomonas entomophila L48]
PSFL/1-154 gi|77457690|ref|YP_347195.1| hypothetical protein Pfl01_1463 [Pseudomonas fluorescens Pf0-1]
PSBR/1-155 gi|330808169|ref|YP_004352631.1| hypothetical protein PSEBR_a1432 [Pseudomonas brassicacearum subsp. brassicacearum NFM421]
PSFL/1-154 gi|378949442|ref|YP_005206930.1| putative hemagglutinin/hemolysin-like protein [Pseudomonas fluorescens F113]
ACJO/1-124 gi|262371395|ref|ZP_06064713.1| conserved hypothetical protein [Acinetobacter johnsonii SH046]
MEMO/1-152 gi|253996156|ref|YP_003048220.1| von Willebrand factor type A [Methylotenera mobilis JLW8]
AESA/1-118 gi|145298663|ref|YP_001141504.1| hemolysin-type calcium-binding repeat-containing protein [Aeromonas salmonicida subsp. salmonicida A449]
DeAC/1-138 gi|291288403|ref|YP_003505219.1| outer membrane adhesin-like protein [Denitrovibrio acetiphilus DSM 12809]
D/1-112 A2 gi|347731967|ref|ZP_08865052.1| hemolysin-type calcium-binding repeat family protein [Desulfovibrio sp. A2]
D6_1/1-172 gi|345891085|ref|ZP_08841943.1| hypothetical protein HMPREF1022_00603 [Desulfovibrio sp. 6_1_46AFAA]
DVVWA/1-161 gi|218886590|ref|YP_002435911.1| von Willebrand factor A [Desulfovibrio vulgaris str. 'Miyazaki F']
D/1-156 A2 gi|347732370|ref|ZP_08865451.1| hemolysin-type calcium-binding repeat family protein [Desulfovibrio sp. A2]
DV12/1-152 gi|46579425|ref|YP_010233.1| hemolysin-type calcium-binding repeat-containing protein [Desulfovibrio vulgaris str. Hildenborough]
STAL/1-151 gi|291452634|ref|ZP_06592024.1| von Willebrand factor type A domain-containing protein [Streptomyces albusJ1074]
CHRE/1-104 gi|159485740|ref|XP_001700902.1| magnesium chelatase subunit D [Chlamydomonas reinhardtii]
1

Figure S3. Maximum likelihood tree built from Maft alignment of eukaryotic and bacterial protein sequences with predicted VWA domains.

# CHAPTER FOUR

# CHARACTERIZATION OF EXTRACELLULAR BIOFILM MUTANTS CULTIVATED ON 1018 CARBON STEEL IN *DESULFOVIBRIO VULGARIS* HILDENBOROUGH

## Contributions of Authors and Co-Authors

Manuscript in Chapter 4

Author: Gregory P. Krantz

Contributions: Developed experimental design, performed experiments, analyzed data, wrote and revised the manuscript.

Author: Marty Boyl-Davis

Contributions: Performed experiments, analyzed data.

Author: Kara B. De Leon

Contributions: Performed experiments, analyzed data, wrote and revised the manuscript.

Author: Judy D. Wall

Contributions: Analyzed data, wrote and revised the manuscript.

Author: Matthew W. Fields

Contributions: Developed experimental design, analyzed data, wrote and revised the manuscript.

Manuscript Information

Gregory P. Krantz, Marty Boyl-Davis, Kara De Leon, Judy D. Wall, & Matthew W. Fields

Status of Manuscript:
__X_ Prepared for submission to a peer-reviewed journal
____ Officially submitted to a peer-reviewed journal
____ Accepted by a peer-reviewed journal

## Abstract

Previous work has demonstrated the important role of large, previously undescribed proteins in biofilm formation and maintenance in the sulfate-reducing bacterium, *Desulfovibrio vulgaris* Hildenborough. Three strains (WT, Δ*dvu1012,* and Δ*dvu1545)* were grown under steady-state conditions in CDC biofilm reactors on 1018 carbon steel under sulfate-reducing conditions to elucidate potential impacts on metal corrosion. Protein measurements indicated the wild-type strain had less initial biofilm biomass than the two deletion strains but similar protein levels for all three strains were observed after longer biofilm growth The Δ*dvu1012* strain had slightly increased carbohydrate levels throughout growth compared to wild-type and the Δ*dvu1545* strains. Initial average planktonic sulfide measurements were highest in the WT strain, though they became similar to the other strains after 192 hours. Biofilm sulfide levels were, on average, highest in the *Δdvu1012* strain and lowest in the *Δdvu1545* strain. An increased initial corrosion rate was observed on the coupons exposed to the *Δdvu1012* culture, though this difference decreased in later time points.

## Introduction

Microbiologically-influenced corrosion of metals occurs under a variety of conditions in marine, freshwater, and terrestrial environments, and sulfate-reducing bacteria are a predominant population that contributes to the direct and indirect biodegradation and biodeterioration of the material (Beech and Gaylarde, 1999). Biofilms are an important contributor to the overall process, and the biofilm EPS (exo-polymeric substance) contributes to interactions with the surface that likely mediate adhesion, ecology, and biochemical activity. For example, *Pseudoaltermonas lipolytica* biofilms on low-alloy steel mainly consisted of proteins and carboxylic acid, and corrosion was increased compared to a *Bacillus* biofilm that consisted of mainly polysaccharides (Guo et al., 2017). However, little is known about the individual EPS components of metal-corroding biofilms, particularly protein, nor the direct and/or indirect roles played in biofilm formation, maintenance, and activity.

MIC can involve a variety of different microorganisms that include sulfate-reducing bacteria (SRB). *Desulfovibrio vulgaris* Hildenborough (DvH) has been implicated in MIC of carbon steel infrastructure and is used as a model organism for extensive anaerobic corrosion studies (Heidelberg et al. 2004). Previous work with *D. vulgaris* Hildenborough showed that biofilms on glass were dependent upon protein filaments (Clark et al., 2007), and subsequent proteomic analyses identified two large, extracellular proteins (DVU1012 and DVU1545) as the most abundant polypeptides extracted from biofilm fractions cultivated on glass (Clark et al., 2012). Recent work by Krantz et al. (Chapter 3) demonstrated the essential role of the proteins (DVU1012 and

DVU1545) to biofilm formation and maintenance in *Desulfovibrio vulgaris* Hildenborough (DvH) when grown on a glass surface but the impacts on metal biofilms is not known.

Laboratory cultures of microorganisms are commonly cultivated under conditions of balanced stoichiometry in terms of carbon and energy sources (or at least conditions of excess). Our recent work demonstrated that when *D. alaskensis* G20 biofilm was grown under electron-donor limiting conditions, corrosion of 1018 carbon steel was increased approximately 3-fold (Chapter 2). Therefore, the described study explores the role of DVU1012 and DVU1545 in forming biofilm on 1018 carbon steel under electron-donor limiting conditions and the potential impact on metal corrosion.

## Materials and Methods

### Microorganism and cultivation

*Desulfovibrio vulgaris* Hildenborough (DvH) was grown in a defined lactate/sulfate (LS4D) medium prepared anoxically as previously described under a variety of conditions (Clark et al., 2007; Klonowoska et al., 2008). Modifications to the original recipe included adjusting the lactate and sulfate concentrations to 25 mM lactate and 16.6 mM sulfate (*i.e.*, electron-donor limiting conditions). As previously described, the medium was not prepared with reducing agent (Clark et al., 2006), and the use of resazurin in the culture medium served as a general indicator of oxidative-reduction potential (ORP). A small amount of sodium hydrosulfite was added to the 10% resazurin solution to shift the solution from purple to pink.

Biofilm Growth

Biofilm samples were grown in CDC Biofilm Reactors (Biosurface Technologies Corp., Bozeman, MT) with the headspace sparged with anoxic $N_2$ gas. Separate reactors were grown for each strain (Δ*dvu1025* (wild-type), *Δdvu1012, Δdvu1545)*. Reactors were inoculated with 40 ml of an exponential-phase culture and allowed to grow in batch mode for approximately 24 hours. The medium pump flow rate was set to 0.7 ml/min ($D = 0.11^{-h}$)) 24 hours post-inoculation and maintained continuous flow until final samples were harvested. Metal coupon dimensions were 7.1 x 1.25 x 0.1cm. Modified coupon holders were used as previously described to provide increased material surface area (Clark et al., 2012).

Biofilm and Coupon Harvesting

Biofilm coupons were removed from the reactor and biofilm was immediately removed from the coupon using a sterile scraper. Biomass was scraped into 5 ml of $dH_2O$ and vortexed prior to growth parameter measurements or stored at -20°C for later analyses. Biomass was boiled at 100°C for 10 minutes before protein and carbohydrate measurements were taken. Protein concentrations were measured with a Qubit Protein Assay Kit (Life Technologies, Carlsbad, CA). Carbohydrate concentration was measured as previously described (Clark et al. 2006). Lactate and acetate were quantified using an Ultimate 3000 High Performance Liquid Chromatography instrument with a 300mm x 7.8mm HPLC Organic Acid Analysis Aminex HPX-87H Ion Exclusion Column (Thermo Scientific, Dionex Germering, Germany). Sulfate was measured with by Ion

Chromatography (Dionex) with an IonPac AS11 column (Dionex). Sulfide was determined using a colorimetric copper sulfate method with sodium sulfide as the standard.

Preparation of Samples and Imaging

Biofilm samples were fixed to each surface by treatment in Karmovsky's Fixative (3.2% w/v paraformaldehyde, 2.5%w/w glutaraldehyde, 0.05M sodium cocodylate) for 16 h. Samples were soaked 4x in $dH_2O$ for 5 min to remove fixative. Ethanol (EtOH) dehydration involved 5 minutes in 25% EtOH, 5 minutes in 50% EtOH, 5 minutes in 75% EtOH, 15 minutes in 95% EtOH, and 2x 45 minutes in 100% EtOH before storage in 100% EtOH. Dehydrated samples were dried in a Tousimis Samdri-795 Critical Point Dryer (Tousimis Research Corporation, Rockland MD) using liquid $CO_2$ and a 10 min purge time. Dried samples were coated with Iridium for 30 seconds with an Emitech K575X Sputter Coater. Samples were imaged with a Zeiss Supra 55VP Field Emission Scanning Electron Microscopy (FE-SEM) (Carl Zeiss, Oberkochen, Germany) at 1keV. Several SEM images were taken of large areas of biofilm along with EDX (electron dispersion x-ray spectroscopy) spectra. The relative percentages of elements present in each image were obtained from the EDX spectra and averaged for each strain. These data were collected with a custom-built Integrated Auger Nanoprobe (Physical Electronics Chanhassen, MN). The OCT (optical coherence tomography) images were taken of a freshly sampled and hydrated corrosion biofilm grown on 1018 carbon steel with a GAN210 Optical Coherence Tomography imaging system (ThorLabs, Newton, NJ) at 25X magnification.

Results and Discussion

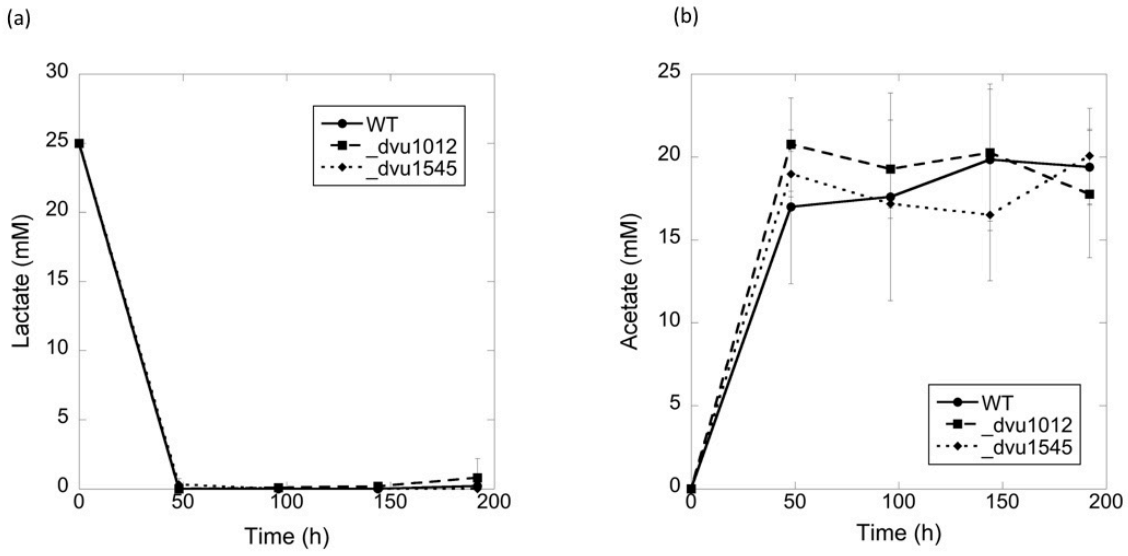


Figure 1. (a) Lactate and (b) acetate levels of planktonic medium in CDC reactors for *Desulfovibrio vulgaris* Hildenborough strains.

Lactate/acetate

Planktonic lactate and acetate levels were measured to assess carbon source utilization by each strain in the CDC biofilm reactors throughout each reactor run (Figure 1). The medium contains 25mM lactate and 16.6mM sulfate concentrations. Because *D. vulgaris* consumes lactate and sulfate in a 2:1 ratio, and the media provided less than a 2:1 ratio of lactate to sulfate, consumption of all lactate was expected after the reactor reached steady-state (lactate consumption and acetate production). After 48 hours of growth, lactate was extremely low to undetectable for each of the three tested strains. *D. vulgaris* oxidizes lactate to acetate in a 1:1 ratio, so the amount of lactate consumed should be equimolar to the concentration of acetate produced. There is variability in the measured acetate concentrations in the three strains over the time tested that all range

from approximately 16 to 20 mM although strain Δ*dvu1012* appeared to have a faster initial rate of acetate production (Figure 1b). All the measured acetate concentrations are less than the 25 mM of lactate that was consumed, and likely represents the utilization of carbon for biomass production. Planktonic growth in the biofilm reactors was not significantly different between the three strains.

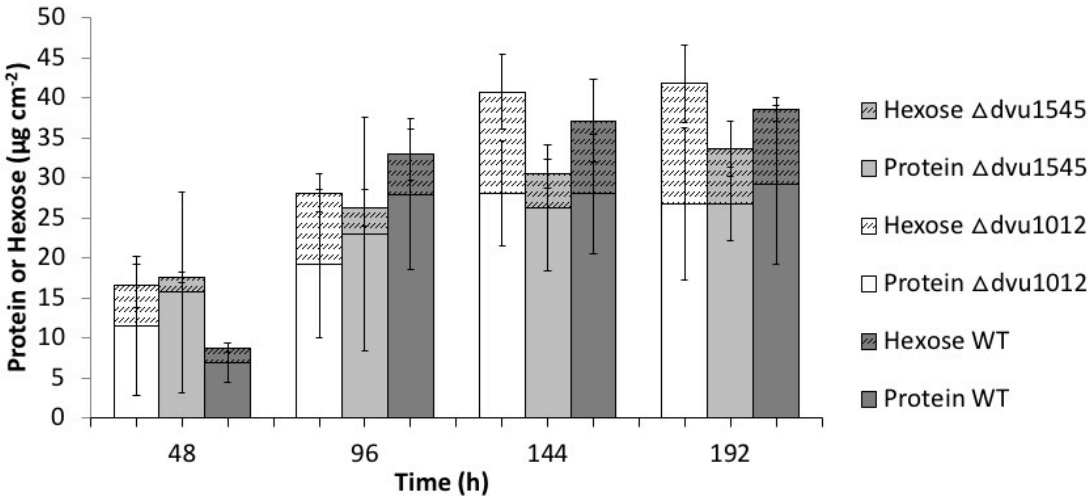


Figure 2. Hexose and protein levels of WT, *Δdvu1012*, and *Δdvu1545* biofilms during 192 h CDC reactor growth on 1018 carbon steel.

Protein/hexose

Biofilm protein and hexose levels were measured to indicate the distribution of biomass in the three tested *D. vulgaris* strains (Figure 2). After 48 hours of growth, the wild-type strain had, on average, lower protein levels than the Δ*dvu1012* or Δ*dvu1545* strains. The higher biofilm protein levels for the mutant strains corresponded with the slightly higher acetate levels initially produced. Hexose levels were considerably lower than the protein levels at 48 hours for all three strains, with hexose-to-protein ratios of 0.44, 0.11, 0.27 for Δ*dvu1012*, Δ*dvu1545*, and wild-type, respectively. At 96 hours of

cultivation, wild-type biofilm protein levels are slightly higher than the two deletion strains, and Δ*dvu1545* has the lowest protein and highest carbohydrate levels compared to wild-type and Δ*dvu1012*. Interestingly, the carbohydrate-to-protein ratios are 0.46, 0.14, and 0.18 for *Δdvu1012*, *Δdvu1545*, and wild-type respectively, and the Δ*dvu1012* biofilm carbohydrate-to-protein ratio is 2.5 to 3-fold higher compared to the other two strains. At 144 hours of biofilm cultivation, the protein levels are quite similar for all three tested strains; however, the hexose is at least twice as high in wild-type and *Δdvu1012* biofilms compared to the *Δdvu1545* biofilm. Hexose-to-protein ratios are 0.45, 0.16, and 0.32 for *Δdvu1012*, *Δdvu1545*, and WT. At the final 192 hour time point, protein levels are very similar to the 144 hour levels (*i.e.*, biofilm protein levels have reached steady-state), but carbohydrate levels continued to increase for the mutant strains.

The hexose-to-protein ratios are 0.56, 0.25, and 0.32, for the *Δdvu1012*, *Δdvu1545*, and wild-type strains, respectively (Figure 2), and overall the Δ*dvu1012* biofilm had the highest carbohydrate levels. These results were compared to the results in Krantz et al. (Chapter 2), which grew the same strain biofilm on glass. The differences in hexose levels between strains in that study were minimal, and not as pronounced when grown on 1018 carbon steel. Cultures of *Desulfovibrio* G20 were shown to contain more carbohydrate, namely mannose, glucose, and galactose, when grown in the presence of mild steel compared to no surface controls (Beech et al., 1991 and recent results by Krantz et al. (2019) with *Desulfovibrio alaskensis* G20 (G20) grown on 1018 carbon steel coupons, G20 produced more hexose than protein in the biofilm biomass. Differences in biofilm physiology between members of the *Desulfovibrio* genus are demonstrated in

these results with *D. vulgaris* where considerably less hexose is produced in biofilm grown on 1018 carbon steel.

Recent work demonstrated that the EPS of a sulfate-reducing biofilm initially decreased corrosion of X80 steel but corrosion increased as the biofilm further developed (Shu et al., 2018). Interestingly, the EPS extracted from waste activated sludge was recently shown to act as a mixed-type corrosion inhibitor with mild steel, most likely acting as a protective film that protects the metal surface from the corrosive environment (Go et al., 2019). The presented results indicate that *Desulfovibrio* G20 biofilms produces more carbohydrate when grown on 1018 carbon steel compared to glass, and that the Δ*dvu1012* mutant produced elevated levels of carbohydrate compared to wild-type.

Sulfate

The provided media contained 16.6 mM sulfate and all 3 strains had similar planktonic concentrations of approximately 7 mM (steady-state). Approximately 10mM sulfate was utilized that correlated to the 25 mM of lactate that was consumed in the medium (Figure S1). The 2:1 ratio of lactate: sulfate consumption is not observed to be exact, but the difference is attributed to assimilation of lactate as a carbon source into biomass.

Sulfide

Planktonic sulfide (Figure 3a) was higher on average in wild-type than the Δ*dvu1012* and Δ*dvu1545* mutant strains for the 48, 96, and 144 hour samples. By the final 192 hour sample, wild-type and Δ*dvu1545* sulfide levels were nearly equal while

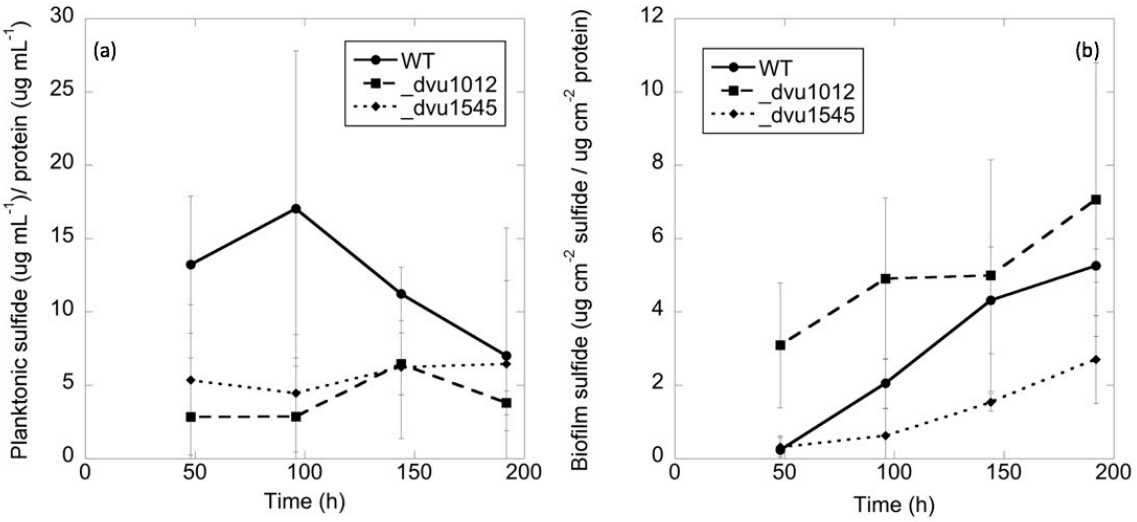


Figure 3. Sulfide normalized to protein levels in the planktonic (a) and biofilm (b) fractions.

Figure 3. (a) Planktonic sulfide numbers normalized to planktonic protein levels and (b) biofilm sulfide numbers normalized to surface area and biofilm protein levels for the different *Desulfovibrio vulgaris* Hildenborough strains grown in CDC biofilm reactors on 1018 carbon steel.

Δ*dvu1012* was slightly lower. There is overlap in the error bars for all of the samples, so differences are not statistically significant. Biofilm measurements showed that, on average, the *Δdvu1012* strain had the highest sulfide concentration (Figure 3b). The wild-type biofilm sulfide levels were intermediate between Δ*dvu1012* and Δ*dvu1545* with Δ*dvu1545* having the lowest sulfide content. The error bars for the *Δdvu1012* 144 and 192 hour time points are large and overlap with wild-type and Δ*dvu1545* samples, making those differences not statistically significant. The overall trends show that the *Δdvu1012* strain has more sulfide associated with biofilm biomass and is suggestive of higher sulfate-reduction in the biofilm phase compared to wild-type and Δ*dvu1545*. The decreased sulfide in the *Δdvu1545* biofilm is not suggestive of decreased biofilm biomass as protein and hexose levels in the last 3 time points are similar between the three strains

and Δ*dvu1545* has higher initial biofilm similar to *Δdvu1012* compared to wild-type (Figure 2). It is interesting to speculate that given the role of DVU1012 and DVU1545 as structural biofilm proteins, the altered extracellular environment of *Δdvu1012* and *Δdvu1545* biofilm may impact sulfide association and/or diffusion from the biofilm proper. For example, in the *Δdvu1012* biofilm, the elevated carbohydrate levels may impact the association of sulfides with biofilm material or vice versa with the *Δdvu1545* biofilm (*i.e.*, lower carbohydrate = lower biofilm associated sulfides).

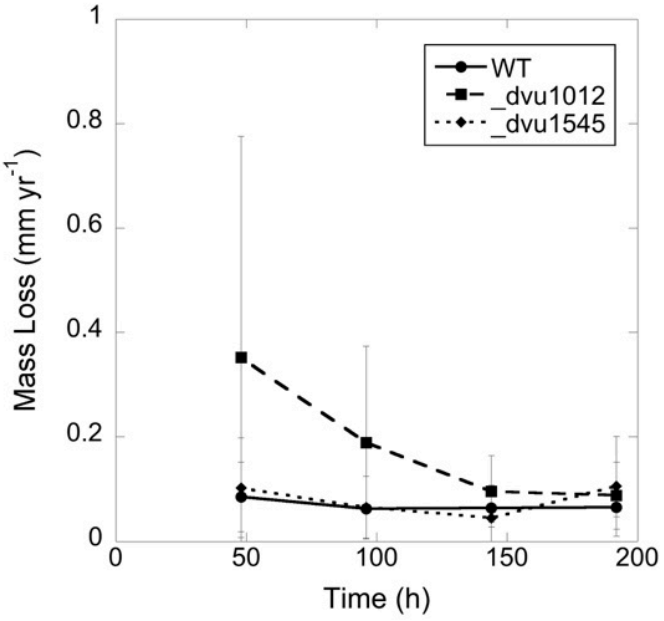


Figure 4. Corrosion rate measured by mass loss in the steel coupons for wild-type, *Δdvu1012*, and *Δdvu1545* biofilms.

Corrosion Rate

Mass loss of the 1018 carbon steel coupons was quantified after exposure to biofilm growth for 192 h under sulfate-reducing conditions (Figure 4). The corrosion rate for the *Δdvu1012* strain was higher in the 48 hour and 96 hour samples than the

*Δdvu1545* and wild-type strains. More specifically, the 48 hour corrosion rate for *Δdvu1012* was 0.35 mm $yr^{-1}$ and was 3.5-fold higher than the rate for *Δdvu1545* and wild-type that were 0.1 and 0.09 mm $yr^{-1}$, respectively. The *Δdvu1012* 96 hour samples had a 3-fold increase compared to *Δdvu1545* and WT (0.19 mm $yr^{-1}$ compared to 0.07 and 0.06 mm $yr^{-1}$, respectively). Mature cultures were used to inoculate the reactors, and cell inocula were quantified $O.D._{.}^{600}$ readings, but some degree of variability could have been introduced with varying cell inoculations.

The data suggest that the *Δdvu1012* strain may be initially more corrosive than the other two strains, but over the length of the experiment, the three strains appear to have a similar average corrosion rate. Corrosion can occur slowly over time, or quickly if the conditions are favorable (Updegraff 1955). Favorable conditions include the carbon steel surface being freshly exposed to the growth media before the formation of a passivation layer of corrosion products. If that exposure of a fresh metal surface co-occurs with the introduction of a higher cell concentration inoculum with increased sulfide content, the initial corrosion rate will likely be higher. However, reactors for all three strains were inoculated in the same manner with similar levels of cells and metal surfaces. Corrosion rate is calculated by dividing the mass loss by a time interval, so if a majority of the corrosion occurs in the first day during those optimal conditions, the rate will lower over time as the mass loss is divided by an increasingly larger time interval. That is likely the explanation for the *Δdvu1012* corrosion rate results. The *Δdvu1545* and WT had less variation with the WT rate staying at 0.06 mm $yr^{-1}$ and *Δdvu1545* at approximately 0.1 mm $yr^{-1}$ (Figure 4). The results suggested that initial biofilm formation was altered for

both mutant biofilms on 1018 carbon steel, perhaps attributed to surface conditioning that impacts initial susceptibility to chemical and/or electrical attack of the metal. However, further work is needed to better understand the relationship between the biofilm EPS matrix, biochemical activity, and the substratum surface.

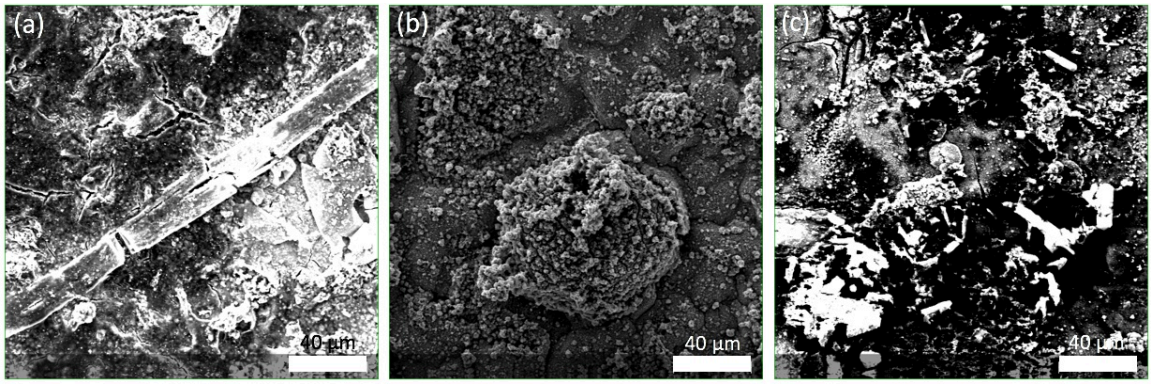


Figure 5. Scanning Electron Microscopy (SEM) images of corrosion biofilms for (a) wild-type, (b) *Δdvu1012*, and (c) *Δdvu1545* strains.

Electron Microscopy and EDX

In the wild-type biofilm after 192 h of growth, large crystal structures were observed (Figure 5a) on top of an even layer of corrosion products. The *Δdvu1012* biofilm (192 h) showed corrosion bubbles but the large crystals observed in wild-type biofilms were not prevalent (Figure 5b). The *Δdvu1545* biofilm (192 h) had some smaller crystal-like structure distributed across the corrosion biofilm surface (Figure 5c). Using Electron Dispersive X-ray Spectroscopy (EDX), the relative abundance of elements could be visualized through false-coloring. The same three SEM images were overlaid with EDX data for abundances of oxygen, magnesium, phosphorus, and sodium (Figures 6a-c). The crystal structures observed in wild-type biofilms likely consisted of

magnesium phosphate crystals due to the high abundance of magnesium, phosphorus, and oxygen. Sodium can be observed in the textured background of corrosion products.

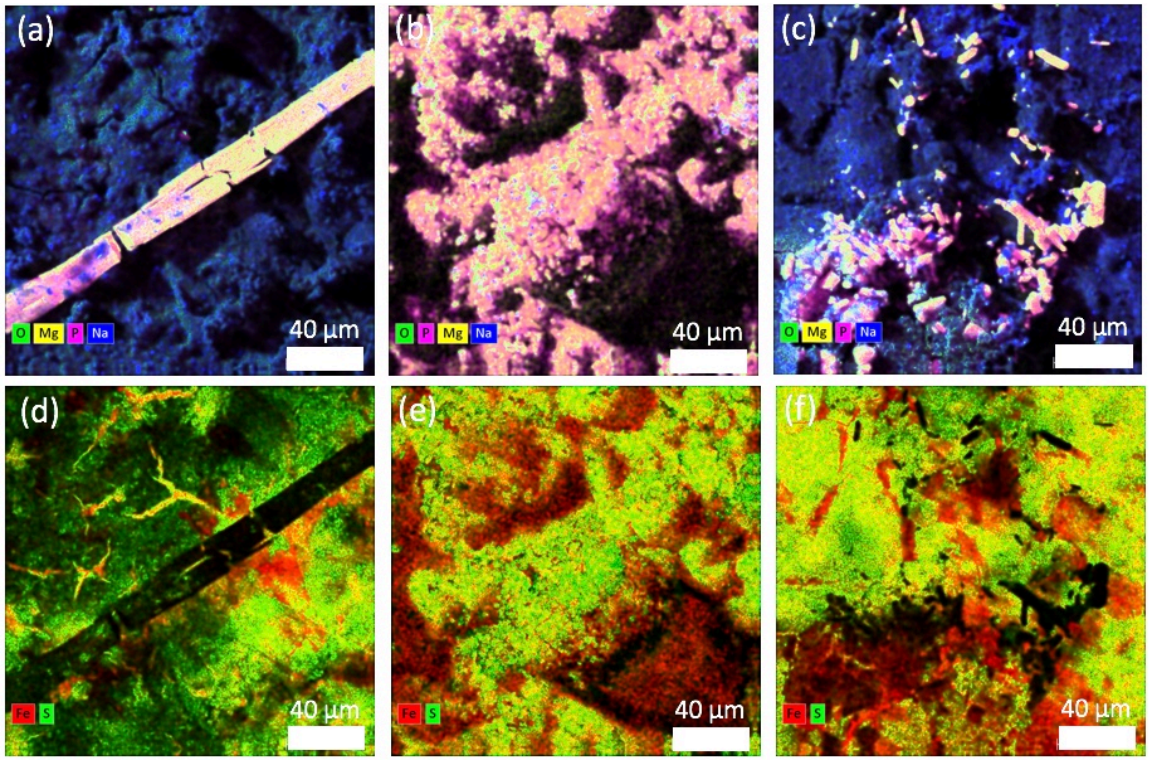


Figure 6. SEM images of corrosion biofilms colorized to indicate the presense of oxygen, phosphorus, magnesium, and sodium. (a) WT, (b) *Δdvu1012*, and (c) *Δdvu1545*. The same images colorized to indicate the presence of iron and sulfur (d) WT, (e) *Δdvu1012*, and (f) *Δdvu1545*.

Magnesium, phosphate, and sodium are provided as salts in the growth medium and likely interact with the development of corrosion minerals during biofilm growth and activity. The *Δdvu1012* biofilm has evenly distributed levels of magnesium and phosphorus across the whole surface and likely represents magnesium phosphate precipitates (Figure 6b). Similar to the wild-type biofilm, the *Δdvu1545* biofilm has crystals with high abundance of magnesium, phosphate, and oxygen on a bed of minerals high in sodium (Figure 6c). The crystals are smaller than those in the WT strain, though

in both cases they seem to have formed completely above the rest of the corrosion products. Corresponding to the higher carbohydrate and associated sulfide levels of *Δdvu1012* biofilm, the biofilm associated precipitates are very different from wild-type biofilm. Previous studies have shown that divalent cations can impact biofilm cohesiveness (Patrauchan et al., 2005), and recent work has shown that mixed species biofilms in hard and soft drinking water have different physical characteristics (Shen et al., 2018). Both DVU1012 and DVU1545 are predicted to contain putative calcium binding domains but the potential role of divalent cations in *D. vulgaris* biofilm formation and activity are not known.

The wild-type biofilm had a high abundance of sulfur with patches of iron, particularly in the cracks in which material could be visualized below the surface (Figure 6d). The *Δdvu1012* biofilm had more iron present on the overall biofilm surface mixed in with sulfur (Figure 6e). The *Δdvu1545* biofilm had areas of high sulfur content with higher iron levels observed in the cracks/low patches of the biofilm/precipitate surface (Figure 6f). The observed crystal structures for wild-type and *Δdvu1545* biofilm do not appear to contain iron or sulfur. The formation of iron sulfide precipitates have been routinely reported for *Desulfovibrio* cultivated under sulfate-reducing conditions in the presence of iron (Picard et al., 2018; references therein), but the potentially different minerals formed by biofilm are not known nor the impact of EPS constituents (*e.g.*, EPS carbohydrates and proteins).

Elemental Quantification

The appearance of the corrosion products and the types of structures observed differed significantly between wild-type and mutant strains, so the relative elemental composition of each SEM image was measured and averaged for each strain in attempt to quantify differences. Corrosion products are notoriously hard to quantify, but a semi-quantitative first step was taken with EDX (Figure 7). While there appears to be more carbon in the wild-type biofilms than the *Δdvu1012* or *Δdvu1545* (Figure 7a), carbon is not accurately measured with EDX. There were small differences in the iron and sulfur levels between the three biofilms, and *Δdvu1545* appeared to have lower sulfur levels (not statistically significant). The oxygen levels in *Δdvu1545* were higher than the other two biofilms, and these results suggested potentially different mineral oxides. Sodium levels in the *Δdvu1012* biofilm were higher than the other two strains, and the *Δdvu1012* and *Δdvu1545* biofilms appeared to have elevated magnesium levels compared to wild-type (Figure 7).

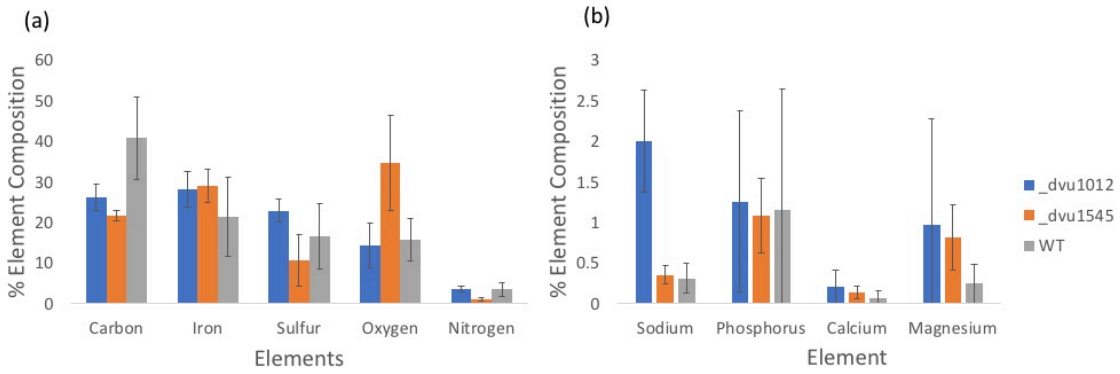


Figure 7. Elemental composition of corrosion biofilms measured by EDX (Electron Dispersion X-ray Spectroscopy). (a) More abundant elements. (b) Less abundant elements.

## Conclusions

While previous work by Krantz et al. (Chapter 3) characterized the *D. vulgaris* strains wild-type, *Δdvu1012,* and *Δdvu1545* as biofilms on glass, this is the first study to examine the role of these proteins in a corrosion biofilm on 1018 carbon steel. The deletion of the *dvu1545* gene allows for slightly better planktonic growth, as indicated by the increased O.D. 600 values, but the sulfide levels in the *Δdvu1545* strain, which would be expected to be higher with increased growth, are indistinguishable from the *Δdvu1012* sulfide levels. As observed with glass, the two mutant strains were able to form biofilm on 1018 carbon steel; however, rates and composition of biofilm growth displayed differences with wild-type. Both mutant biofilms had higher initial biofilm formation, but only the *Δdvu1012* biofilm had a corresponding higher initial corrosion rate. Both overall biofilm protein and corrosion rates were similar among the strains after longer cultivation times.

The SEM images show large magnesium phosphate crystals associated with the wild-type biofilm surface, and similar crystals are lacking in the mutant biofilms. In contrast, phosphorus and magnesium seem to be evenly distributed along the *Δdvu1012* biofilm surface, and *Δdvu1012* biofilm was also highest in sodium levels. The EDX data shows an increase in the abundance of oxygen in the *Δdvu1545* biofilm/corrosion products that could be suggestive of different mineral oxides. Given that DVU1012 and DVU1545 have putative binding domains for divalent cations and both mutant biofilms had elevated levels of magnesium and calcium compared to wild-type, divalent cations could contribute to controlling physical attributes (*e.g.*, stiffness) of *D. vulgaris* biofilms

via the presumptive DVU1012 and DVU1545 proteins. These physical attributes could impact not only cohesiveness of the biofilm but also mineral precipitation, diffusivity, and activity of the biofilm matrix. Future work is needed to elucidate the exact role(s) of divalent cations in sulfate-reducing biofilms.

## Acknowledgements

This material is funded by ENIGMA- Ecosystems and Networks Integrated with Genes and Molecular Assemblies (http://enigma. lbl.gov), a Scientific Focus Area Program at Lawrence Berkeley National Laboratory is based upon work supported by the U.S. Department of Energy, Office of Science, Office of Biological & Environmental Research under contract number DE-AC02-05CH11231.

Electron microscopy was performed in part at the Montana Nanotechnology Facility, a member of the National Nanotechnology Coordinated Infrastructure (NNCI), which is supported by the National Science Foundation (Grant# ECCS-1542210).

References

Picard, A., Gartman, A., Clarke, D. R. & Girguis, P. R. Sulfate-reducing bacteria influence the nucleation and growth of mackinawite and greigite. *Geochim. Cosmochim. Acta* **220**, 367–384 (2018).

Shen, Y. *et al.* Effect of divalent ions and a polyphosphate on composition, structure, and stiffness of simulated drinking water biofilms. *NPJ Biofilms Microbiomes* **4**, 15 (2018).

Patrauchan, M. A., Sarkisova, S., Sauer, K. & Franklin, M. J. Calcium influences cellular and extracellular product formation during biofilm-associated growth of a marine Pseudoalteromonas sp. *Microbiology* **151**, 2885–2897 (2005).

Go, L. C., Holmes, W., Depan, D. & Hernandez, R. Evaluation of extracellular polymeric substances extracted from waste activated sludge as a renewable corrosion inhibitor. *PeerJ* **7**, e7193 (2019).

Shu, Y. *et al.* Characteristics of SRB Biofilm and Microbial Corrosionof X80 Pipeline Steel. *Acta Metall. Sinica* **54**, 1408–1416 (2018).

Beech, I. B., Gaylarde, C. C., Smith, J. J. & Geesey, G. G. Extracellular polysaccharides from Desulfovibrio desulfuricans and Pseudomonas fluorescens in the presence of mild and stainless steel. *Appl. Microbiol. Biotechnol.* **35**, 65–71 (1991).

Guo, Z., Liu, T., Cheng, Y. F., Guo, N. & Yin, Y. Adhesion of Bacillus subtilis and Pseudoalteromonas lipolytica to steel in a seawater environment and their effects on corrosion. *Colloids Surf. B Biointerfaces* **157**, 157–165 (2017).

Beech, I. B. & Gaylarde, C. C. Recent advances in the study of biocorrosion: an overview. *Rev. Microbiol.* **30**, 117–190 (1999).

Updegraff, D. M. Microbiological Corrosion of Iron and Steel—A Review. *Corrosion* **11**, 44–48 (1955).

Krantz, G. P. *et al.* Bulk phase resource ratio alters carbon steel corrosion rates and endogenously produced extracellular electron transfer mediators in a sulfate-reducing biofilm. *Biofouling* 1–15 (2019).

Whitney, W. R. THE CORROSION OF IRON. *J. Am. Chem. Soc.* **25**, 394–406 (1903).

Clark, M. E., Edelmann, R. E., Duley, M. L., Wall, J. D. & Fields, M. W. Biofilm formation in Desulfovibrio vulgaris Hildenborough is dependent upon protein filaments. *Environ. Microbiol.* **9**, 2844–2854 (2007).

Klonowska, A. *et al.* Hexavalent chromium reduction in Desulfovibrio vulgaris Hildenborough causes transitory inhibition of sulfate reduction and cell growth. *Appl. Microbiol. Biotechnol.* **78**, 1007–1016 (2008).

Clark, M. E. *et al.* Transcriptomic and proteomic analyses of Desulfovibrio vulgaris biofilms: Carbon and energy flow contribute to the distinct biofilm growth state. *BMC Genomics* **13**, (2012).

Enning, D. *et al.* Marine sulfate-reducing bacteria cause serious corrosion of iron under electroconductive biogenic mineral crust. *Environ. Microbiol.* **14**, 1772–1787 (2012).

Clark, M. E. *et al.* Temporal Transcriptomic Analysis as Desulfovibrio vulgaris Hildenborough Transitions into Stationary Phase during Electron Donor Depletion. *Appl. Environ. Microbiol.* **72**, 5578–5588 (2006).

Heidelberg, J. F. *et al.* The genome sequence of the anaerobic, sulfate-reducing bacterium Desulfovibrio vulgaris Hildenborough. *Nat. Biotechnol.* **22**, 554–559 (2004).

Enning, D. & Garrelfs, J. Corrosion of iron by sulfate-reducing bacteria: new views of an old problem. *Appl. Environ. Microbiol.* **80**, 1226–1236 (2014).

Supplementary Information

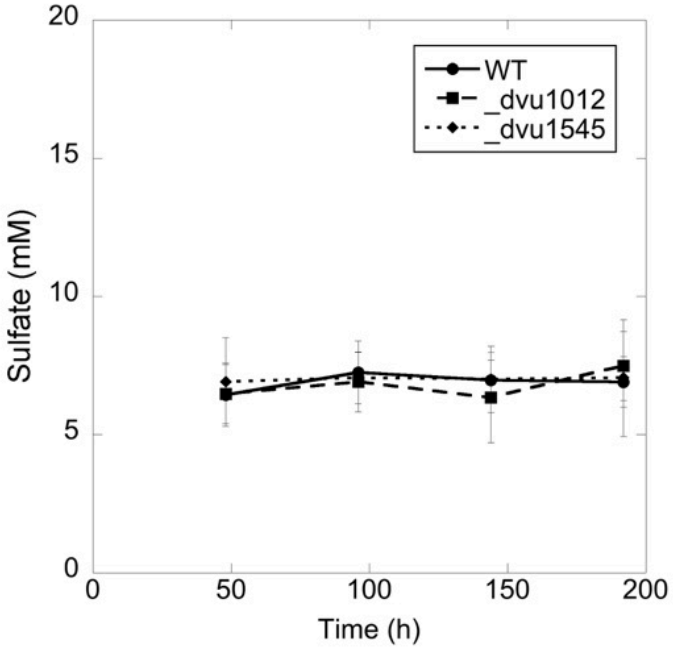


Figure S1. Planktonic sulfate concentrations from the *Desulfovibrio vulgaris* Hildenborough strains grown in CDC biofilm reactors.

# CHAPTER FIVE

## EPILOGUE

The work comprising my dissertation chapters have elucidated mechanisms that occur in the biofilm matrix. A great deal of the biofilm research done previously has focused on intercellular phenomena, and while some research has been done on EPS, much of that work has focused on carbohydrates. The biofilm matrix interactions that I examine in this dissertation involve coenzymes, proteins, and corrosion products. While these mechanisms have not been studied in depth with regard to SRB biofilm cells, they perform important functions in the systems where they occur.

While it has been long been known that SRB play a role in MIC, the mechanism by which it was thought to occur was indirectly through the production of sulfide, which then went on to corrode the steel in what is referred to as CMIC. Results published by Enning et al. 2012 demonstrated that SRB were capable of corroding mild steel through another electron uptake process called EMIC. Kato 2016 stated that EMIC can occur through direct electron uptake by the cells being in direct contact with the zero-valent iron or indirectly through an extracellular electron transfer molecule (EET). Li et al. 2018 refers to these mechanisms as direct electron transfer (DET) or mediated electron transfer (MET). Kato 2016 also mentioned that it was unclear whether all bacteria and archea use one similar system for EET, or if they have each evolved their own.

Kato 2016 stated that the field of EET-EMIC remains controversial because the specific mechanisms by which EMIC capable organisms cause corrosion are unresolved.

In chapter two I propose a mechanism that G20 uses to conduct MET. The proposed model is that when G20 is growing on a mild steel substrate and dissolved organic acids are unavailable for growth, it secretes a flavin-based extracellular electron transfer molecule enabling it to harvest high energy electrons from the zero valence iron in the steel. Previous to this work, it was known that carbon starvation induces increased corrosion on steel when SRB are present (Xu and Gu 2014, Dou et al. 2019). It was also known that adding synthetic FAD and riboflavin increases the corrosion rate beyond that of SRB alone (Li et al. 2015). My work connects these two observations and suggests that G20 can produce a flavin molecule which is utilized to harvest high energy electrons and increase corrosion under carbon starvation conditions. The point being made here is that when the SRB are running out of lactate, they use some of their remaining energy to synthesize flavin molecules and secrete them. The flavin molecules are catalysts that can help the cells harvest high energy electrons multiple times before they degrade. This cycling of extracellular electron transfer molecules makes the energy investment in synthesizing them worthwhile, and transforms the $Fe^0$ in the surrounding steel into a growth medium. Future research on the half-life of extracellular flavin molecules is warranted.

Kato 2016 also mentioned that it was unclear whether all bacteria and archea capable of MET use one similar system for, or if they have each evolved their own. Possible mechanisms include $H_2$ diffusion, flavin molecules, or naturally occurring inorganic chemicals.

The identity of the flavin molecule that is utilized by G20 remains unclear. Future work would do well to quantify all the MET capable molecules in the riboflavin pathway and compare their abundance between the EAL and EDL conditions. The metabolomics dataset from my study did identify metabolic features such as riboflavin and FAD, but the p-values on these features were too high to confidently identify them as those compounds. Identifying compounds is one of the current limitations of the untargeted metabolomics technique, as peaks observed in the method can often have multitude possible identities. Improvements in the chemical standards database would make the technique more accurate for a larger class of target molecules. Using targeted mass spectrometry on these samples could also identify these molecules. Performing RNAseq on both the EAL and EDL 1018 carbon steel biofilms would provide additional insight into how G20 is using the riboflavin pathway under these nutrient limited conditions.

It is interesting that G20 cells appear to be using a flavin extracellular electron transfer molecule for electron harvest while the biofilm cells are encased in conductive corrosion products. Perhaps the $FeS_x$ minerals are not conductive enough to provide electrons at the rate needed for growth, or maybe they are using both direct and indirect mechanisms of obtaining high energy electrons while anchored in the biofilm.

Zooming out to the industry wide impact of my research in this area, these results have relevance to how the oil industry manages its corrosion mitigation programs. G20 depends on sulfate to grow and many oil platforms are injecting seawater into the rock formations to enhance oil recovery. Seawater contains on average 28mM of sulfate

which increases the sulfate levels in the produced oil. For comparison, my growth media contains 15mM of sulfate, so increasing the sulfate content of the oil will push the nutrient ratio in the EDL direction which creates the conditions for higher corrosion rates. To address this problem, oil companies have started adding nitrate to injection water to encourage nitrate reducing bacteria to outcompete SRB. But doing so selects for iron corrosion by nitrate reducers and creates an entirely separate problem (Lahme et al. 2018). Removal or reduction of the sulfate from the injection water, while difficult, is a more effective solution to corrosion mitigation.

Previous to the results I present in chapter 3, the specific protein interactions that occur in the extracellular matrix of a sulfate-reducing bacterial biofilm that allow it to stick to a surface was poorly understood. It was known that the biofilm was mostly protein content (Clark et al. 2007), but the structure and function of those proteins were unknown. The proteins DVU1012 and DVU1545 were chosen because they were the two most abundant proteins in the DvH biofilm, and were very large at 3038 and 2414 amino acids. I hypothesized that peptides requiring that much energy to synthesize and maintain at abundant levels must be important. Together with Dr. Kara De Leon, we demonstrated that they were essential for biofilm formation (De Leon et al. 2017). But we didn't know why they were so important, as their structure and function was unknown. I used the I-TASSER structure prediction tool suite to predict models for the folded proteins. The toolset is limited to peptides of 1500 amino acids in length, and I used an overlapping prediction approach to create the folded models as both proteins were significantly longer than the limit. The structure predictions provided a visual

representation of where the amino acids were in 3 dimensional space, and as part of the threading algorithm, it identified the nearest solved crystal structure homologs. The publications associated with these solved crystal structures provided greater insight into what functions the homologs had, and suggested similar functions that DVU1012 and DVU1545 might perform. The I-TASSER data suggested that both proteins have structure that is quite similar to bacterial toxin proteins that have stacked wraps of β-sheets that form a barrel structure. Single particle analysis in collaboration with Dr. Peter Walian yielded a hollow structural envelope for DVU1012 that looked quite similar to the predicted structure from I-TASSER, providing further evidence that the predictions were accurate. TEM images show a barrel structure similar in size and shape to DVU1012 bound between cells. DVU1012 has a protein adhesion site in the Von Willebrand Type A (VWA) domain, so I hypothesized that it was playing a structural role in the biofilm helping cells stick together. I also hypothesized that these structural proteins would be important in responding to shear force, since it is one of the main physical disturbances that a hydrated biofilm must respond to. The same biofilm experiments were run as before, but at an increased stir rate of 80rpm instead of 50rpm. The increased shear force caused a large increase in biofilm protein and density in the wild-type strain, but a decrease in the *Δdvu1012/Δdvu1545* strain biofilm, suggesting DVU1012 and DVU1545 are essential for the biofilm's ability to tolerate increased shear force. These are the first results to identify protein components necessary for a SRB biofilm to respond to shear force. The fact that these proteins are necessary for biofilm formation and for the biofilm to respond to shear are the most significant results

presented in my dissertation. This information advances the knowledge of protein mechanisms in the extracellular matrix of an SRB biofilm.

Previous work by Rodesney et al. 2017 demonstrated how the envelope protein PilY1 is required in *Pseudomonas* for shear force sensing and leads to cyclic-di-GMP signaling and biofilm formation. PilY1 has weak similarity to the VWA domain. DVU1012 and DVU1545 may play a similar role in a DvH biofilm. Future work examining whether these two proteins are involved in sensing and catalyzing signal transduction of the presence of shear force is warranted. Crystal structures of both proteins would also confirm the accuracy of the structural predictions, though the challenges associated with cloning and overexpressing a 3038 amino acid protein are noteworthy. In collaboration with Dr. Peter Walian, I made antibodies to stain for DVU1012 and DVU1545. These antibodies did not adhere to a WT DvH biofilm, unfortunately. Developing antibodies that successfully target these proteins would be helpful in visualizing where they localize in a biofilm. The most promising of future experiments would be to use the antibodies for a protein pulldown assay to isolate and sequence the protein binding partners that are associated with DVU1012 and DVU1545. Identifying the signaling pathways and binding partners would greatly expand the knowledge of how an SRB biofilm anchors and regulates itself.

The VWA domain present in DVU1012 is of particular interest because it is an adhesion domain. The most widely studied VWA domain example is the human Von Willebrand Factor (VWF). This protein is present in low levels in the bloodstream in a globular state and initiates blood clot formation. The active form of VWF is about 2000

amino acids and contains three VWA domains and multiple other types of Von Willebrand domains. When a person gets a cut or scrape, it exposes Von Willebrand domains in collagen fibers. The Von Willebrand factor VWA domains binds the collagen domains with its own VWA domains, which anchors it to the site of injury. The shear force of blood flow causes a conformational change, stringing out the protein and exposing additional Von Willebrand domains. These bind other Von Willebrand factor proteins and recruit platelet cells, and a blood clot is formed. The presence of a VWA domain in an extracellular bacterial protein that is essential for shear force tolerance is interesting indeed. Perhaps DVU1012 plays a similar role where biofilm is formed under shear stress instead of a blood clot formation. I could hypothesize that biofilm formation is an evolutionary precursor to blood clot formation. Perhaps certain species of VWA protein-producing bacteria form initial clots of cells, and then other biofilm community members join the clump.

A pBLAST search of the DVU1012 VWA domain reveals it to be present in many *Pseudomonas* species, *Moritella viscosa,* fellow *Desulfovibrio* strains, and *Sulfuromonas*. Results from this search appear to be constrained to *proteobacteria.* Many of the results from the DVU1012 search were in T1SS retention module proteins or a T1SS targeted protein, particularly among the *Pseudomonas* species.

Using the human VWA domain as a bootstrap pBLAST search query expanded the scope of the VWA distribution. The resulting collection of sequences was used to construct the multiple alignment (Figure 6) and phylogenetic tree (Figure S3) in Chapter 3. Most of the search results using the human VWA query were blood-containing

eukaryotic species, but one notable exception was *Chlamydomonas reinhardtii*. The VWA domain appears to be widely distributed across biology.

Zooming out a bit, DvH is also a culprit in the biocorrosion of steel pipelines and is used as a model organism for such studies. Targeting the proteins DVU1012 and DVU1545 through specific proteases or other means might be a viable MIC mitigation strategy.

Keeping biocorrosion and these extracellular proteins in mind, chapter four examines the WT, *Δdvu1012,* and *Δdvu1545* strains on a 1018 carbon steel substrate. This data was generated in collaboration with my undergraduate assistant Marty Boyls-Davis. I hypothesized that the deletion strains would have different corrosion rates or caused a change in the corrosion minerals present the biofilm, because of the importance of these proteins to biofilm formation. An initial increase in the corrosion rate of *Δdvu1012* strain was observed, but most of the corrosion occurred only before the initial time point, as it averaged out by the end of the experiment. The corrosion products were quantified using EDX and averaged over several images taken of the biofilm of each strain. The *Δdvu1545* biofilm had a higher abundance of oxygen, and sodium was present in higher levels in the *Δdvu1012* strain compared to the other two strains. These results cannot be correlated to specific differences in mineral identities without performing Mossbauer spectroscopy as well, but it does suggest there are differences in the corrosion products between strains. While there were small differences between the corrosion rates and corrosion products of the strains, significant differences were not

observed. The DVU1012 and DVU1545 may not play a large role in corrosion behavior, or if they do, they are able to compensate for the loss of each other.

In conclusion, all of my results contribute to a better understanding of the extracellular mechanisms that occur in a monoculture SRB biofilm. This information is relevant to industrial systems where these bacteria cause damage to steel infrastructure and pose environmental risk, or future academic research that seeks to understand the regulation of SRB biofilm formation. I look forward to reading papers from groups who do so.

References

Li, Y. *et al.* Anaerobic microbiologically influenced corrosion mechanisms interpreted using bioenergetics and bioelectrochemistry: A review. *J. Mater. Sci. Technol.* **34**, 1713–1718 (2018).

Gracheva, M. A. *et al.* Mössbauer study of iron minerals transformations by Fuchsiella ferrireducens. *Hyperfine Interact.* **238**, 84 (2017).

Smith, J. S. & Miller, J. D. A. Nature of Sulphides and their Corrosive Effect on Ferrous Metals: A Review. *Br. Corros. J.* **10**, 136–143 (1975).

Rodesney, C. A. *et al.* Mechanosensing of shear by Pseudomonas aeruginosa leads to increased levels of the cyclic-di-GMP signal initiating biofilm development. *Proc. Natl. Acad. Sci. U. S. A.* **114**, 5906–5911 (2017).

Dou, W. *et al.* Electrochemical investigation of increased carbon steel corrosion via extracellular electron transfer by a sulfate reducing bacterium under carbon source starvation. *Corros. Sci.* (2019). doi:10.1016/j.corsci.2019.02.005

Lahme, S. *et al.* Metabolites of an oil field sulfide-oxidizing nitrate-reducing Sulfurimonas sp. cause severe corrosion. *Appl. Environ. Microbiol.* (2018). doi:10.1128/AEM.01891-18

Clark, M. E., Edelmann, R. E., Duley, M. L., Wall, J. D. & Fields, M. W. Biofilm formation in Desulfovibrio vulgaris Hildenborough is dependent upon protein filaments. *Environ. Microbiol.* **9**, 2844–2854 (2007).

De León, K. B. *et al.* Unintended Laboratory-Driven Evolution Reveals Genetic Requirements for Biofilm Formation by Desulfovibrio vulgaris Hildenborough. *MBio* **8**, (2017).

Kato, S. Microbial extracellular electron transfer and its relevance to iron corrosion. *Microb. Biotechnol.* **9**, 141–148 (2016).

Xu, D. & Gu, T. Carbon source starvation triggered more aggressive corrosion against carbon steel by the Desulfovibrio vulgaris biofilm. *Int. Biodeterior. Biodegradation* **91**, 74–81 (2014).

Li, H. *et al.* Extracellular Electron Transfer Is a Bottleneck in the Microbiologically Influenced Corrosion of C1018 Carbon Steel by the Biofilm of Sulfate-Reducing Bacterium Desulfovibrio vulgaris. *PLoS One* **10**, e0136183 (2015).

# REFERENCES CITED

Picard, A., Gartman, A., Clarke, D. R. & Girguis, P. R. Sulfate-reducing bacteria influence the nucleation and growth of mackinawite and greigite. *Geochim. Cosmochim. Acta* **220**, 367–384 (2018).

Shen, Y. *et al.* Effect of divalent ions and a polyphosphate on composition, structure, and stiffness of simulated drinking water biofilms. *NPJ Biofilms Microbiomes* **4**, 15 (2018).

Patrauchan, M. A., Sarkisova, S., Sauer, K. & Franklin, M. J. Calcium influences cellular and extracellular product formation during biofilm-associated growth of a marine Pseudoalteromonas sp. *Microbiology* **151**, 2885–2897 (2005).

Go, L. C., Holmes, W., Depan, D. & Hernandez, R. Evaluation of extracellular polymeric substances extracted from waste activated sludge as a renewable corrosion inhibitor. *PeerJ* **7**, e7193 (2019).

Shu, Y. *et al.* Characteristics of SRB Biofilm and Microbial Corrosionof X80 Pipeline Steel. *Acta Metall. Sinica* **54**, 1408–1416 (2018).

Beech, I. B., Gaylarde, C. C., Smith, J. J. & Geesey, G. G. Extracellular polysaccharides from Desulfovibrio desulfuricans and Pseudomonas fluorescens in the presence of mild and stainless steel. *Appl. Microbiol. Biotechnol.* **35**, 65–71 (1991).

Guo, Z., Liu, T., Cheng, Y. F., Guo, N. & Yin, Y. Adhesion of Bacillus subtilis and Pseudoalteromonas lipolytica to steel in a seawater environment and their effects on corrosion. *Colloids Surf. B Biointerfaces* **157**, 157–165 (2017).

Beech, I. B. & Gaylarde, C. C. Recent advances in the study of biocorrosion: an overview. *Rev. Microbiol.* **30**, 117–190 (1999).

Liu, Y. & Tay, J.-H. The essential role of hydrodynamic shear force in the formation of biofilm and granular sludge. *Water Res.* **36**, 1653–1665 (2002).

Scarascia, G. *et al.* Quorum sensing effect on the ability of Desulfovibrio vulgaris to form biofilm and to biocorrode carbon steel in saline conditions. *Appl. Environ. Microbiol.* (2019). doi:10.1128/AEM.01664-19

Stylo, M., Neubert, N., Roebbert, Y., Weyer, S. & Bernier-Latmani, R. Mechanism of Uranium Reduction and Immobilization in Desulfovibrio vulgaris Biofilms. *Environ. Sci. Technol.* **49**, 10553–10561 (2015).

Kurczy, M. E. *et al.* Comprehensive bioimaging with fluorinated nanoparticles using breathable liquids. *Nat. Commun.* **6**, 5998 (2015).

Rabus, R. *et al.* A Post-Genomic View of the Ecophysiology, Catabolism and

Biotechnological Relevance of Sulphate-Reducing Prokaryotes. *Adv. Microb. Physiol.* **66**, 55–321 (2015).

Holman, H.-Y. N. *et al.* Real-time molecular monitoring of chemical environment in obligate anaerobes during oxygen adaptive response. *Proc. Natl. Acad. Sci. U. S. A.* **106**, 12599–12604 (2009).

Brileya, K. A., Camilleri, L. B., Zane, G. M., Wall, J. D. & Fields, M. W. Biofilm growth mode promotes maximum carrying capacity and community stability during product inhibition syntrophy. *Front. Microbiol.* **5**, 693 (2014).

Yang, J. & Zhang, Y. I-TASSER server: new development for protein structure and function predictions. *Nucleic Acids Res.* **43**, W174–81 (2015).

Kaesche, H. *Corrosion of Metals: Physicochemical Principles and Current Problems*. (Springer Science & Business Media, 2012).

Smith, J. S. & Miller, J. D. A. Nature of Sulphides and their Corrosive Effect on Ferrous Metals: A Review. *Br. Corros. J.* **10**, 136–143 (1975).

Okamoto, A., Nakamura, R., Nealson, K. H. & Hashimoto, K. Bound Flavin Model Suggests Similar Electron-Transfer Mechanisms in Shewanella and Geobacter. *CHEMELECTROCHEM* **1**, 1808–1812 (2014).

Marsili, E. *et al.* Shewanella secretes flavins that mediate extracellular electron transfer. *Proc. Natl. Acad. Sci. U. S. A.* **105**, 3968–3973 (2008).

Updegraff, D. M. Microbiological Corrosion of Iron and Steel—A Review. *Corrosion* **11**, 44–48 (1955).

Rochex, A., Godon, J.-J., Bernet, N. & Escudié, R. Role of shear stress on composition, diversity and dynamics of biofilm bacterial communities. *Water Res.* **42**, 4915–4922 (2008).

El-Kirat-Chatel, S., Beaussart, A., Boyd, C. D., O'Toole, G. A. & Dufrêne, Y. F. Single-cell and single-molecule analysis deciphers the localization, adhesion, and mechanics of the biofilm adhesin LapA. *ACS Chem. Biol.* **9**, 485–494 (2014).

Rusconi, R., Guasto, J. S. & Stocker, R. Bacterial transport suppressed by fluid shear. *Nat. Phys.* **10**, 212 (2014).

Payne, D. E. & Boles, B. R. Emerging interactions between matrix components during biofilm development. *Curr. Genet.* **62**, 137–141 (2016).

Schooling, S. R. & Beveridge, T. J. Membrane vesicles: an overlooked component of the matrices of biofilms. *J. Bacteriol.* **188**, 5945–5957 (2006).

Hooper, S. L. & Burstein, H. J. Minimization of extracellular space as a driving force in prokaryote association and the origin of eukaryotes. *Biol. Direct* **9**, 24 (2014).

Odom, J. M. & Singleton, R. *The Sulfate-Reducing Bacteria: Contemporary Perspectives*. (Springer, New York, NY, 1993).

Odom, J. M. & Peck, H. D., Jr. Hydrogen cycling as a general mechanism for energy coupling in the sulfate-reducing bacteria, Desulfovibrio sp. *FEMS Microbiol. Lett.* **12**, (1981).

Foti, M. *et al.* Diversity, activity, and abundance of sulfate-reducing bacteria in saline and hypersaline soda lakes. *Appl. Environ. Microbiol.* **73**, 2093–2100 (2007).

Castro, H. F., Williams, N. H. & Ogram, A. Phylogeny of sulfate-reducing bacteria(1). *FEMS Microbiol. Ecol.* **31**, 1–9 (2000).

Pester, M., Knorr, K.-H., Friedrich, M. W., Wagner, M. & Loy, A. Sulfate-reducing microorganisms in wetlands - fameless actors in carbon cycling and climate change. *Front. Microbiol.* **3**, 72 (2012).

Krantz, G. P. *et al.* Bulk phase resource ratio alters carbon steel corrosion rates and endogenously produced extracellular electron transfer mediators in a sulfate-reducing biofilm. *Biofouling* 1–15 (2019).

Whitney, W. R. THE CORROSION OF IRON. *J. Am. Chem. Soc.* **25**, 394–406 (1903).

Hugenholtz, P., Pitulle, C., Hershberger, K. L. & Pace, N. R. Novel division level bacterial diversity in a Yellowstone hot spring. *J. Bacteriol.* **180**, 366–376 (1998).

Rabus, R. *et al.* The genome of Desulfotalea psychrophila, a sulfate-reducing bacterium from permanently cold Arctic sediments. *Environ. Microbiol.* **6**, 887–902 (2004).

Dupraz, C. & Visscher, P. T. Microbial lithification in marine stromatolites and hypersaline mats. *Trends Microbiol.* **13**, 429–438 (2005).

Spitz, O. *et al.* Type I Secretion Systems-One Mechanism for All? *Microbiol Spectr* **7**, (2019).

Kanonenberg, K., Spitz, O., Erenburg, I. N., Beer, T. & Schmitt, L. Type I secretion system-it takes three and a substrate. *FEMS Microbiol. Lett.* **365**, (2018).

Thomas, S., Holland, I. B. & Schmitt, L. The Type 1 secretion pathway - the hemolysin system and beyond. *Biochim. Biophys. Acta* **1843**, 1629–1641 (2014).

Holland, I. B., Schmitt, L. & Young, J. Type 1 protein secretion in bacteria, the ABC-transporter dependent pathway (review). *Mol. Membr. Biol.* **22**, 29–39 (2005).

Higgins, M. K. *et al.* Structure of the ligand-blocked periplasmic entrance of the bacterial multidrug efflux protein TolC. *J. Mol. Biol.* **342**, 697–702 (2004).

Pettersen, E. F. *et al.* UCSF Chimera--a visualization system for exploratory research and analysis. *J. Comput. Chem.* **25**, 1605–1612 (2004).

Kim, J.-S. *et al.* Crystal Structure of a Soluble Fragment of the Membrane Fusion Protein HlyD in a Type I Secretion System of Gram-Negative Bacteria. *Structure* **24**, 477–485 (2016).

Walian, P. J. *et al.* High-throughput isolation and characterization of untagged membrane protein complexes: outer membrane complexes of Desulfovibrio vulgaris. *J. Proteome Res.* **11**, 5720–5735 (2012).

Newell, P. D., Monds, R. D. & O'Toole, G. A. LapD is a bis-(3',5')-cyclic dimeric GMP-binding protein that regulates surface attachment by Pseudomonas fluorescens Pf0-1. *Proc. Natl. Acad. Sci. U. S. A.* **106**, 3461–3466 (2009).

Ivanov, I. E. *et al.* Atomic force and super-resolution microscopy support a role for LapA as a cell-surface biofilm adhesin of Pseudomonas fluorescens. *Res. Microbiol.* **163**, 685–691 (2012).

Persat, A. *et al.* The mechanical world of bacteria. *Cell* **161**, 988–997 (2015).

Bill Costerton, Gill Geesey, K.J. Cheng. How Bacteria Stick. (1978). doi:10.1038/scientificamerican0178-86

Flemming, H.-C. EPS-Then and Now. *Microorganisms* **4**, (2016).

Guo, S., Vance, T. D. R., Stevens, C. A., Voets, I. & Davies, P. L. RTX Adhesins are Key Bacterial Surface Megaproteins in the Formation of Biofilms. *Trends Microbiol.* **27**, 453–467 (2019).

Smith, T. J., Font, M. E., Kelly, C. M., Sondermann, H. & O'Toole, G. A. An N-Terminal Retention Module Anchors the Giant Adhesin LapA of Pseudomonas fluorescens at the Cell Surface: a Novel Subfamily of Type I Secretion Systems. *J. Bacteriol.* **200**, (2018).

Ost, G. S., Ng'ang'a, P. N., Lang, A. E. & Aktories, K. Photorhabdus luminescens Tc toxin is inhibited by the protease inhibitor MG132 and activated by protease cleavage resulting in increased binding to target cells. *Cell. Microbiol.* **21**, e12978 (2019).

Jackson, V. A., Busby, J. N., Janssen, B. J. C., Lott, J. S. & Seiradake, E. Teneurin Structures Are Composed of Ancient Bacterial Protein Domains. *Front. Neurosci.* **13**, 183 (2019).

Gatsogiannis, C. *et al.* Membrane insertion of a Tc toxin in near-atomic detail. *Nat. Struct. Mol. Biol.* **23**, 884–890 (2016).

Li, J. *et al.* Structural Basis for Teneurin Function in Circuit-Wiring: A Toxin Motif at the Synapse. *Cell* **173**, 735–748.e15 (2018).

Jackson, V. A. *et al.* Structures of Teneurin adhesion receptors reveal an ancient fold for cell-cell interaction. *Nat. Commun.* **9**, 1079 (2018).

Hobley, L., Harkins, C., MacPhee, C. E. & Stanley-Wall, N. R. Giving structure to the biofilm matrix: an overview of individual strategies and emerging common themes. *FEMS Microbiol. Rev.* **39**, 649–669 (2015).

Flemming, H.-C., Neu, T. R. & Wozniak, D. J. The EPS matrix: the 'house of biofilm cells'. *J. Bacteriol.* **189**, 7945–7947 (2007).

Karatan, E. & Watnick, P. Signals, regulatory networks, and materials that build and break bacterial biofilms. *Microbiol. Mol. Biol. Rev.* **73**, 310–347 (2009).

Flemming, H.-C. & Wingender, J. The biofilm matrix. *Nat. Rev. Microbiol.* **8**, 623–633 (2010).

Yang, J. *et al.* The I-TASSER Suite: protein structure and function prediction. *Nat. Methods* **12**, 7–8 (2015).

Roy, A., Kucukural, A. & Zhang, Y. I-TASSER: a unified platform for automated protein structure and function prediction. *Nat. Protoc.* **5**, 725 (2010).

Zhang, Y. I-TASSER server for protein 3D structure prediction. *BMC Bioinformatics* **9**, 40 (2008).

McCarty, P. L. Energetics and bacterial growth. *Organic compounds in aquatic environments* **1**, 157–172 (1971).

Grininger, M., Zeth, K. & Oesterhelt, D. Dodecins: a family of lumichrome binding proteins. *J. Mol. Biol.* **357**, 842–857 (2006).

Fieschi, F., Nivière, V., Frier, C., Décout, J. L. & Fontecave, M. The mechanism and substrate specificity of the NADPH:flavin oxidoreductase from Escherichia coli. *J. Biol. Chem.* **270**, 30392–30400 (1995).

Birss, V. I., Guha-Thakurta, S., McGarvey, C. E., Quach, S. & Vanýsek, P. An electrochemical study of the photolysis of adsorbed flavins. *J. Electroanal. Chem.* **423**, 13–21 (1997).

Treadwell, G. E. & Metzler, D. E. Photoconversion of riboflavin to lumichrome in plant tissues. *Plant Physiol.* **49**, 991–993 (1972).

Okamoto, A., Hashimoto, K., Nealson, K. H. & Nakamura, R. Rate enhancement of bacterial extracellular electron transport involves bound flavin semiquinones. *Proc. Natl. Acad. Sci. U. S. A.* **110**, 7856–7861 (2013).

Brutinel, E. D. & Gralnick, J. A. Shuttling happens: soluble flavin mediators of extracellular electron transfer in Shewanella. *Appl. Microbiol. Biotechnol.* **93**, 41–48 (2012).

Curley, G. P., Carr, M. C., Mayhew, S. G. & Voordouw, G. Redox and flavin-binding properties of recombinant flavodoxin from Desulfovibrio vulgaris (Hildenborough). *Eur. J. Biochem.* **202**, 1091–1100 (1991).

Ksenzhek, O. S. & Petrova, S. A. Electrochemical properties of flavins in aqueous solutions. *J. Electroanal. Chem. Interfacial Electrochem.* **156**, 105–127 (1983).

Muramatsu, H. *et al.* A new family of NAD(P)H-dependent oxidoreductases distinct from conventional Rossmann-fold proteins. *J. Biosci. Bioeng.* **99**, 541–547 (2005).

Zhou, J. *et al.* How sulphate-reducing microorganisms cope with stress: lessons from systems biology. *Nat. Rev. Microbiol.* **9**, 452–466 (2011).

Little, B. J. & Lee, J. S. *Microbiologically Influenced Corrosion*. (John Wiley & Sons, 2007).

Nealson, K. H. & Saffarini, D. Iron and manganese in anaerobic respiration: environmental significance, physiology, and regulation. *Annu. Rev. Microbiol.* **48**, 311–343 (1994).

Bonifay, V. *et al.* Metabolomic and Metagenomic Analysis of Two Crude Oil Production Pipelines Experiencing Differential Rates of Corrosion. *Front. Microbiol.* **8**, 99 (2017).

Mayhew, S. G. The effects of pH and semiquinone formation on the oxidation--reduction

potentials of flavin mononucleotide: a reappraisal. *Eur. J. Biochem.* **265**, 698–702 (1999).

Malinauskas, A., Ruzgas, T. & Gorton, L. Tuning the redox potential of riboflavin by zirconium phosphate in carbon paste electrodes. *Bioelectrochem. Bioenerg.* **49**, 21–27 (1999).

Thauer, R. K., Stackebrandt, E. & Hamilton, W. A. Energy metabolism and phylogenetic diversity of sulphate-reducing bacteria. *Sulphate-reducing bacteria: Environmental and engineered systems* 1–37 (2007).

Clark, M. E., Edelmann, R. E., Duley, M. L., Wall, J. D. & Fields, M. W. Biofilm formation in Desulfovibrio vulgaris Hildenborough is dependent upon protein filaments. *Environ. Microbiol.* **9**, 2844–2854 (2007).

Klonowska, A. *et al.* Hexavalent chromium reduction in Desulfovibrio vulgaris Hildenborough causes transitory inhibition of sulfate reduction and cell growth. *Appl. Microbiol. Biotechnol.* **78**, 1007–1016 (2008).

De León, K. B. *et al.* Unintended Laboratory-Driven Evolution Reveals Genetic Requirements for Biofilm Formation by Desulfovibrio vulgaris Hildenborough. *MBio* **8**, (2017).

Dinh, H. T. *et al.* Iron corrosion by novel anaerobic microorganisms. *Nature* **427**, 829–832 (2004).

Kato, S. Microbial extracellular electron transfer and its relevance to iron corrosion. *Microb. Biotechnol.* **9**, 141–148 (2016).

Busby, J. N., Panjikar, S., Landsberg, M. J., Hurst, M. R. H. & Lott, J. S. The BC component of ABC toxins is an RHS-repeat-containing protein encapsulation device. *Nature* **501**, 547–550 (2013).

Huan, T. *et al.* Systems biology guided by XCMS Online metabolomics. *Nat. Methods* **14**, 461–462 (2017).

Clark, M. E. *et al.* Transcriptomic and proteomic analyses of Desulfovibrio vulgaris biofilms: Carbon and energy flow contribute to the distinct biofilm growth state. *BMC Genomics* **13**, (2012).

Keller, K. L. & Wall, J. D. Genetics and Molecular Biology of the Electron Flow for Sulfate Respiration in Desulfovibrio. *Front. Microbiol.* **2**, (2011).

Enning, D. *et al.* Marine sulfate-reducing bacteria cause serious corrosion of iron under electroconductive biogenic mineral crust. *Environ. Microbiol.* **14**, 1772–1787 (2012).

Clark, M. E. *et al.* Temporal Transcriptomic Analysis as Desulfovibrio vulgaris Hildenborough Transitions into Stationary Phase during Electron Donor Depletion. *Appl. Environ. Microbiol.* **72**, 5578–5588 (2006).

Xu, D. & Gu, T. Carbon source starvation triggered more aggressive corrosion against carbon steel by the Desulfovibrio vulgaris biofilm. *Int. Biodeterior. Biodegradation* **91**, 74–81 (2014).

Zhang, P., Xu, D., Li, Y., Yang, K. & Gu, T. Electron mediators accelerate the microbiologically influenced corrosion of 304 stainless steel by the Desulfovibrio vulgaris biofilm. *Bioelectrochemistry* **101**, 14–21 (2015).

Chen, Y. *et al.* Long-term survival of Desulfovibrio vulgaris on carbon steel and associated pitting corrosion. *Corros. Sci.* doi:10.1016/j.corsci.2014.09.016

Hauser, L. J. *et al.* Complete Genome Sequence and Updated Annotation of Desulfovibrio alaskensis G20. *J. Bacteriol.* **193**, 4268–4269 (2011).

Smith, C. A., Want, E. J., O'Maille, G., Abagyan, R. & Siuzdak, G. XCMS: Processing Mass Spectrometry Data for Metabolite Profiling Using Nonlinear Peak Alignment, Matching, and Identification. *Anal. Chem.* **78**, 779–787 (2006).

Heidelberg, J. F. *et al.* The genome sequence of the anaerobic, sulfate-reducing bacterium Desulfovibrio vulgaris Hildenborough. *Nat. Biotechnol.* **22**, 554–559 (2004).

Ivanisevic, J. *et al.* Toward 'Omic Scale Metabolite Profiling: A Dual Separation–Mass Spectrometry Approach for Coverage of Lipid and Central Carbon Metabolism. *Anal. Chem.* **85**, 6876–6884 (2013).

Benton, H. P. *et al.* Autonomous Metabolomics for Rapid Metabolite Identification in Global Profiling. *Anal. Chem.* **87**, 884–891 (2015).

Li, H. *et al.* Extracellular Electron Transfer Is a Bottleneck in the Microbiologically Influenced Corrosion of C1018 Carbon Steel by the Biofilm of Sulfate-Reducing Bacterium Desulfovibrio vulgaris. *PLoS One* **10**, e0136183 (2015).

Enning, D. & Garrelfs, J. Corrosion of iron by sulfate-reducing bacteria: new views of an old problem. *Appl. Environ. Microbiol.* **80**, 1226–1236 (2014).

Venzlaff, H. *et al.* Accelerated cathodic reaction in microbial corrosion of iron due to direct electron uptake by sulfate-reducing bacteria. *Corros. Sci.* **66**, 88–96 (2013).

Montenegro-Burke, J. R. *et al.* Smartphone Analytics: Mobilizing the Lab into the Cloud for Omic-Scale Analyses. *Anal. Chem.* **88**, (2016).

# APPENDICES

# APPENDIX A

## SMARTPHONE ANALYTICS: MOBILIZING THE LAB INTO THE CLOUD FOR OMIC-SCALE ANALYSES

# APPENDIX A

## SMARTPHONE ANALYTICS: MOBILIZING THE LAB INTO THE CLOUD FOR OMIC-SCALE ANALYSES

### Contributions of Authors and Co-Authors

Manuscript in Appendix A

Author: J. Rafael Montenegro-Burke

Contributions: Experimental design, performed experiments, analyzed data, wrote and revised the manuscript.

Author: Thiery Phommavongsay

Contributions: Performed experiments, analyzed data.

Author: Aries E. Aisporna

Contributions: Performed experiments, analyzed data.

Author: Tao Huan

Contributions: Performed experiments, analyzed data.

Author: Duane Rinehart

Contributions: Performed experiments, analyzed data.

Author: Erica Forsberg

Contributions: Performed experiments, analyzed data.

Author: Farris L. Poole

Contributions: Performed experiments, analyzed data.

Author: Michael P Thorgersen

Contributions: Performed experiments, analyzed data.

Author: Michael W. W. Adams

Contributions: Performed experiments, analyzed data.

Author: **Gregory Krantz**

Contributions: Performed experiments, analyzed data.

Author: Matthew W. Fields

Contributions: Wrote and revised the manuscript.

Author: Trent R. Northen

Contributions: Wrote and revised the manuscript.

Author: Paul D. Robbins

Contributions: Wrote and revised the manuscript.

Author: Laura Niedernhofer

Contributions: Wrote and revised the manuscript.

Author: Luke Lairson

Contributions: Wrote and revised the manuscript.

Author: H. Paul Benton

Contributions: Wrote and revised the manuscript.

Author: Gary Suizdak

Contributions: Experimental design, analyzed data, wrote and revised the manuscript.

Manuscript Information

J. Rafael Montenegro-Burke, Thiery Phommavongsay, Aries E. Aisporna, Tao Huan, Duane Rinehart, Erica Forsberg, Farris L. Poole, Michael P Thorgersen, Michael W. W. Adams, Gregory Krantz, Matthew W. Fields, Trent R. Northen, Paul D. Robbins, Laura Niedernhofer, Luke Lairson, H. Paul Benton, Gary Suizdak

Analytical Chemistry
Status of Manuscript:
____ Prepared for submission to a peer-reviewed journal
____ Officially submitted to a peer-reviewed journal
____ Accepted by a peer-reviewed journal
__X__ Published in a peer-reviewed journal

ACS Publications
Published August 25, 2016
Nature Methods 14, 461-462 (2017)

analytical chemistry

Article

pubs.acs.org/ac

# Smartphone Analytics: Mobilizing the Lab into the Cloud for Omic-Scale Analyses

J. Rafael Montenegro-Burke,[†] Thiery Phommavongsay,[†] Aries E. Aisporna,[†] Tao Huan,[†] Duane Rinehart,[†] Erica Forsberg,[†] Farris L. Poole,[‡] Michael P. Thorgersen,[‡] Michael W. W. Adams,[‡] Gregory Krantz,[§] Matthew W. Fields,[§] Trent R. Northen,[∥] Paul D. Robbins,[⊥] Laura J. Niedernhofer,[⊥] Luke Lairson,[#] H. Paul Benton,[†] and Gary Siuzdak*[,†,⊥]

[†]Scripps Center for Metabolomics, [#]Department of Chemistry, and [⊥]Departments of Chemistry, Molecular, and Computational Biology, The Scripps Research Institute, 10550 North Torrey Pines Road, La Jolla, California 92037, United States

[‡]Department of Biochemistry and Molecular Biology, University of Georgia, Athens, Georgia 30602, United States

[§]Department of Microbiology and Immunology and Center for Biofilm Engineering, Montana State University, 109 Lewis Hall, Bozeman, Montana 59717, United States

[∥]Life Sciences Division, Lawrence Berkeley National Laboratory, 1 Cyclotron Road, Berkeley, California 94720, United States

[⊥]Departments of Metabolism and Aging, The Scripps Research Institute—Florida, Jupiter, Florida 33458, United States

Supporting Information

**ABSTRACT:** Active data screening is an integral part of many scientific activities, and mobile technologies have greatly facilitated this process by minimizing the reliance on large hardware instrumentation. In order to meet with the increasingly growing field of metabolomics and heavy workload of data processing, we designed the first remote metabolomic data screening platform for mobile devices. Two mobile applications (apps), XCMS Mobile and METLIN Mobile, facilitate access to XCMS and METLIN, which are the most important components in the computer-based XCMS Online platforms. These mobile apps allow for the visualization and analysis of metabolic data throughout the entire analytical process.

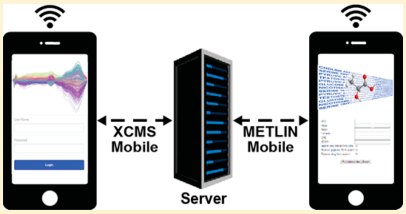


Specifically, XCMS Mobile and METLIN Mobile provide the capabilities for remote monitoring of data processing, real time notifications for the data processing, visualization and interactive analysis of processed data (e.g., cloud plots, principle component analysis, box-plots, extracted ion chromatograms, and hierarchical cluster analysis), and database searching for metabolite identification. These apps, available on Apple iOS and Google Android operating systems, allow for the migration of metabolomic research onto mobile devices for better accessibility beyond direct instrument operation. The utility of XCMS Mobile and METLIN Mobile functionalities was developed and is demonstrated here through the metabolomic LC-MS analyses of stem cells, colon cancer, aging, and bacterial metabolism.

Metabolomics has become a powerful technology for the comprehensive analysis of metabolites, identifying biomarkers and deciphering the mechanistic underpinnings of biological phenomena.[1] Among the different analytical platforms, MS-based metabolomics methodologies coupled to preionization separation techniques such as LC-MS and GC/MS are widely used due to their wide metabolome coverage.[2] Aside from advances in instrumentation, development in informatic resources for data processing and interpretation has significantly progressed in the past decade, increasing the productivity in many laboratories. Our metabolic data processing platform, XCMS,[3] has benefited from numerous updates and developments on the cloud based infrastructure of XCMS Online.[4,5]

XCMS Online enables the performance of metabolic feature picking, retention-time alignment, and data visualization for thousands of users entirely from one central hardware platform, housed at the Scripps Center for Metabolomics (La Jolla, CA). XCMS Online is regularly visited by ~500 IP address daily and performs ~60 jobs a day. One major advantage of XCMS Online is the centralization of resources, removing the need for redundant software and individual powerful computing capabilities. Additionally, taking metabolomic data into the cloud provides the advantage of sharing metabolomic data among XCMS Online users, making it readily available for publication. Another advantage of the Web-based platform is the integration of XCMS with METLIN,[6] a database of over 240,000 metabolites and 14,000 metabolites with high resolution MS/MS spectra in both positive and negative ion-

Received: July 13, 2016
Accepted: August 25, 2016
Published: August 25, 2016





DOI: 10.1021/acs.analchem.6b02676
Anal. Chem. 2016, 88, 9753−9758

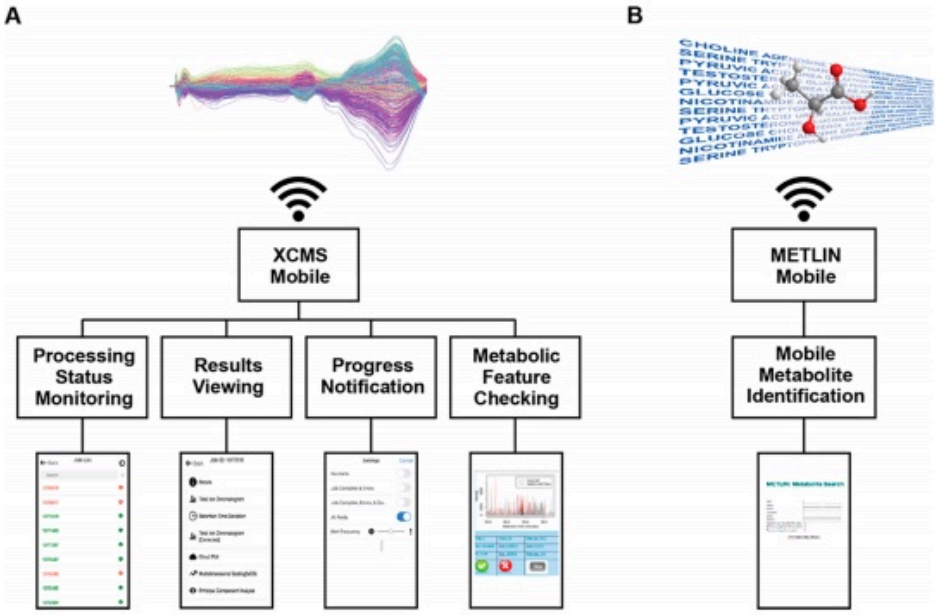


Figure 1. Flowchart and functions of XCMS Mobile (A) and METLIN Mobile (B) applications.

mode at 4 different collision energies, which facilitates the metabolite identification to around 11,000 users.[7]

One major disadvantage of most bioinformatic tools is their typical limitation to personal computers (PCs) usage, and once outside of the laboratory, data and instrument access is typically limited to a Virtual Private Network (VPN) based connection. Furthermore, in the past few decades, research has become more data-intensive and specialized equipment is often shared between different groups. These changes have not only caused an increase in the amount of time necessary for analysis but also instrument access can be limited to only nontraditional working hours.[8] Mobile devices, particularly smartphones, offer the advantage of accessibility to a wide range of operations and functionalities at relatively economic prices. Moreover, the use of smartphones has widely spread across the United States to 185 million devices.[9] In addition, frequent personal use of these devices has been reported to around 85 ± 55 times per day.[10] To take advantage of the rapidly evolving mobile hardware and software technologies, we have developed two mobile apps: XCMS Mobile and METLIN Mobile to facilitate data monitoring beyond the laboratory. XCMS Mobile allows for monitoring, controlling data processing, and analysis in the cloud from common cellular devices using iOS and Android operating systems (OS) such as Apple and Android devices, respectively. METLIN Mobile auto select Web design (beta version) allows metabolite identification using the METLIN metabolite database. These apps allow XCMS users to make progress in the metabolomics study workflow independently of the location through hand-held mobile devices. The two mobile apps are now available from app stores linked via https://xcmsonline.scripps.edu/. Depending on the type of the mobile device (Apple or Android), XCMS Mobile can also be directly installed from App Store or Google Play; METLIN Mobile can be accessed via https://metlin.scripps.edu using Firefox or Chrome Web browsers.

Herein, we describe the functionalities of XCMS Mobile and METLIN Mobile presented in the context of microbial biofilms metabolic influence on colon tissue and cancer occurrence in a LC-MS based metabolomics study.[11] The functions available in these platforms are processing status monitoring, results viewing, progress notification metabolic feature checking, and metabolite identification (Figure 1). Our integration of mobile apps with metabolomics study shows considerable benefits, including high accessibility and mobility without compromising user-friendliness, resulting in improved research productivity.

## EXPERIMENTAL SECTION

**Development of XCMS Mobile and METLIN Mobile Applications.** XCMS Mobile and METLIN Mobile were developed using the programming languages JavaScript, HTML5, and CSS3 and the mobile framework jQuery Mobile to be compatible across Android and iPhone platforms. The platforms iPhone/iPhone 3G, iPhone 3GS, and newer (Apple Inc., Cupertino, CA) as well as Android 1.0−4.4 (Google Inc., Mountain View, CA) are all supported in the current version. Backend database management and functionality of the mobile application was developed using a REST API provided by the DreamFactory REST framework. The client side of the application was developed to make calls to the REST API, which returns data back in JSON format. This data was



DOI: 10.1021/acs.analchem.6b02676
Anal. Chem. 2016, 88, 9753−9758

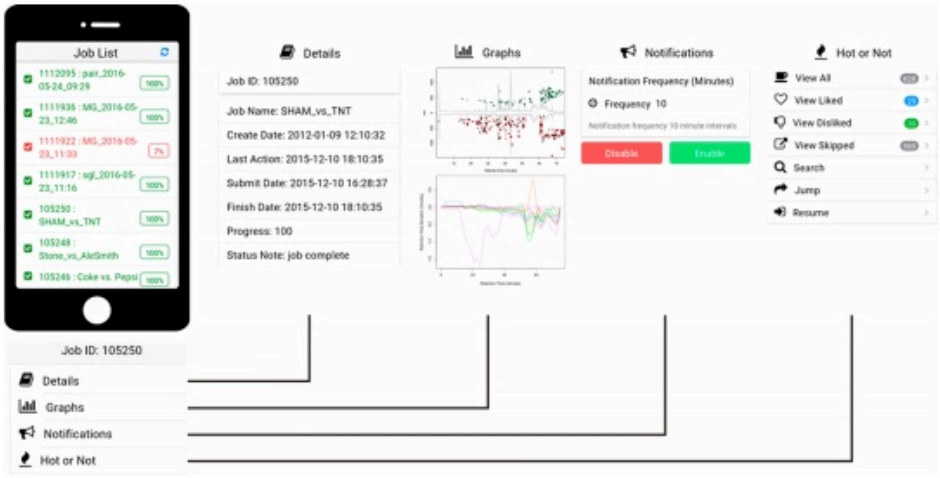


**Figure 2.** XCMS Mobile menu and visualization functions. "Job List" displays all jobs submitted to XCMS online with their respective progress. In "Details", further information regarding each job can be accessed. Data analysis visualization graphs such as cloud plots are available under "Graphs". "Notification" settings can be enabled and set to different frequencies. Lastly, "Hot or Not" displays EIC of the different metabolic features allowing the user to mark features of interest for further analysis.

manipulated using JavaScript, to allow for user-friendly visualization and interaction with the data. jQuery Mobile framework and CSS3 were used in the creation of the front end look and feel of the mobile apps.

**Sample Preparation and LC-MS Analysis.** Samples were analyzed by reverse-phase liquid chromatography-quadrupole time-of-flight mass spectrometry (RPLC-QTOF) as previously described.[11,12] Full data sets are available as a public shares on XCMS Online.

**Data Streaming with XCMS Mobile and METLIN Mobile.** Data streaming strategy[13] was applied to upload LC-MS data onto XCMS Online upon acquisition completion. Data processing was actively monitored using an iPhone 6 (Apple Inc., Cupertino, CA) with XCMS Mobile and METLIN Mobile installed. Notification frequency was set to a default of 10 min.

## WORKFLOW

**XCMS Mobile.** XCMS Mobile allows for remote monitoring and interpretation of the metabolomic data processed on XCMS Online. The current version of XCMS Mobile has four modules (Figure 1A): data processing status monitoring, progress notification, results viewing, and metabolic feature checking. Examples of these 4 modules with their respective tabs are shown in Figure 2.

**Data Processing Status Monitoring.** The data processing status monitoring function allows for the tracking of the processing status of the submitted jobs to XCMS Online on mobile devices. An overview of all the job status submitted or an in-depth view of individual job status is available in this function. The overview of all the job status is presented on the home page upon user log in to XCMS Mobile using the user corresponding XCMS Online login information. On the overview page, each job listed has a unique job ID, job name, and progress indicator. The data processing progress is displayed by a percentage value overlaid on a blue progress box indicating that the data processing steps are in progress. While a green progress box indicates completion of the data processing steps. On the other hand, a red progress bar indicates an error during data processing steps. Further detailed job status information, such as submission date, completion date, status note, log (errors), and warnings can be accessed under the "Details" tab.

**Results Viewing.** The results viewing function can be accessed under the "Graphs" tab, and it allows for a quick graphical glance of the processed metabolomic data. These data visualization graphs have the capabilities of providing relevant information about the performance of the analysis and the quality of the data before advancing onto more detailed data interpretation. Currently, the data visualization graphs include the original TIC of all the samples, retention time deviation plots, nonmetric multidimensional scaling, PCA score plots, box-plots, and cloud plots.

**Progress Notification.** Progress notification, an important function in XCMS Mobile, is accessed through the "Notifications" tab and allows the remote monitoring of ongoing data processing by notifications in mobile devices. These notifications can be activated and deactivated by the user, and the display rate of the current data processing progress can be set at a user defined frequency (e.g., 10 min).

**Metabolic Feature Checking.** Metabolic feature checking in XCMS Mobile allows the user to manually confirm the metabolic features that will be used for further identification and interpretation through a binary selection system found under the "Hot or Not" tab. Usually, such metabolic feature checking is a time-consuming process, taking researchers hours to days in front of the computer examining metabolic features. On the contrary, the mobile metabolic feature checking



DOI: 10.1021/acs.analchem.6b02676
Anal. Chem. 2016, 88, 9753−9758

function allows users to inspect and filter metabolic features on hand-held devices independently of the location. After examining each extracted ion chromatogram (EIC) of individual metabolic features presented on the screen of the mobile device, the different features can be selected or discarded by "swiping" right or left, respectively (Figure 3).

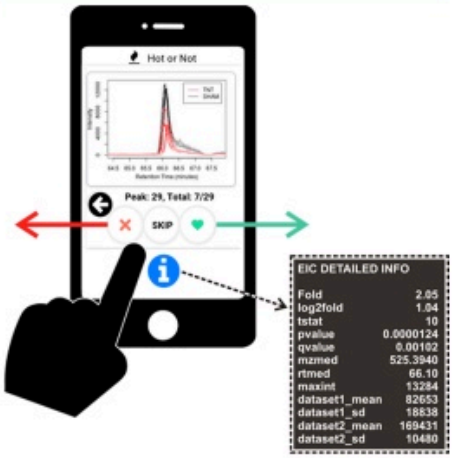


**Figure 3.** Metabolic feature checking (Hot or Not). Individual features EIC can be analyzed and marked for future analysis by swiping to the right (green arrow) or by pressing the green button. Conversely, uninteresting features can be swiped to the left (red arrow) or by pressing the red button. The blue "i" button displays information about each feature such as fold change, $m/z$, retention time, etc.

Additionally, other metabolic information, such as fold change, $m/z$, and retention time to name a few, can be displayed by pressing the blue "i" button. Lastly, upon metabolic feature checking the results are sent to the cloud-based XCMS Online server, providing subsequent PC accessibility.

**METLIN Mobile.** METLIN Mobile (beta version) is an auto select Web design, which provides rapid and accessible metabolite identification and information using mobile devices (Figure 1B). In its current version, METLIN Mobile allows users to perform simple and advanced metabolite searches (Figures S1 and S2, respectively) based on single or multiple metabolic searching criteria such as METLIN ID (MID), molecular mass, $m/z$, metabolite name, chemical formula, and CAS or KEGG number. Furthermore, fragmentation data (MS/MS) can be accessed, both directly and indirectly through metabolite name and links in the search results, respectively (Figures S3 and S4). It is worth mentioning that the search graphical user interface is optimized so that all information can be easily displayed on the mobile device, minimizing the necessary screen manipulation and is currently being beta tested in an ongoing aging study (Figure 4).

**Applications.** To demonstrate the performance of XCMS Mobile and METLIN Mobile through the data analysis workflow, a LC-MS metabolomic study comparing the metabolomic differences between paired colon cancer tissues and normal tissues in association with microbial biofilms from 30 individuals was selected. During the data processing, progress notifications every 10 min were received over the entire data processing time of 24 h. Subsequently, results were examined on the mobile device, with TIC, PCA, and other plots highlighting their differences. 150 metabolic features were statistically significant ($p < 0.01$) with fold changes in the range of >1.5 or <0.67. Metabolic feature checking was performed on XCMS Mobile, where 135 metabolic features were correctly extracted by XCMS. Finally, METLIN Mobile was used to putatively identify these 135 metabolites by mass matching against METLIN with a mass tolerance of 5 ppm. Among them, 80 metabolic features got positive putative identifications, available for further validation and interpretation.

In this work, we described the functionalities of two developed mobile apps, XCMS Mobile and METLIN Mobile, to actively and remotely screen and interpret metabolomic data as well as perform metabolite identification. The current version of XCMS Mobile provides four important modules (Figure 1): processing status monitoring, progress notification, results viewing, and metabolic feature checking. Additionally, METLIN Mobile provides one module, remote metabolite identification by accessing METLIN database information. Compared to conventional metabolomic bioinformatic tools,[14,15] which are typically restricted to be used on PCs, XCMS Mobile and METLIN Mobile are designed to access and display metabolomic data from mobile devices in the cloud, improving researchers' productivity. Regardless of conventional metabolomic tools designed to implement more comprehensive functions, the functions provided by the mobile apps are more suitable for quick and convenient data screening and data visualization, particularly outside laboratory settings. Most importantly, these two mobile apps are designed for the robust and widely used metabolomic platform: XCMS Online server and METLIN spectra library platform, which will benefit over 10,000 metabolomics researchers worldwide.

The different functions available for these mobile apps for metabolomics studies were exemplified using a colon cancer study. Overall, three major advantages are clearly determined in terms of improving research productivity by using XCMS Mobile and METLIN Mobile. First, data processing can be monitored remotely and independently from the location. Considering the automatic data processing of 60 individual samples on XCMS Online took 24 h, the processing status monitoring and progress notification function allows for the supervision of data processing status remotely with fast response capability while performing other tasks. For example, upon a progress error notification during data processing, we immediately were able to correct the error and continue to process, minimizing delays in the study. Second, following data processing completion notification, processed data can be visualized in graphs, such as TIC, retention time correction, PCA, cloud plot to name a few, and provide an assessment of instrumental performance as well as differences in metabolic signatures between the different sample groups. These preliminary results allowed for the planning of follow-up experiments for validation and quantitation in advance. Third, data interpretation and metabolite identification can be performed under more flexible time conditions away from the laboratory or office PC. In this particular work, the manual feature confirmation of 150 metabolic features and metabolite identification was performed remotely during nontraditional working hours. It is worth mentioning that for this metabolic study only about 20 min of regular office hours were used over



DOI: 10.1021/acs.analchem.6b02676
Anal. Chem. 2016, 88, 9753−9758

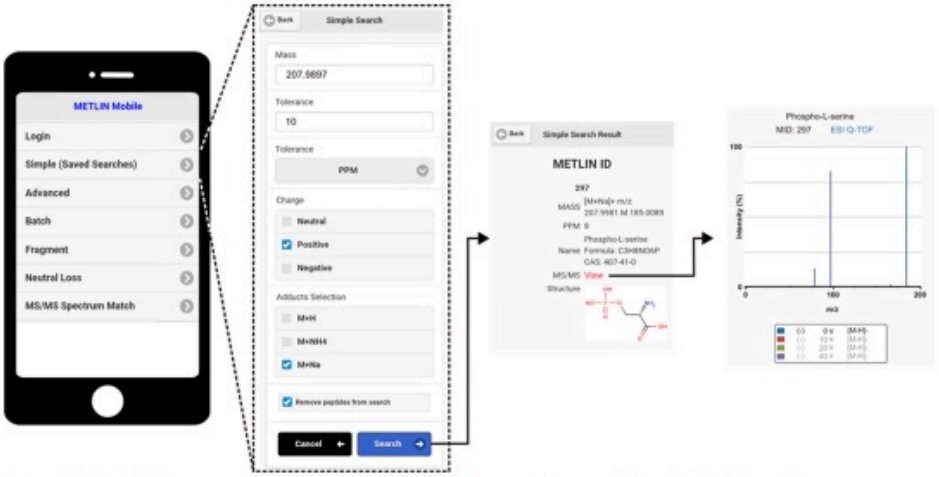


Figure 4. METLIN Mobile provides access to the METLIN database and allows for different search types. In "Simple Search", a particular $m/z$ value, in this case 207.9897 found to be dysregulated in an ongoing aging study, can be searched for matches with several filter options such as mass tolerance, charge, adducts, and type of molecules. The matching metabolites are displayed in "Results", where information such as molecular formula and structure are shown for the pertaining compound.

a 3 day period without accounting for data acquisition. This demonstrates the potential of taking the lab into the cloud and pursuing several metabolomic studies simultaneously.

## CONCLUSION

In summary, we have developed two mobile apps, XCMS Mobile and METLIN Mobile, with the goal of reducing the reliance on personal computers for metabolomic data monitoring and interpretation. Each application was designed to improve research productivity and minimize resources for remote data processing. We demonstrated the advantage and capabilities of using mobile apps in metabolomics on typical metabolomic studies including colon cancer, aging, and bacterial metabolism. To the best of our knowledge, XCMS Mobile and METLIN Mobile are the first mobile apps in the field of metabolomics, and we expect the use of mobile apps in metabolomics could be implemented to other bioinformatic tools, streamlining data analysis by providing greater flexibility to metabolomics researchers. We believe that these mobile applications will greatly increase the accessibility of metabolomics data analysis, enabling students around the world to gain first-hand experience analyzing metabolomic data.

## ASSOCIATED CONTENT

### Supporting Information

The Supporting Information is available free of charge on the ACS Publications website at DOI: 10.1021/acs.analchem.6b02676.

Supplemental Figures 1−4 (PDF)

## AUTHOR INFORMATION

### Corresponding Author

*Phone: 858-784-9415. E-mail: siuzdak@scripps.edu.

### Author Contributions

J.R.M.-B. and T.P. contributed equally.

### Notes

The authors declare no competing financial interest.

## ACKNOWLEDGMENTS

The authors thank the following for funding assistance: Ecosystems and Networks Integrated with Genes and Molecular Assemblies (http://enigma.lbl.gov), a Scientific Focus Area Program at Lawrence Berkeley National Laboratory for the U.S. Department of Energy, Office of Science, Office of Biological and Environmental Research under contract number DE-AC02-05CH11231, and the National Institutes of Health (NIH) grants R01 GMH4368 and PO1 A1043376-02S1.

## REFERENCES

(1) Patti, G. J.; Yanes, O.; Siuzdak, G. *Nat. Rev. Mol. Cell Biol.* **2012**, *13*, 263−269.
(2) Dunn, W. B.; Ellis, D. I. *TrAC, Trends Anal. Chem.* **2005**, *24*, 285−294.
(3) Smith, C. A.; Want, E. J.; O'Maille, G.; Abagyan, R.; Siuzdak, G. *Anal. Chem.* **2006**, *78*, 779−787.
(4) Tautenhahn, R.; Patti, G. J.; Rinehart, D.; Siuzdak, G. *Anal. Chem.* **2012**, *84*, 5035−5039.
(5) Gowda, H.; Ivanisevic, J.; Johnson, C. H.; Kurczy, M. E.; Benton, H. P.; Rinehart, D.; Nguyen, T.; Ray, J.; Kuehl, J.; Arevalo, B.; Westenskow, P. D.; Wang, J.; Arkin, A. P.; Deutschbauer, A. M.; Patti, G. J.; Siuzdak, G. *Anal. Chem.* **2014**, *86*, 6931−6939.
(6) Smith, C. A.; O'Maille, G.; Want, E. J.; Qin, C.; Trauger, S. A.; Brandon, T. R.; Custodio, D. E.; Abagyan, R.; Siuzdak, G. *Ther. Drug Monit.* **2005**, *27*, 747−751.
(7) Kurczy, M. E.; Ivanisevic, J.; Johnson, C. H.; Uritboonthai, W.; Hoang, L.; Fang, M.; Hicks, M.; Aldebot, A.; Rinehart, D.; Mellander, L. J.; Tautenhahn, R.; Patti, G. J.; Spilker, M. E.; Benton, H. P.; Siuzdak, G. *Bioinformatics* **2015**, *31*, 3721−3724.
(8) Schiermeier, Q. *Nature* **2012**, *492*, 299−300.



DOI: 10.1021/acs.analchem.6b02676
Anal. Chem. 2016, 88, 9753−9758

(9) Eadicicco, L. Americans Check Their Phones 8 Billion Times a Day. In *Time*: New York, New York, Dec 15, 2015.
(10) Andrews, S.; Ellis, D. A.; Shaw, H.; Piwek, L. *PLoS One* **2015**, *10*, e0139004.
(11) Johnson, C. H.; Dejea, C. M.; Edler, D.; Hoang, L. T.; Santidrian, A. F.; Felding, B. H.; Ivanisevic, J.; Cho, K.; Wick, E. C.; Hechenbleikner, E. M.; Uritboonthai, W.; Goetz, L.; Casero, R. A., Jr.; Pardoll, D. M.; White, J. R.; Patti, G. J.; Sears, C. L.; Siuzdak, G. *Cell Metab.* **2015**, *21*, 891−897.
(12) Ivanisevic, J.; Zhu, Z.-J.; Plate, L.; Tautenhahn, R.; Chen, S.; O'Brien, P. J.; Johnson, C. H.; Marletta, M. A.; Patti, G. J.; Siuzdak, G. *Anal. Chem.* **2013**, *85*, 6876−6884.
(13) Rinehart, D.; Johnson, C. H.; Nguyen, T.; Ivanisevic, J.; Benton, H. P.; Lloyd, J.; Arkin, A. P.; Deutschbauer, A. M.; Patti, G. J.; Siuzdak, G. *Nat. Biotechnol.* **2014**, *32*, 524−527.
(14) Pluskal, T.; Castillo, S.; Villar-Briones, A.; Orešič, M. *BMC Bioinf.* **2010**, *11*, 395.
(15) Xia, J.; Sinelnikov, I. V.; Han, B.; Wishart, D. S. *Nucleic Acids Res.* **2015**, *43*, W251−w257.

# APPENDIX B

## SYSTEMS BIOLOGY GUIDED BY XCMS ONLINE METABOLOMICS

# APPENDIX B

## SYSTEMS BIOLOGY GUIDED BY XCMS ONLINE METABOLOMICS

### Contributions of Authors and Co-Authors

Manuscript in Appendix A

Author: Tao Huan

Contributions: Experimental design, performed experiments, analyzed data, wrote and revised the manuscript.

Author: Erika M. Forsberg

Contributions: Experimental design, performed experiments, analyzed data, wrote and revised the manuscript.

Author: Duane Rinehart

Contributions: Performed experiments, analyzed data.

Author: Caroline H. Johnson

Contributions: Performed experiments, analyzed data.

Author: Julijana Ivanisevic

Contributions: Performed experiments, analyzed data.

Author: H. Paul Benton

Contributions: Performed experiments, analyzed data.

Author: Mingliang Fang

Contributions: Performed experiments, analyzed data.

Author: Aries Aisporna

Contributions: Performed experiments, analyzed data.

Author: Brian Hilmers

Contributions: Performed experiments, analyzed data.

Author: Farris L. Poole

Contributions: Performed experiments, analyzed data.

Author: Michael P Thorgersen

Contributions: Performed experiments, analyzed data.

Author: Michael W. W. Adams

Contributions: Performed experiments, analyzed data.

Author: **Gregory Krantz**

Contributions: Performed experiments, analyzed data.

Author: Erica L. Majumder

Contributions: Performed experiments, analyzed data.

Author: Judy D. Wall

Contributions: Performed experiments, analyzed data.

Author: Matthew W. Fields

Contributions: Experimental design, analyzed data, wrote and revised the manuscript.

Author: Paul D. Robbins

Contributions: Experimental design, analyzed data, wrote and revised the manuscript.

Author: Laura J. Niedernhofer

Contributions: Experimental design, analyzed data, wrote and revised the manuscript.

Author: Trey Ideker

Contributions: Experimental design, analyzed data, wrote and revised the manuscript.

Author: Nicholas J. W. Rattray

Contributions: Experimental design, analyzed data, wrote and revised the manuscript.

Author: Royston Goodacre

Contributions: Experimental design, analyzed data, wrote and revised the manuscript.

Author: Luke L. Lairson

Contributions: Experimental design, analyzed data, wrote and revised the manuscript.

Author: Gary Suizdak

Contributions: Experimental design, analyzed data, wrote and revised the manuscript.

Manuscript Information

Tao Huan, Erika M. Forsberg, Duane Rinehart, Caroline H. Johnson, Julijana Ivanisevic, H. Paul Benton, Mingliang Fang, Aries Aisporna, Brian Hilmers, Farris L. Poole, Michael P Thorgersen, Michael W. W. Adams, Gregory Krantz**,** Matthew W. Fields, Paul D. Robbins, Laura J. Niedernhofer, Trey Ideker, Erica L. Majumder, Judy D. Wall, Nicholas J. W. Rattray, Royston Goodacre, Luke L. Lairson, Gary Suizdak

Nature Methods
Status of Manuscript:
____ Prepared for submission to a peer-reviewed journal
____ Officially submitted to a peer-reviewed journal
____ Accepted by a peer-reviewed journal
__X__ Published in a peer-reviewed journal

Springer Nature
Published April 27, 2017
Nature Methods 14, 461-462 (2017)

## Systems biology guided by XCMS Online metabolomics

**To the Editor:** An aim of systems biology is to understand complex interactions between genes, proteins and metabolites by integrating and modeling multiple data sources. We report an 'integrated-omics' approach within XCMS Online[1] that automatically superimposes raw metabolomic data onto metabolic pathways and integrates it with transcriptomic and proteomic data (http://XCMSOnline.scripps.edu/).

Mapping downstream metabolite changes onto metabolic pathways and biological networks can provide considerable mechanistic insight that can be confirmed by association to multi-omic data. However, pathway analysis using untargeted metabolomics requires intense data curation, including feature filtering, statistical analysis and metabolite identification. Subjectively defined values such as fold change, *P* value and signal intensity cut-off are needed to identify significantly dysregulated metabolite features within enormous data sets. Confirming metabolite identities for pathway analysis typically requires performing additional tandem mass spectrometry (MS/MS) experiments and matching the spectra to standards or MS/MS spectral databases. The magnitude of these data sets makes it impractical to manually interpret, and therefore the use of bioinformatic tools at each step is essential. Multiple analysis platforms are often needed to complete the entire workflow, which can take several weeks, depending on the size of the sample cohort and the experience of the analyst.

XCMS was originally developed as a metabolomics data processing algorithm to extract metabolic features from raw MS data and perform statistical analysis. The evolution of XCMS from a command line tool[2] to an intuitive cloud-based online platform[1] facilitated its use by a broader community. However, the community is still in need of user-friendly tools to take metabolomic output and associate it with metabolic pathways to identify aberrant biological processes. To address this demand, we implemented automated predictive pathway analysis[3], operating directly on the entire metabolic feature table, into the XCMS Online workflow (**Fig. 1**), removing the need to transfer data to another application and enabling quick and efficient pathway analysis. This process involves uploading raw MS data to XCMS Online, where the statistically significant features are identified; then, using Fisher's exact test, dysregulated metabolic pathways are identified from the processed accurate mass data[3]. If gene and protein data are available, they are uploaded and overlaid with the results of the metabolomic analysis. Currently there are over 7,600 metabolic models available for pathway analysis from BioCyc[4] v19.5–20.0, with contents being updated regularly. Further confirmation of dysregulated pathways can be performed by comparing metabolite spectra, obtained via targeted or autonomous MS/MS, with standard fragmentation spectra from METLIN, which contains MS/MS data on over 14,000 molecules[5]. To address instances in which a standard spectrum is not available, we have also recently added machine learning *in silico* fragmentation data to METLIN, generating MS/MS spectra on over 220,000 more molecules. Our workflow enables (i) evaluation of biochemical relevance by mapping

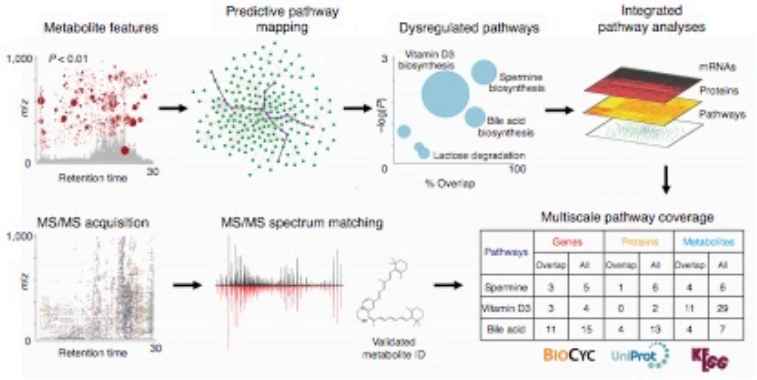


**Figure 1** | Workflow for metabolomic data and pathway analysis using XCMS Online. A metabolite feature table of statistically significant features is generated from standard XCMS processing; these features automatically undergo predictive pathway mapping using a specified biological model. The pathway cloud plot shows dysregulated pathways (blue circles) with increasing statistical significance on the *y* axis, metabolite overlap on the *x* axis and total number of metabolites in the pathway represented by the circle radius. The multiscale pathway coverage table presents enriched metabolic pathways with overlapped and total metabolites, genes and proteins. MS/MS data confirm dysregulated pathways by matching metabolite MS/MS spectra with the METLIN database.

high resolution MS data directly onto pathways, (ii) cross-integration of genomic and proteomic data and (iii) metabolite identity verification via data-dependent MS/MS analysis, either separately or as part of the autonomous workflow[5].

Our multi-omic analysis tool uses embedded BioCyc[6] and Uniprot[6] databases to map user-uploaded gene and protein data onto the predicted metabolic pathways (**Supplementary Fig. 1**). Results can be viewed in table form or using the interactive Pathway Cloud plot (**Fig. 1**). Dysregulated pathways with greater percent overlap and statistical significance appear in the upper right of the cloud plot. Graph features can be clicked to view more information on overlapping gene, protein and metabolite data, with links to BioCyc, KEGG and METLIN. Important features can be readily identified, helping to decipher underlying biological mechanisms. Details on the pathway analysis and integrated omics workflow can be found in the **Supplementary Methods**. Data sharing is possible between collaborators and the public, and we encourage users to share their data in the XCMS Online community.

To demonstrate metabolic pathway analysis and multi-omic integration, we describe representative sample sets in the **Supplementary Note**, including metabolic pathway analysis using progenitor cell proliferation data and a bacterially induced corrosion study (**Supplementary Fig. 2**); proteomic integration with an aging study (**Supplementary Fig. 3**); transcriptomic and proteomic integration using a human colon cancer study (**Supplementary Fig. 4** and **Supplementary Table 1**); a nitrate stress response study in sulfate-reducing bacteria (**Supplementary Fig. 5**) and a media stress response study in *Escherichia coli* (**Supplementary Fig. 6** and **Supplementary Table 2**); and a cohort of 1,600 diabetes plasma samples (**Supplementary Fig. 7**), which helps illustrate the scalability of the cloud-based XCMS Online.

Other notable tools providing pathway analysis and multi-omic integration include Galaxy-M[7], Open MS from KNIME[8] and MetaboAnalyst[9]. However, many of these tools still require separate preprocessing of tandem liquid chromatography—mass spectrometry data and are not fully integrated into a single program. Our workflow automatically maps metabolomic data directly onto pathways and integrates transcriptomics and proteomics for systems-wide interpretation in one cohesive platform. Additionally, metabolic network mapping is available based on the predictive activity network algorithm[3] for analysis of metabolomic data only, with multi-omics networking in development. In the future, we will incorporate unique metabolic pathways and networks from other sources to provide more comprehensive biological resources.

**Data availability.** To assist users with the workflow, we have provided a sample data set entitled "Ecoli_glucose-vs-adenosine" (Job ID #1133019) that can be found on XCMS Online under XCMS Public (https://xcmsonline.scripps.edu/landing_page.php?pgcontent=listPublicShares), as well as two instructional videos available on the XCMS Institute website (https://xcmsonline.scripps.edu/landing_page.php?pgcontent=institute) under the Omics tab and by clicking Integrated Omics or Pathway Cloud Plot.

ACKNOWLEDGMENTS

The authors thank J. Nazroo, G. Tampubolon, N. Pendleton and F.C.W. Wu from the University of Manchester for constructive discussions alongside Medical Research Council grant MRC G1001375/1 (R.G.) for generous funding. The authors thank the following for funding assistance: Ecosystems and Networks Integrated with Genes and Molecular Assemblies (ENIGMA), a Scientific Focus Area Program at Lawrence Berkeley National Laboratory for the US Department of Energy, Office of Science, Office of Biological and Environmental Research under contract number DE-AC02-05CH11231 (G.S.); and National Institutes of Health grants R01 GMH4368 (G.S.) and P01 A1043376-02S1 (G.S.).

*Note: Any Supplementary Information and Source Data files are available in the online version of the paper.*

AUTHOR CONTRIBUTIONS

T.H., E.M.F., D.R., H.P.B., A.A., B.H., T.I., M.W.W.A., P.D.R., L.J.N., M.W.F. and G.S. contributed to multi-omic platform design and development; T.H., E.M.F., C.H.J., M.F., G.K., M.P.T., L.L.L., F.L.P. E.L.M., J.D.W., N.J.W.R. and R.G. contributed to data collection and analysis. T.H. and E.M.F. share first authorship. C.H.J., J.I., T.I., and G.S. also contributed to manuscript writing.

COMPETING FINANCIAL INTERESTS

The authors declare no competing financial interests.

**Tao Huan[1,13], Erica M Forsberg[1,13], Duane Rinehart[1], Caroline H Johnson[1,2], Julijana Ivanisevic[3], H Paul Benton[1], Mingliang Fang[1,4], Aries Aisporna[1], Brian Hilmers[1], Farris L Poole[5], Michael P Thorgersen[5], Michael W W Adams[5], Gregory Krantz[6], Matthew W Fields[6], Paul D Robbins[7], Laura J Niedernhofer[7], Trey Ideker[8], Erica L Majumder[9], Judy D Wall[9], Nicholas J W Rattray[2,10], Royston Goodacre[10], Luke L Lairson[11] & Gary Siuzdak[1,11,12]**

[1]Scripps Center for Metabolomics, The Scripps Research Institute, La Jolla, California, USA. [2]Yale School of Public Health, Yale University, New Haven, Connecticut, USA. [3]Metabolomics Platform, Faculty of Biology and Medicine, University of Lausanne, Lausanne, Switzerland. [4]School of Civil and Environmental Engineering, Nanyang Technological University, Singapore. [5]Department of Biochemistry and Molecular Biology, University of Georgia, Athens, Georgia, USA. [6]Department of Microbiology and Immunology and Center for Biofilm Engineering, Montana State University, Montana State University, Bozeman, Montana, USA. [7]Departments of Metabolism and Aging, The Scripps Research Institute-Florida, Jupiter, Florida, USA. [8]Department of Medicine, University of California San Diego, La Jolla, California, USA. [9]Department of Biochemistry, University of Missouri, Columbia, Missouri, USA. [10]Manchester Institute of Biotechnology, School of Chemistry, The University of Manchester, Manchester, UK. [11]Department of Chemistry, The Scripps Research Institute, La Jolla, California, USA. [12]Departments of Molecular and Computational Biology, The Scripps Research Institute, La Jolla, California, USA. [13]These authors contributed equally to this work.
e-mail: siuzdak@scripps.edu

1. Gowda, H. *et al. Anal. Chem.* **86**, 6931–6939 (2014).
2. Smith, C.A., Want, E.J., O'Maille, G., Abagyan, R. & Siuzdak, G. *Anal. Chem.* **78**, 779–787 (2006).
3. Li, S.Z. *et al. PLoS Comput. Biol.* **9**, 7 (2013).
4. Caspi, R. *et al. Nucleic Acids Res.* **42**, D459–D471 (2014).
5. Benton, H.P. *et al. Anal. Chem.* **87**, 884–891 (2015).
6. The UniProt Consortium. *Nucleic Acids Res.* **43**, D204–D212 (2015).
7. Davidson, R.L., Weber, R.J.M., Liu, H.Y., Sharma-Oates, A. & Viant, M.R. *Gigascience* **5**, 10 (2016).
8. Aiche, S. *et al. Proteomics* **15**, 1443–1447 (2015).
9. Xia, J., Sinelnikov, I.V., Han, B. & Wishart, D.S. *Nucleic Acids Res.* **43**, W251–W257 (2015).

## Addressing reproducibility in single-laboratory phenotyping experiments

**To the Editor:** Phenotyping genetically engineered mouse lines has become a central strategy for discovering mammalian gene function. The International Mouse Phenotyping Consortium (IMPC) coordinates a large-scale community effort for phenotyping thousands of mutant lines[1], making data accessible in public databases[2] and distributing novel mutant lines as animal models of human diseases. The utility of any findings, however, critically depends on whether

# APPENDIX C

## METABOLOMIC COMPARISON OF NUTRITIONALLY LIMITED GROWTH IN *DESULFOVIBRIO ALASKENSIS* G20 AND *DESULFOVIBRIO VULGARIS* HILDENBOROUGH

## Introduction

Bacteria must adapt to changing environmental conditions, as alterations to factors such nutrient concentrations occur commonly, and acclimation is required for survival. When resources are available at ratios that are less than ideal, the cells must use the limiting nutrient efficiently. Such conditions were explored in Chapter 1 with *Desulfovibrio alaskensis* G20 growing under electron acceptor limiting (EAL) and electron donor limiting (EDL) conditions on a 1018 carbon steel surface. A metabolomic dataset was generated comparing these two conditions and a systems biology analysis of it was performed in the publication "Systems biology guided by XCMS Online metabolomics" shown in Appendix B. This data will be included in a manuscript from Franco et al. (unpublished) that contains data from a metabolomic study of altering nutrient limitation in *Desulfovibrio vulgaris* Hildenborough. Appendix C is a comparison of those two metabolomic datasets.

## Materials and Methods

### Biofilm growth

Biofilm samples were grown in CDC biofilm reactors (Biosurface Technologies Corp., Bozeman, MT, USA) with the headspace sparged with anoxic N2 gas (run through an oxygen-scrubber). Separate reactors were used to cultivate G20 biofilms on 1018 carbon steel coupons under each limiting nutrient condition. The coupons were not polished and supplied by Biosurface Technologies Corp. Reactors were inoculated with 40 ml of an exponential-phase culture and allowed to grow in batch mode for 24 h. The

medium pump flow rate was set to 0.3 ml min1 (D = 0.05 $h^{-1}$) 24 h post-inoculation and continuous flow was maintained until final samples were harvested. The dilution rate was chosen because the influent growth medium did not contain additional reducing agent as previously reported (Clark et al. 2006, 2012) and in situ growth rates are typically slower. The starting pH of medium was ~7.2 and during growth was 7.6–7.8. Modifications to the original recipe included adjusting the lactate and sulfate concentrations to 50 mM lactate:15 mM sulfate for EAL conditions and 15 mM lactate:15 mM sulfate for EDL conditions. The metal coupon dimensions were 7.6 x 1.5 x 0.1 cm. Modified coupon holders were used as previously described to provide increased material surface area (Clark et al. 2012). Experiments done in DvH were comparing an EAL condition (50 mM lactate: 10 mM sulfate) to a balanced (BAL) (60 mM lactate: 30mM sulfate) condition.

Metabolomics and data processing

At 192 h, biofilm coupons (EAL and EDL on 1018 CS) were dipped in degassed dH2O and the biofilm biomass scraped into a sterile microcentrifuge tube with degassed dH2O (4 °C). The tubes were centrifuged at 10,000 rpm for 5 min at 4 °C. The supernatant was removed and the cell pellet frozen with liquid $N_2$ and stored at 80 °C. Samples were processed and data analyzed as previously described (Ivanisevic et al. 2013; Benton et al. 2015; Montenegro-Burke et al. 2016; Huan et al. 2017).

## Results

The experiment in DvH done by Franco et al. involved comparing metabolite abundance in an EAL condition as the base case to a BAL condition as the test case. When the nutrient ratio was altered between those conditions, dysregulation was observed in purine and pyrimidine metabolism, as well as in glutamine and glutamate metabolism, and peptidoglycan biosynthesis. Dysregulated metabolites are shown in Figure 1 (Franco et al.).

Similarities are seen in the G20 dataset, where EAL was the base case and EDL was the test scenario. Metabolomic processing was done using a new multiomics platform on XCMS Online that resulted in higher level dysregulated pathways list, compared to the individual metabolite analysis done in DvH. Dysregulation occurs in the purine, pyrimidine, glutamine, and glutamate biosynthesis, though there appear to be no disruption in the peptidoglycan metabolism. There were other pathways in G20 that were altered between these two conditions in addition to the ones seen in DvH. Systems processing other nucleotides like inosine are affected and there is dysregulation in multiple amino acid biosynthetic pathways including asparagine, arginine, valine, and lysine. Changing the nutrient ratio in G20 also disrupts tRNA charging at multiple points. Pathways responsible for carbohydrate metabolism are affected such as trehalose degradation and sucrose degradation. Altering the nutrient ratio causes large changes in the metabolomic profile and to pathways the cell is maintaining in both G20 and DvH.

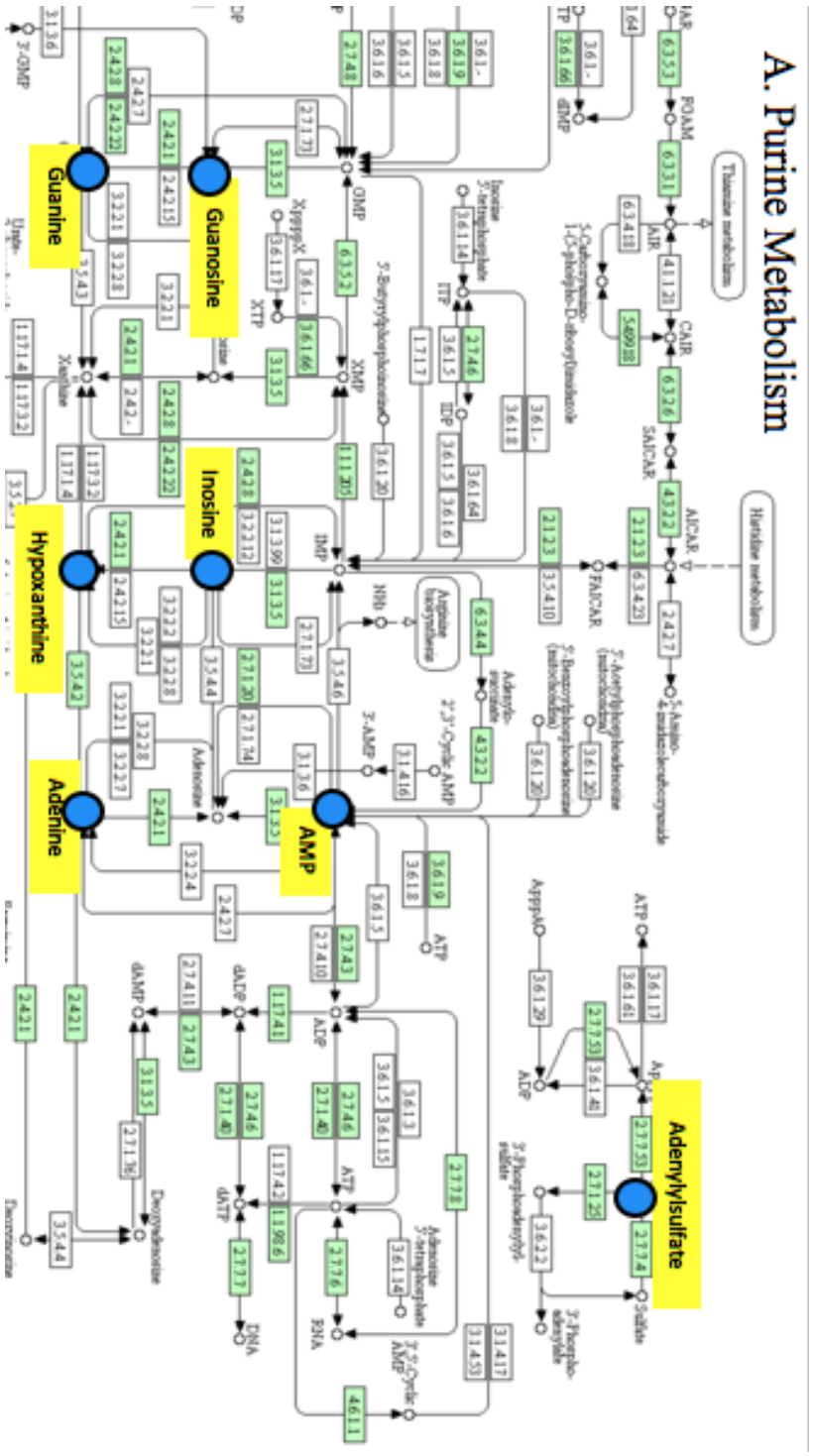
A. Purine Metabolism
Thiamine metabolism
Histidine metabolism
Adenylylsulfate
Guanine
Guanosine
Inosine
Hypoxanthine
Adenine
AMP

## B. Pyrimidine Metabolism

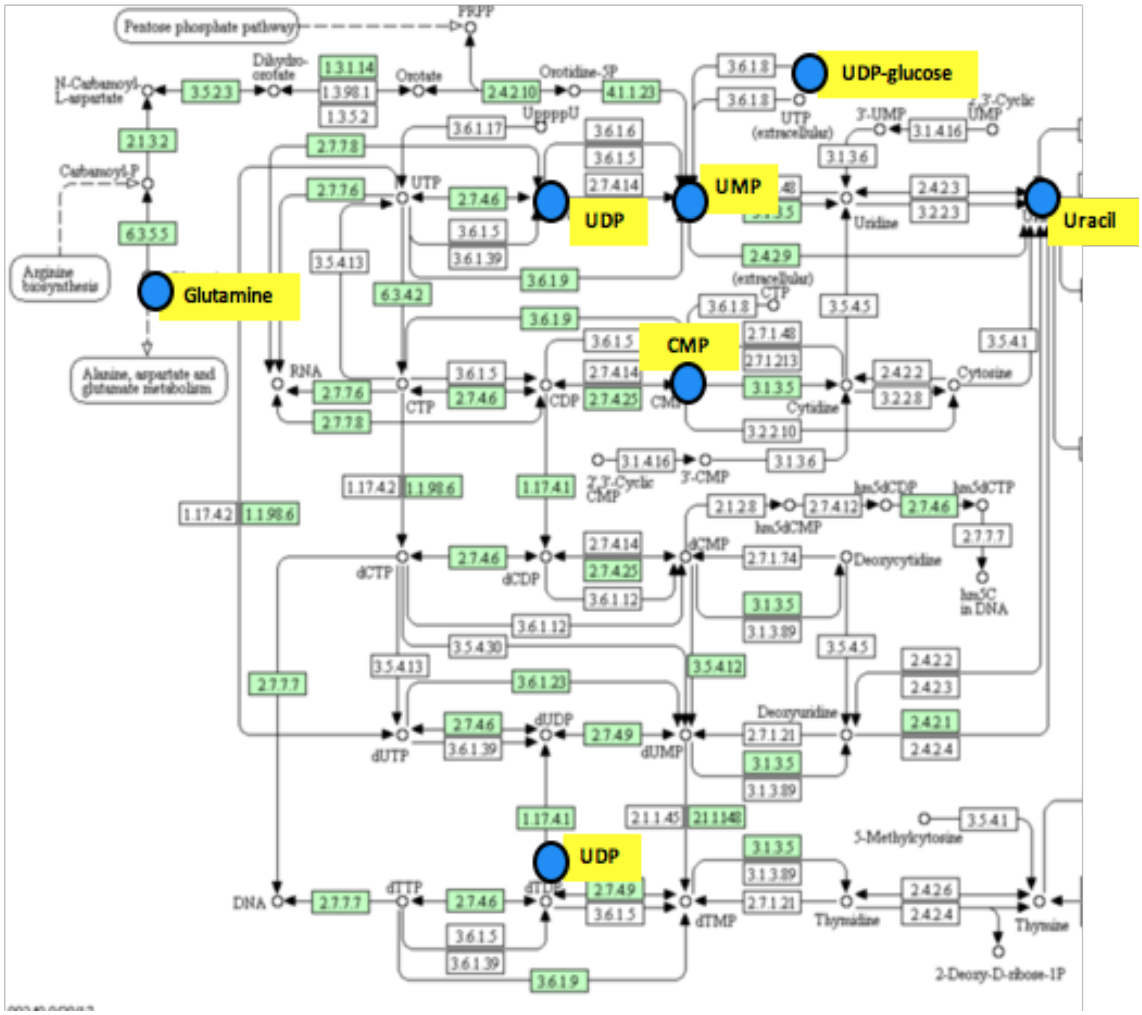


## C. Glutamine and Glutamate Metabolism

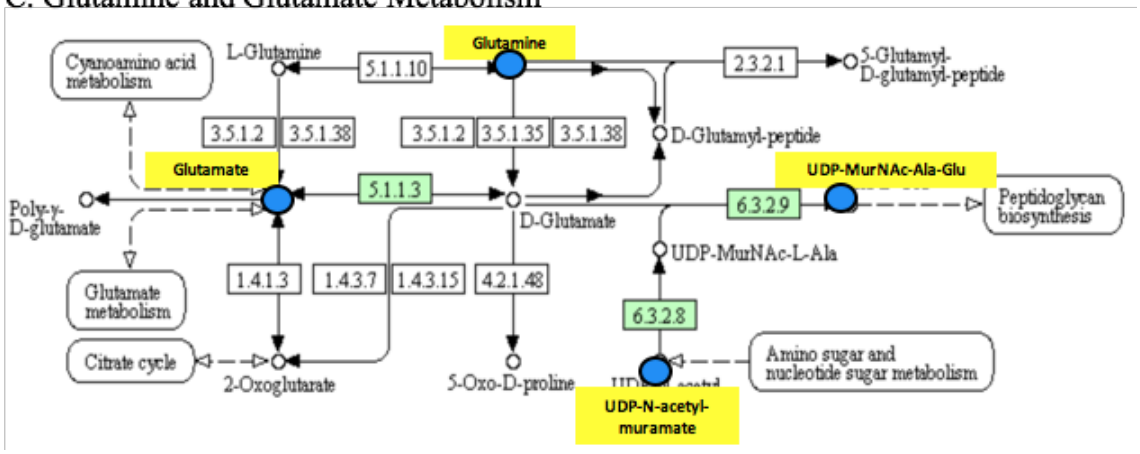

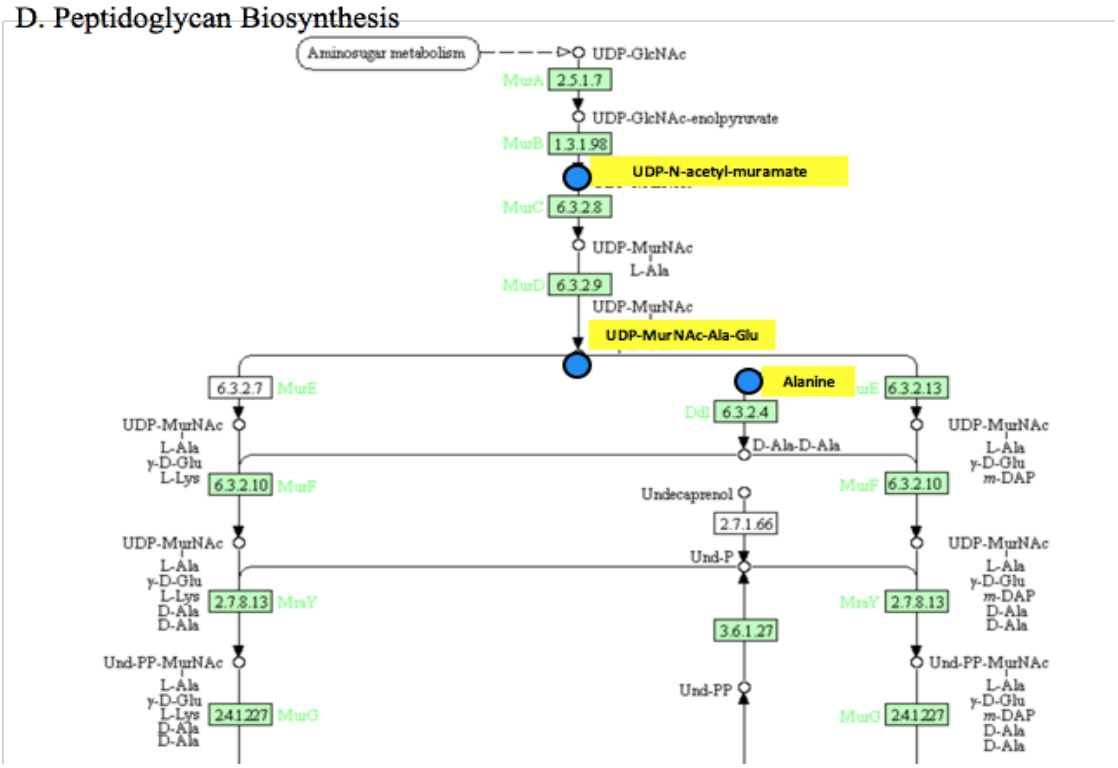


Figure 1. Metabolic pathways with multiple down-regulated metabolites, highlighted in yellow, under EAL conditions. Green boxes represent genes/proteins that are annotated in the D. vulgaris Hildenborough genome. Figures adapted from KEGG. (Franco et al.)

| Pathways |
| --- |
| asparagine biosynthesis I |
| pyridoxal 5'-phosphate biosynthesis I |
| tetrahydrofolate salvage from 5,10-methenyltetrahydrofolate |
| asparagine biosynthesis III (tRNA-dependent) |
| trehalose degradation V |
| phosphopantothenate biosynthesis I |
| asparagine biosynthesis II |
| asparagine degradation I |
| arginine biosynthesis IV (archaebacteria) |
| 6-hydroxymethyl-dihydropterin diphosphate biosynthesis I |
| sucrose degradation II (sucrose synthase) |
| purine deoxyribonucleosides degradation |
| inosine-5'-phosphate biosynthesis I |
| glutamate biosynthesis I |
| glutamine degradation II |
| glutamate biosynthesis V |
| valine biosynthesis |
| valine degradation II |
| 5-aminoimidazole ribonucleotide biosynthesis I |
| tRNA charging |
| lysine biosynthesis VI |
| citrulline-nitric oxide cycle |

Table 3. List of pathways with multiple dysregulated metabolites when comparing EAL conditions as the base case to EDL conditions as the test case.